Aalto-yliopisto
Aalto-universitetet
Aalto University

Master's Programme in Mechanical Engineering

The effects of static strain aging on the mechanical performance of nodular cast iron

Ville Björklund

Master's Thesis
2021

Tekijä Ville Björklund

Työn nimi Staattisen myötövanhenemisen vaikutukset pallografiittivaluraudan mekaanisiin ominaisuuksiin

Maisteriohjelma Konetekniikka (Mechanical Engineering)	**Koodi** ENG25

Työn valvoja Professor Sven Bossuyt

Työn ohjaaja(t) Professor Hannu Hänninen

Päivämäärä 30.7.2021	**Sivumäärä** 90+7	**Kieli** Englanti

Tiivistelmä

KBS-3 loppusijoituskonseptissa käytetty ydinpolttoaine on tarkoitus sijoittaa suuriin kuparikapseleihin, jotka haudataan syvälle peruskallioon. Kapselin pääasiallinen kuromaa kantava elementti on tarkoitus valmistaa EN-GJS-400-15U ferriittisestä pallografiitti-valuraudasta (PGR). Loppusijoitusolosuhteiden takia herää kysymys myötövanhenemisen mahdollisista vaikutuksista sisäosan kestävyyteen, joita ei ole tutkittu nykyisellään riittävästi. Tässä diplomityössä käsitellään staattisen myötövanhenemisen vaikutuksia sisäosassakäytettävän PGR:n mekanisiin ominaisuuksiin ja sisäosan kestävyyteen.

Staattista myötövanhenemista tutkittiin esivenyttämällä materiaalista valmistettuja vetosauvoja 1 %, 2 % ja 3 % nimellisiin venymiin. Esivenytettyjä näytteitä ikäännytettiin eri lämpötiloissa, jotka vaihtelivat huoneenlämpötilasta 400 °C-asteeseen. Staattinen myötövanheneminen (SSA) toi korostuneen myötörajan esiin materiaalin jännitys-venymäkäyrissä kaikilla tutkituilla esivenymillä, kaikissa tutkituissa lämpötiloissa ja kaikilla tutkituilla ikäännytysajoilla, vaikka vastaanotetussa tilassaan tutkittu materiaali myöti tasaisesti ilman korostunutta myötörajaa. Esivenymän suurentaminen nosti materiaalin myötörajaa enemmän verrattuna matalampiin esivenymiin. Maksimaalinen myötölujuus saavutettiin jo yhden päivän ikäännytyksellä 100 °C-asteen lämpötilassa ja tätä pidempi 11 päivän ikäännytys ja/tai ikäännytyslämpötilan nostaminen 200 °C-asteeseen ei vaikuttanut myötölujuuteen merkittävästi. Korkeammissa 300 °C ja 400 °C lämpötiloissa myötölujuus nousi vähemmän ja myötörajasta tuli selvästi vähemmän korostunut kuin matalammissa lämpötiloissa. Esivenyttämättömien testisauvojen ikäännytyksellä ei ollut vaikutusta materiaalin käyttäytymiseen.

Digitaalista kuvakorrelaatiota käytettiin venymien paikallistumisen tutkimiseen vanhennetuilla testisauvoilla. SSA ilmeni testisauvoissa venymien Lüders-nauha-tyyppisenä paikallistumisena myötörajan ympärillä. Tyypillisistä Lüders-nauhoista poiketen useiden deformaationauhojen samanaikainen muodostuminen esti nauhojen liikkeen mittapituuden läpi johtaen ennenaikaisiin jännityskeskittymiin ja lopulta murtumaan

Avainsanat Käytetty ydinpolttoaine; pallografiittivalurauta; staattinen myötövanheneminen

Author Ville Björklund

Title of thesis The effects of static strain aging on the mechanical performance of nodular cast iron

Master programme Mechanical Engineering   **Code** ENG25

Thesis supervisor Sven Bossuyt

Thesis advisor(s) Hannu Hänninnen

Date 30.7.2021   **Number of pages** 90+7   **Language** English

Abstract

Finland and Sweden are amongst the first countries moving forward with the plans regarding geological disposal of spent nuclear fuel. Spent nuclear fuel is intended to be placed in long-term geological repositories in accordance with the KBS-3 method where the spent nuclear fuel is placed in large copper canisters that are sealed and buried deep in the bed rock. The load-bearing element in these canisters is an insert made of nodular cast iron of grade EN-GJS-400-15U. Questions regarding the possible role of strain aging in the material properties of the cast iron insert in the repository conditions have been largely overlooked and have not been thoroughly studied yet. This thesis explores the phenomenon of static strain aging in the nodular cast iron to be used for this application, and its effects on the mechanical performance of the material.

Static strain aging was studied by pre-straining tensile specimens made from the given material to 1 %, 2 % and 3 % nominal strains. The pre-strained specimens were aged at various temperatures ranging from room temperature (RT) to 400 °C for varying times. The static strain aging brought pronounced yield point to the material for all studied pre-strain levels, temperatures, and aging times despite the as received material behaving smoothly with no pronounced yield point. Increasing the pre-strain raised the yield strength of the material more compared to lower pre-strain. The maximum yield strength levels were already achieved with aging in 100 °C for 1 day and aging at higher temperature of 200 °C and/or increasing aging time to 11 days had no significant effect on the yield strength. Aging at higher temperatures of 300 °C and 400 °C resulted in lower increase in yield strength and the yield point became less pronounced as the aging temperature was raised over 200 °C. Aging non-pre-strained specimens had no effect on the yielding behavior compared to as received material.

Digital image correlation was used to study how the static strain aging affect the strain localization in the material. Strain aging was found to manifest as formation of complex Lüders bands at the onset of yielding. Formation of multiple bands inhibited the band propagation and lead to premature localization of strain in these areas, which lead to earlier fracture.

Keywords Spent nuclear fuel; ductile cast iron; static strain aging

Contents

Symbols and abbreviations

Symbols

A	total cross-sectional area of the dislocations per unit area of matrix
A_{gt}	Elongation at maximum force
A_t	Elongation at fracture
c	Concentration
c_0	Defect concentration a long way from dislocation
δ	Thickness of grain boundary
d	grain size
D_0	Maximal diffusion coefficient
D_{app}	Apparent diffusivity trough crystal
D_{gb}	Diffusion coefficient trough grain boundary
D_L	Diffusion coefficient trough lattice
D_p	Diffusion coefficient trough dislocation
E_I	Interaction energy
J	Diffusion flux (chapter 2.2.2)/ J-integral (chapter 2.1.10)
$J(a)$	J-integral value for postulated crack
J_{2mm}	J-integral value corresponding to 2 mm stable crack growth
K_{IC}	Fracture toughness in mode I loading
Q	Activation energy
R	Universal gas constant
S_{FJ}	Safety factor in ASME code used for J-integral analysis
S_{FK}	Safety factor in ASME code (value changes depending on application)
T	Temperature
T_m	Melting temperature

Abbreviations

ASME	The American Society of Mechanical Engineering
BCC	Body-centered cubic
BWR	Boiling water reactor
CERT	Constant extension rate tensile testing
DCI	Ductile cast iron
DHD	Deep hole drilling
DIC	Digital image correlation
DSA	Dynamic strain aging
EBS	Engineered barrier system

EDZ	Excavation damage zone
EDZ_{CI}	Construction induced excavation damage zone
EDZ_{SI}	Stress induced excavation damage zone
EDS	Energy-dispersive X-ray spectroscopy
EPR	European Pressurised Water Reactor
FCC	Face-centered cubic
FE	Finite element
ICHD	Incremental Center-Hole Drilling
KBS-3	Kärnbränslesäkerhet-3
NDT	Non-destructive testing
PWR	Pressurised water reactor
SEM	Scanning electron microscope/microscopy
SKB	Svensk kärnbränslehantering AB
SSA	Static strain aging

1 Introduction

The spent nuclear fuel from nuclear power plants in Finland and Sweden is planned to be disposed using the method called KBS-3 (kärnbränslesäkerhet 3). In this method large copper canisters are used to seal the spent nuclear fuel after which the canisters are buried in crystalline bedrock and surrounded with layer of bentonite clay. The method is based on the general theory that radioactive deposit in the bedrock can be present for tens of thousands of years without harming the health of human populations. The repository is designed to last at least 100 000 years to ensure safe nuclear decay of the spent fuel without causing environmental harm.

The copper canisters are comprised of the outer copper shell with welded copper lid, inner cast iron insert with steel tube cassette inside and steel lid. The copper shell is used mainly for its corrosion resistance and high ductility which ensures the integrity of the shell in the repository conditions. The cast iron insert is the main load bearing structure in the canister, and it should withstand the environmental mechanical loads that it is subjected to. The canister insert can experience yielding due to rock shear movements along fractures in the bedrock that cross the canister hole.

The nuclear decay of the fuel rods causes the temperature to rise inside the insert. The estimated maximum temperature in the middle of the fuel rod bundle inside the cast iron insert is about 230 °C according to worst case calculations and the temperature at the edge of the bundle is around 30 °C lower [1]. In theory this heating of the insert enables the possibility for dynamic and static strain aging in the cast iron insert if the canister insert is subjected to yielding in the repository. The phenomena of strain aging are known for long time, but they are still not thoroughly understood. Strain aging has been studied more in steels than cast irons. The same principles should, apply for cast irons and steels but some differences are still to be expected. For example, the different silicon contents in the materials change the activation energy of the carbon diffusion [2]. This can affect the temperature ranges and strain conditions where the aging can occur. Some studies on the dynamic strain aging effects on the ductile cast iron grade planned to be used in the insert have already been conducted [3]. However, studies regarding of the static strain aging of the specific cast iron grade in the repository conditions have not been conducted and the phenomenon should be studied further. In this study the static strain aging of the cast iron insert over a range of conditions spanning those predicted for the repository is examined.

2 Literature review

2.1 Nuclear waste program and KBS-3

The KBS-3 method is developed by Swedish Nuclear Fuel and Waste Management Company SKB. The Finnish nuclear waste management company Posiva and Swedish SKB intend to use this method for long term nuclear waste disposal in Finland and Sweden. The KBS-3 method consists of three main protective barriers: the copper canister, bentonite clay buffer and crystalline bedrock (figure 1). The copper canisters containing the spent nuclear fuel are buried approximately 500 meters deep to the bedrock and the empty space in the deposition holes is filled with bentonite clay. Finally, the tunnel leading to the deposition hole is backfilled with bentonite clay. [4][5]
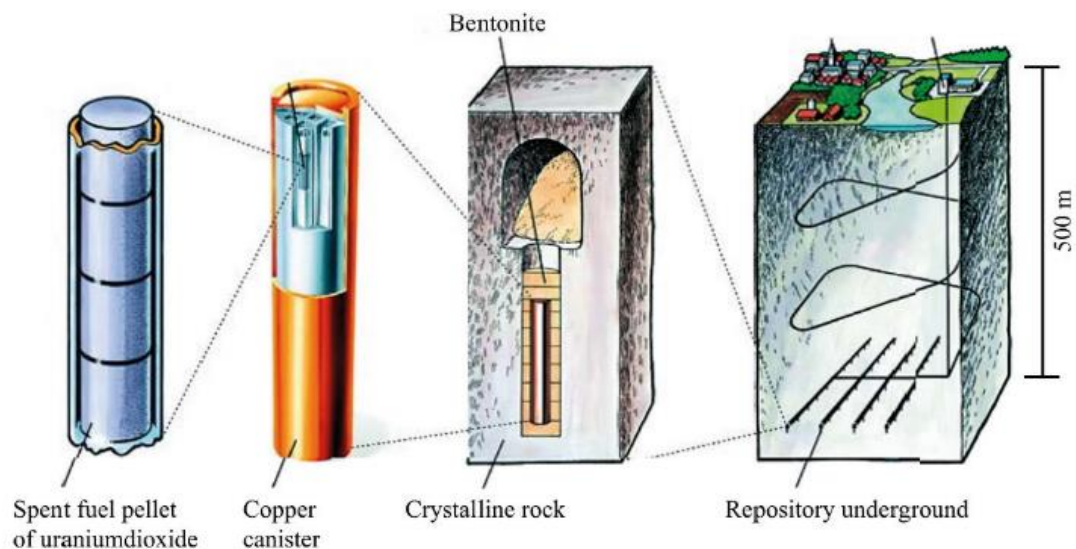

Figure 1 Illustration of the KSB-3 method [5]

Each of the barriers have their own safety functions. The safety functions of the different parts in the engineered barrier system (EBS) in Posiva's repository concept are as follows[6]:

1) The main safety function of the canister is to ensure the prolonged containment of the spent nuclear fuel. This function is mainly dependent on the mechanical strength and load bearing capabilities of the canister as well as the corrosion resistance.
2) The safety functions of the bentonite buffer are:
   a. Provide favorable and predictable conditions regarding the mechanical, geochemical and hydrogeological conditions for the canister and protect the canister from external processes that could compromise its safety functions and the containment of the spent nuclear fuel.
   b. Limit the release of the radionuclides if the canister fails.
3) The safety functions of the deposition tunnel back fill and plug are to:
   a. Contribute to favorable and predictable mechanical, geochemical and hydrogeological conditions for the buffer and the canister.
   b. Limit the release of radionuclides if the canister fails.

c. Contribute to the mechanical stability of the host rock in the vicinity of the deposition tunnels.

4) The safety functions of the backfill of underground openings are to:
    a. Assure that the long-term isolation of the repository from the surface environment and normal habitats for humans and other biota is not compromised.
    b. Limit the inflow to and release of harmful substances from the repository.

2.1.1 Excavation damage zones and fracture growth in bedrock

When considering the possibility of strain aging in the cast iron canister insert it is important to understand the environmental causes for the possible loading scenarios that are imposed on the canister. The different loading scenarios affecting the canister and the possible occasions where actual plastic straining of the cast iron insert can occur are reviewed in section: 2.1.7 "Loads affecting the insert".

When the repositories are designed the deposition, holes are located so that they do not intersect natural fractures of the rock mass. This is essential to avoid the possibility of rock shear movements larger than 50 mm across the canister. However, the rock mass around the deposition hole and the tunnel is affected by the excavation damage that is caused by the construction. In the area affected by the excavation damage the rock strength is significantly reduced and the hydraulic conductivity is increased. This zone is called excavation damage zone (EDZ) which can be further divided into two different zones: construction induced EDZ_{CI} and stress induced EDZ_{SI} zone. The EDZ increases the risk for different types of rock damage mechanisms such as rock shear and spalling which in turn can affect the integrity of the disposal canister.[7]

In-situ experiments in Olkiluoto site have shown that the anisotropic rock masses can experience structurally controlled failure at the lithological borders. In this failure mode the weakest plane fails causing stress relaxation and preventing further progressive failure. In all experiments sub critical fracture growth was observed after boring the test holes. The fracture propagation was observed in two weeks to 18-month period after the boring. The KBS-3V method was found to be prone to initiation of new fractures sometime after the excavation, whereas the KBS-3H method was not. However, after 60 years of disposal, fracture initiation can be expected in both vertical and horizontal repositories. Based on the experiments two-fold failure criterion consisting of 40 MPa for rock mass damage onset and 90 MPa for rock mass strength have been proposed.[7]

The probability for critical rock shear movements in the repository sites during deposition is very low. It is estimated that out of 6000 canisters approximately 4 canisters would be in unsuitable locations where the rock shear amplitude could reach 5 cm. Possibility for even higher rock shears has also been studied. Out of 6000 canisters approximately 0.5 canisters would be subjected to rock shear of 10 cm which would correspond to about 0.12 failed canisters over 1 000 000 year period due to the low probability of earthquakes. The risk for the rock shear is directly proportional to the number of unsuitable canister positions and is thus 8 times higher for the 5 cm criterion [8]. In later studies the probability for 5 cm or larger shear occurring has been even lower and the mean number of canisters expected to be

in critical positions out of 6000 canisters was less than 0.11 in Forsmark site for 5 cm shear criterion [9].

2.1.2 Canister design

The canister is the primary and most important barrier between the environment and the spent nuclear fuel. The canister is expected to effectively limit the release of the radioactive substances to the environment for minimum of 100 000 years. To ensure that this comes true, the canister should remain sealed and intact with very good reliability in the repository conditions.

The canister consists of the outer copper shell and massive cast iron insert. The outer shell of the canister is made of copper because copper has some important properties that make it suitable for the outer layer. The material chosen for the outer shell is Cu-OFP (oxygen free copper alloyed with 30-100 ppm phosphorus). This type of copper has very high ductility and good corrosion resistance, which are critical in order the ensure that the canister remains sealed and intact in the repository. However, the outer shell does not have good load bearing capabilities. The main function of the cast iron insert is to be the load bearing element in the canister design. Additionally, the cast iron insert helps to shield the radiation inside.
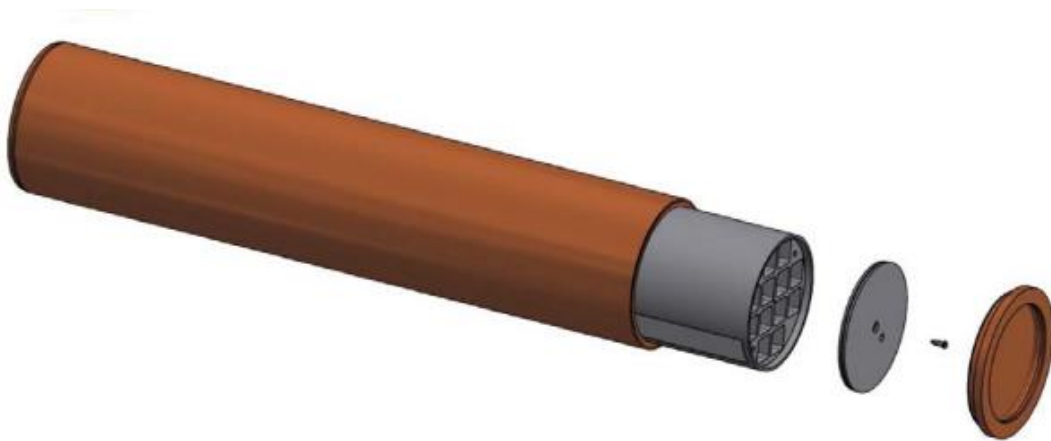
Figure 2. Exploded view of the canister components. The components from left to right are: copper overpack, cast iron insert, steel lid, screw for the lid, copper lid.[10]

There are three different types of canisters for different reactor types since the fuel elements in the reactors have different geometry. The BWR, PWR and VVER-440 canisters are presented in figure 3. The canister dimensions vary depending on the type. The outer diameter of the canister is the same 1.05 m for all canister types, but the total length varies. The lengths of the VVER-440, BWR and PWR canisters are 3.552 m, 4.75 m and 5.223 m respectively.[6]
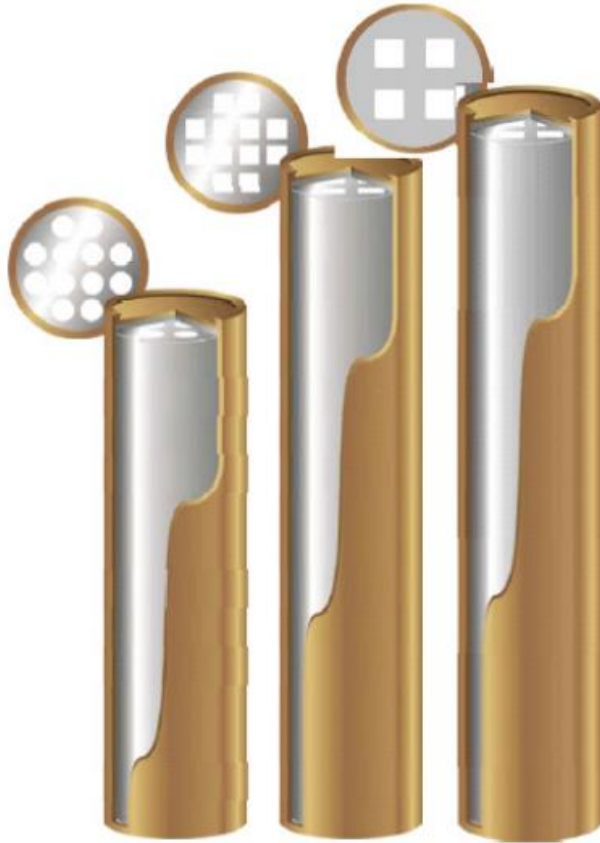
Figure 3 Three different canister types from left to right: VVER-440, BWR and EPR/PWR [6]

2.1.3 Insert manufacturing

The cast iron insert is manufactured by casting. The channels in the cast iron insert are formed when the iron is cast around steel tube cassette in a mold.

The steel tubes are manufactured from cold formed steel plates with welding or are directly hot formed. The hot formed steel tube material should fulfil the requirements in EN 10210-1 S355J2H and the cold formed steel plates should fulfil the requirements in EN 10219-1 S355J2H. The steel tube cassette is manufactured by welding the steel tubes together with support plates. The support plates and flat bars that are used to manufacture the cassette are made of EN 100250 S235JRG2 steel. The steel cassette structure for BWR insert is presented in figure 4.[10][11]


Figure 4 The steel cassette construction for BWR insert.[11]

The insert is manufactured from EN-GJS-400-15U nodular cast iron by casting. Before the casting process, the steel channels are filled with sand to avoid deformation of the steel tubes due to the melt pressure of the cast. The casting method may vary between foundries, but the casting molds used are made of either sand or steel. The molds can be filled from the top of the insert or from the bottom of the insert by leading the molten metal through a channel down to the bottom of the canister. These methods are referred as top pouring and bottom pouring, respectively. During the casting, the temperature of the melt is monitored closely, and the acceptable melt temperature is between 1310 °C and 1370 °C. The filling of the casting mold takes approximately 1 minute. After the casting process the insert is cooled down in the casting mold for few days after which the steel channels are emptied and sand blasted. The excess material from the top of the canister is cut off and the channels of the insert are inspected by moving specific gauge along the length of the channels. The insert is then pre-machined and machined to its final dimensions. [11][12]

2.1.4 Insert microstructure and possible defects

The material properties are tested after the manufacturing by tensile testing. Tensile testing is done for test samples cut from the top of the insert as well as for cast-on samples. The samples cut from top of the insert are usually tested by a third party. The samples cut from the top represent the worst material properties of the insert rather reliably, since all the slag in the cast tends to float upwards. For this reason, the top samples are used to verify the conformity of the insert. The cast-on samples are not representative of the real cast and only work as indication of the result due to the much faster cooling rate in the samples. [12][13]

The samples that showed the lowest and largest elongations in the tensile tests are inspected with optical microscopy to ensure that the microstructure is typical for nodular cast iron. The microstructure should in all positions be minimum of 80% of graphite forms V and VI as specified in standard EN ISO 945 and should not include any graphite of forms I and II. Typical microstructure of the insert is shown in figure 5.[12][13]
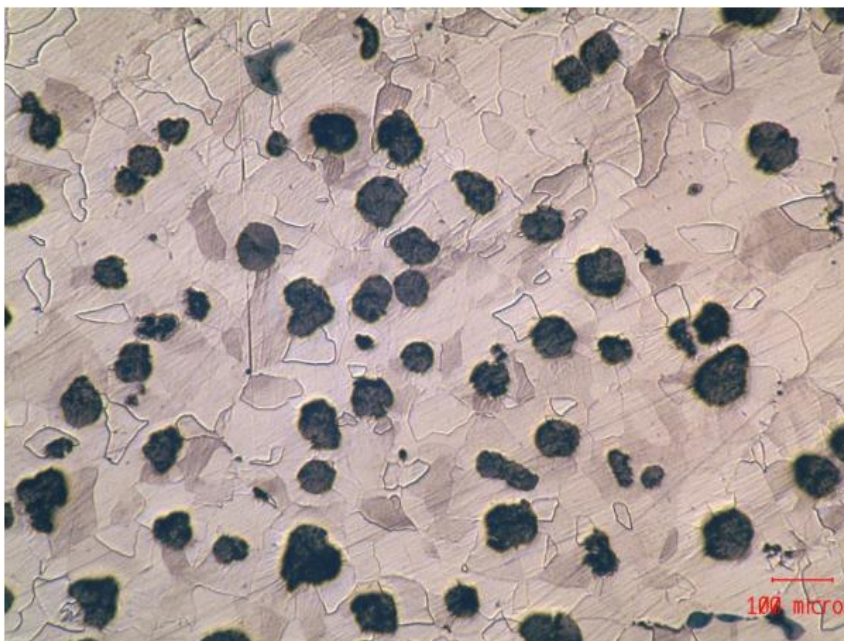
Figure 5 Micrograph from the insert. Ferritic matrix with graphite nodules of form V and IV.[12]

In large casts like the cast iron insert it should be considered that the microstructure in the whole cast is likely not entirely homogeneous. Dahlberg et al. found there to be a systematic variation in the mechanical properties between the different sample positions of the cast iron insert and between separate inserts [14]. While the effect on elastic and initial plastic properties was found to be minimal, the effect on the elongation to fracture was significant. The differences can be explained by the local variations in graphite nodule sizes and the nodule density. Samples containing higher than average concentration of graphite nodules generally tend to fracture at lower strain. Additionally, possible local defects in the cast can have impact on the mechanical properties.

There are several different types of defects that can be present in the cast iron insert. The different defect types and their detection in non-destructive testing (NDT) are explained in the research of Pitkänen [11].

Shrinkage cavities are cavities inside the cast with dendritic walls that is caused by local temperature centrum in the cast. The shrinkage cavity usually occurs in areas where the cast solidifies the last.

Shrinkage pores are small defects that are formed in similar manner to shrinkage cavities, but instead of one big void smaller pores are formed inside the cast. The pores affect the mechanical properties of the material. At the porous area, the ductility and strength of the cast are negatively affected.

Blowholes are essentially voids or bubbles in the cast caused by gas in the liquid of cast. The blowholes can vary in size but are usually between 2-20 mm in diameter. Similarly to pores, blowholes affect the strength of the material negatively

Pinholes are also cavities caused by gas inside the cast but are mainly located at the surface of the cast. The pin holes can be open or closed and are usually 1-100 mm in size.

Shrinkage cavities, shrinkage pores, blowholes and pinholes can all be detected with ultrasonic inspection.

Slag, oxide, and sand inclusions are defects that are caused by impurities that end up in the cast. Slag inclusion is formed usually from magnesium oxide, magnesium sulfide or enriched magnesium slag that is present in the molten metal. In sand inclusion the sand particles are usually from the sand mold. These defects cannot usually be detected with ultrasonic inspection and are instead usually detected in metallographic samples.

Elephant skin is round stretched cavity along the surface of the cast which look like wrinkled elephant skin.

Cracks can form in the insert due to the loads that it is subjected to. In mechanical testing the cracks usually initiate near the steel tubes in the cast.

Low nodularity is specified as a defect type because it can substantially decrease the ductility toughness of the cast. If the cast iron insert has graphite nodules of forms V an IV less than 80 % or has any graphite of forms I and II according to standard EN ISO 945, it is considered to have low nodularity. The low nodularity is possible to detect with ultrasonic testing. However, the ultrasonic detection of low nodularity is challenging because low

nodularity increases the ferrite content in the microstructure and the low nodularity and increasing ferrite content have opposite effects on the sound velocity in the structure.

The acceptable defect size depends on the area the defect is located in the insert. For BWR and PWR inserts different zones used for damage tolerance analysis are determined in SKB design report from 2010 (figure 6). In the report the maximum allowable defect sizes for these zones in isostatic loading are determined for both crack-like defects and hole defects. The maximum defect sizes are listed in tables 1 and 2.[13]
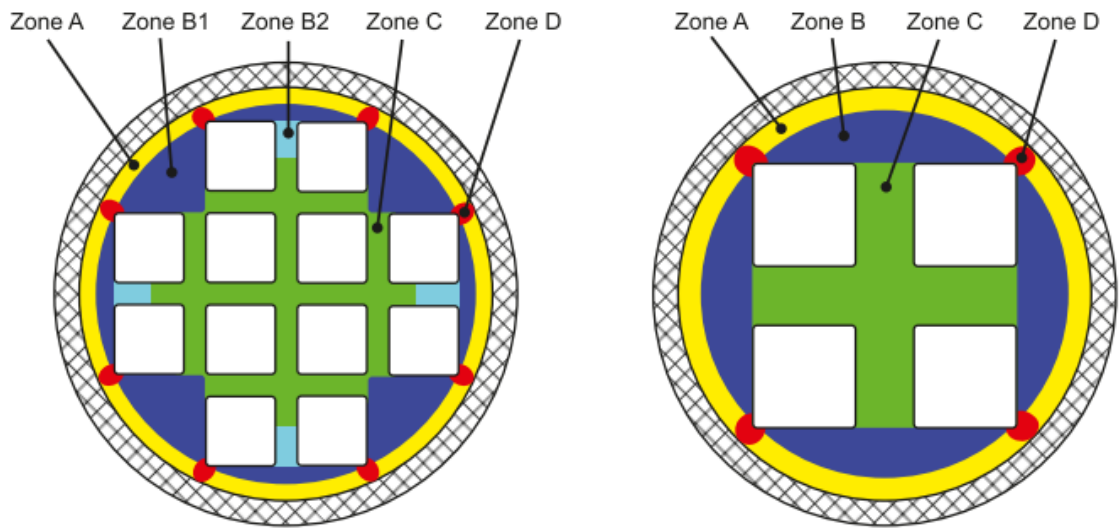

Figure 6 Different zones in BWR and PWR inserts used for damage tolerance analysis and determining maximum defect sizes

Table 1. Maximum acceptable defect size for crack like defects (cracks, slag inclusion etc.) [13].

Zone	Defect size a (mm)	
	BWR	PWR
A	37	53
B /(B1)	65	112
(B2)	50	
C	24	104
D	32	31

Table 2. Maximum acceptable defect size for hole defects (shrinkage cavities, shrinkage pores, blowholes, pinholes etc.) [13].

Zone	Defect size D (mm)	
	BWR	PWR
A	40	80
B /(B1)	60	100
(B2)	20	
C	20	100
D	20	20

2.1.5 Non-destructive testing of the cast iron insert

The NDT testing of the insert is carried out in multiple steps. The first inspections are done by the supplier. Ultrasonic testing and magnetic particle testing are used in the first step. These inspections are mainly done to get the permission to deliver the parts to minimize the risk that the parts are rejected in the later manufacturing steps.[15]

The final inspections are done in the canister factory and are carried out in two steps. The ultrasonic testing is done after the pre-machining step when there is still excess material on the insert surface. This methodology ensures that the whole final volume of the insert will be inspected as the sensitivity of ultrasonic testing near the surface is not good. After machining the insert to its final size specific surface inspection techniques are used. The surface inspection consists of eddy current inspection and magnetic particle inspection.[15]

The ultrasonic testing is the main technique for testing the insert and detecting volumetric defects. Three different ultrasonic techniques are used to inspect different parts of the insert. The ultrasonic methods are normal inspection, angle inspection and transmission inspection. The normal incidence inspection is the primary testing method of the cast iron insert and it covers the volume from the surface to the depth of around 200 mm. The angular wave technique is used as complementary technique to inspect defects the main axis of which is in the radial-circumferential plane. The covered volume is from the surface of the insert to the depth of 50 mm. The transmission inspection method is used to inspect the strips between the channel tubes in the insert. The different volumes inspected with the ultrasonic testing methods are shown in figure 7.[15]
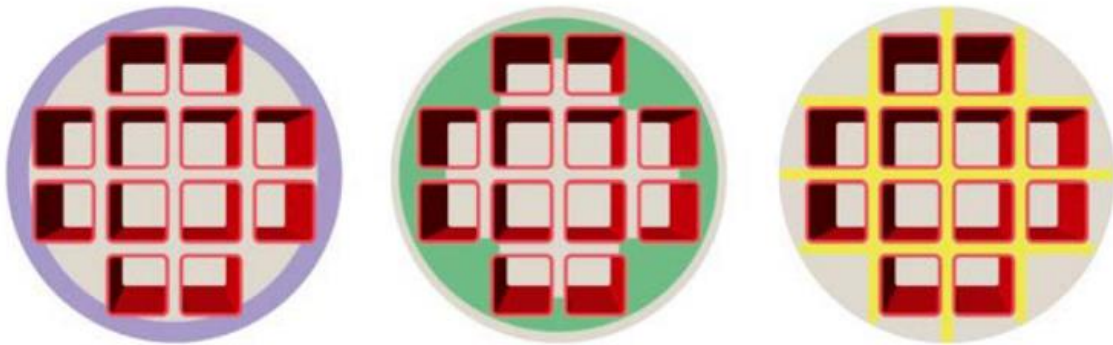

Figure 7 Different inspection techniques for BWR insert depending on the volume that is being inspected. Angle inspection (violet), normal inspection (green) and transmission inspection (yellow).

2.1.6 Residual stresses in the insert

There will be some residual stresses present in the insert after the casting process. The residual stresses form when the cast cools down unevenly. The cast iron insert cools down faster at the surface of the insert and near the channel tubes than in the thicker parts of the cast. When thicker parts of the cast cool down the shrinking of the melt iron causes tension in the thicker sections of the cast, and thus causes compression in the outer cylindrical surface of the insert.

For measuring the residual stresses mainly the Deep Hole Drilling (DHD) technique has been used. The DHD technique is semi-invasive measurement technique that is based on mechanical strain relief. In the DHD technique reference bushes are attached to the front and back surfaces of the component at measurement points. Then a reference hole with diameter 1.5 mm or 3 mm is gun drilled trough the component and the reference bushes. The diameter of the reference hole is then measured along the full thickness of the component using air probe. The measurements are done in increments of 0.2 mm along the length of the hole and 22.5-degree increments along the axis of the hole. After the hole is measured a 5mm or 10 mm diameter core including the reference hole is machined out from the component using electro discharge machining after which the reference hole is measured again through the whole depth using the same increments as before.

Bowman et al. measured the residual stresses in a BWR insert using the DHD technique. For the measurements a 980 mm long piece of the BWR insert, cut from 1310 mm – 2290 mm section from the bottom was used. The diameter of the insert section was roughly 960 mm. The test specimen was provided by POSIVA.

The measurement location can be seen in figure 8. It should be noted that unlike the measurements 1,2 and 3 the measurements 4 and 5 were not drilled radially inwards so the 'hoop' stress in these measurements refers to the combination of radial and hoop stress. The measurement results from the report of Bowman [16] are compiled below:

Measurement 1: The axial residual stress started at 10 MPa at the surface and increased to 58 MPa peak at 2 mm deep. The hoop stress started at 25 MPa and also increased sharply to tensile peak of 57 MPa at 2 mm deep. From here the values fluctuated and decreased to compression achieving compressive peaks of -34 MPa in axial direction and -60 MPa in hoop direction at 37.8 mm deep in the cast iron/ steel tube interface. The axial residual stress in the steel tube part fluctuated between minimum value of 93 MPa and maximum value of 118 MPa. The maximum hoop stress in the steel tube section was 51 MPa and the minimum was 18 MPa.

Measurement 2: The residual stress was found to start at compressive peak of -62 MPa in axial direction and -41 MPa in hoop direction. The stresses then increased to tensile peaks of 4 MPa and 11 MPa in axial and hoop direction, respectively, at the depth of 5.4mm. After the peak at 5.4 mm deep the axial and hoop stresses fluctuated in the error bound with the hoop stress averaging 12 MPa higher than axial stress. At the cast iron/steel tube interface there was axial peak of -5.1 MPa. The hoop stress had tensile peak of 17 MPa at 18.6 mm deep and it reduced to 2.3 MPa in the cast iron/ steel tube interface. In the steel tube section, the axial residual stress fluctuated between minimum of 15 MPa and maximum of 72 MPa. In the steel tube the hoop stress fluctuated between compressive value of -61 MPa and tensile value of 16 MPa.

Measurement 3: The axial residual stress started at compressive peak of about -113 MPa which was the highest measured axial stress in the cast iron. The stress then increased to -14 MPa at 20 mm. The axial stress achieved tensile peak of about 10 MPa at 273.8 mm. The hoop stress started with compressive peak of about -80 MPa which was also the highest hoop stress measured in the cast. The hoop stress increased sharply to about 0 MPa at 21.4 mm

and achieved tensile peak of 25 MPa at 277 mm. After the tensile peaks the axial and hoop stress values fluctuated.

Measurement 4: The residual stress was found to start with compressive peak of -38 MPa and -35 MPa in axial and 'hoop' directions, respectively, and then to increase to tensile peaks of 12 MPa and 6 MPa at the depth of 8.8 mm. The values then lowered again to compression achieving compressive peak values of -39 MPa in axial direction and -34 MPa in 'hoop' direction at the depth of 84.4 mm. In the steel tube section the maximum axial stress was found to be 69 MPa and the minimum value 55 MPa. The hoop stress was compressive in the steel tube section with peak value of -43 MPa and then increased to -11 MPa at the last measurement point.

Measurement 5: The axial residual stress was 66 MPa at the first steel tube/cast iron interface 9.2 mm deep. In the cast iron part, the axial stress was in compression and there was compressive peak of -20 MPa at start at 11.4mm. The axial stress then increased to -2 MPa at 14.2 mm and then fluctuated around zero in the remaining of the cast iron section. The 'hoop' stress was 0 MPa at the steel tube/cast iron interface 9.2 mm deep. In the cast iron part, the 'hoop' stress started at 25 MPa 11.4 mm deep and then decreased to 16 MPa at 36.4 mm deep. The value then rose to the maximum of 34 MPa at 66.4 mm deep. The axial stresses in the first steel tube section fluctuated between minimum tensile value of 51 MPa and maximum value of 81 MPa. The 'hoop' stress fluctuated between minimum value of 0 MPa and maximum of 41 MPa. In the second steel tube section the maximum axial stress was 71 MPa and minimum was 31 MPa. The 'hoop' stress in the second steel tube section fluctuated between minimum of 4 MPa and maximum of 41 MPa.

Overall, the axial and hoop stresses behaved very similarly in the cast iron. All the measurement locations showed compressive peak stresses close to the surface of the insert with the exception of measurement location 1. Generally, after the compressive stress peaks the stresses tended to increase sharply to tension and most of the measurements showed tensile stress peaks before 20 mm deep. The peak compressive residual stresses were found to be -113MPa and -80 MPa in the axial and hoop direction, respectively. These stresses were found at the surface region of the cast iron insert at the measurement location 3. Maximum tensile residual stresses were found 2 mm deep from the surface of measurement location 1. The residual stresses were 58 MPa in the axial direction and 57 MPa in the hoop direction. [16]

Although the stresses in the cast iron are in the focus it is worth noting that in addition to the peaks on the surface of the insert there were high residual stress peaks in the steel tube section. There are clearly stress concentrations at the steel tube sections and some relatively high peaks were also measured at the cast iron/steel tube interfaces. The axial stresses in the steel tubes were higher than hoop or 'hoop' stresses in all measured locations. The maximum axial stress measure in the steel tubes was 118 MPa near the cast iron/steel tube interface and it was measured from location 1. Maximum tensile hoop stress was 64 MPa in the inner surface of the steel tube measured from location 1 and compressive hoop stress of -61 MPa was found in the cast iron/ steel tube interface at measurement location 2. The most notable peaks measured directly at the cast iron/steel tube interface were -60 MPa hoop stress at measurement location 1 and 66 MPa axial tensile stress measured at location 5.[16]
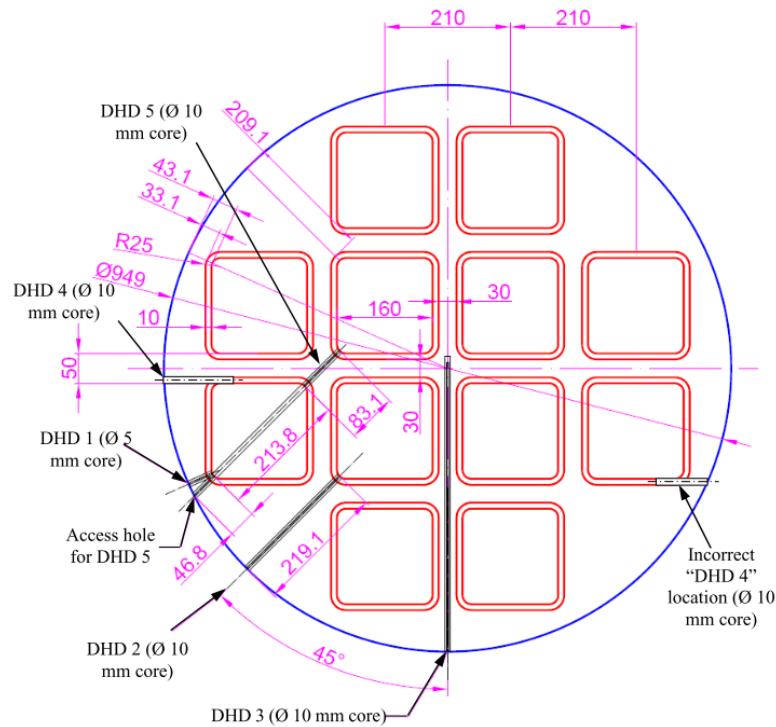
Figure 8 BWR insert cross section showing the measurement locations. Dimensions are in mm.[16]

Shipsha performed assessment on the residual stresses of BWR- and PWR-inserts. The evaluation is based on the previous reports. For the measurements in the reports, DHD and Incremental Center-Hole Drilling (ICHD) methods were used. Based on the evaluation of Shipsha, a pessimistic maximum tensile residual stress of 90 MPa can be assumed in the hoop direction for PWR insert when measured between the steel channels. In BWR insert pessimistic assumption for maximum hoop stress is 60 MPa along the ligament from steel tube corner to the outer surface of the insert.[17]

It should be noted that the overall accuracy of the DHD method is +/-30 MPa which means that many of the characteristic features in the measured residual stresses can be considered to be measurement fluctuations rather than actual changes in the stress field. This accuracy is not valid for the first 1 mm of the surface and the stresses cannot be reliably measured in that region.[16]

The compressive residual stress in the surface of the insert can be beneficial due to the tendency of closing small surface cracks. The compressive stresses can also be beneficial in the case where the canister is subjected to bending as higher applied tensile stresses are needed to cause yielding. The residual stresses are sometimes considered to have no meaningful impact on the higher loading cases of the insert since the residual stresses are thought to disappear as the insert is subjected to yielding.[6][18] However, this is a misunderstanding and not entirely true, since residual stresses are added to the external loads and will determine the location where the yielding starts and the local ductility determines if yielding continues so that the whole insert will yield or if cracking initiates first.

12

The residual stresses can cause local yielding in the insert when combined with the possible compressive loads the insert is subjected to in repository conditions. Additionally, it is probable that some permanent local yielding already occurs during the solidification of the cast due to the uneven cooling and shrinking. In theory the small local yielding could enable the strain aging to occur readily without external yielding scenario like rock shear movements.

2.1.7 Loads affecting the insert

The loads that affect the canister are mainly external loads. There are some possible internal load cases that can affect the canister, but these are so small that they can be ignored when examining the mechanical loads. The nuclear fuel rods produce helium gas when decaying, which can increase the internal pressure inside the canister, but the possible pressure increase is negligible compared to external loads. The other internal load case is related to the corrosion of the cast iron insert which can produce hydrogen gas. This process can only take place if residual water comes with the fuel elements and is enhanced when the canister is leaking and filling with water. A maximum amount of cooling water that will come with the fuel elements is estimated to be 0.6 liter per canister. Additional pressure inside the canister is also caused by the growing corrosion products of iron like magnetite and other iron oxides. Residual water trapped inside the canister during the encapsulation may produce nitric acids in the presence of nitrogen gas which could cause corrosion. However, this effect can be effectively reduced or avoided by the drying process of the fuel assemblies and using argon as the gas inside the canister instead of air. [6][19]

The suitable depth for the repository has been demonstrated to be between 400 - 500 m and the nominal depth of the Olkiluoto repository site is set to be 420m [6][10]. The external loads affecting the canister in these conditions are due to the environment and the bentonite layer surrounding the canister in the repository. The design load of the canister is set to 50 MPa isostatic load consisting of groundwater pressure of 40 MPa and swelling pressure of 10 MPa from the bentonite buffer.

As the bentonite buffer starts to wet the bentonite starts swelling. The wetting process can take up to hundreds of years at dry sites. At the end of the wetting phase when the bentonite is fully saturated with water the bentonite layer will cause isostatic pressure load on the canister since further swelling is prevented due to the confinement. The load from the bentonite can vary in the range of 3-10 MPa and can be unevenly distributed due to uneven wetting and variation in hole dimensions. In the long-term calcium rich ground water can lead to the sodium ions of the bentonite to change with calcium ions which can increase the maximum swelling pressure up to 15 MPa. However, this ion changing process can take thousands of years.[10][6]

The bentonite swelling can cause asymmetrical loading on the canister in different ways. During the water saturation period the water can saturate the bentonite clay unevenly depending on where the water will intrude the deposition hole. The water saturation causes radial swelling pressure on the canister and thus the uneven wetting causes uneven load distribution on the canister. In the uneven loading scenarios, the canister can be thought to act as freely supported beam since the canister is over 5 times longer than its diameter. The worst-case loading scenario during the wetting phase is demonstrated in figure 9. This load

case only occurs during the period the water saturation is incomplete. The load distribution during the water saturation is triangular when the water is assumed to be from axial crack as the wetting and the resulting swelling pressure will vary depending on the distance from the fracture. Most of the deposition holes will fully saturate in the first 2000 years of the deposition. Very pessimistic upper limit for the full saturation is 10 000 years.[10][20]
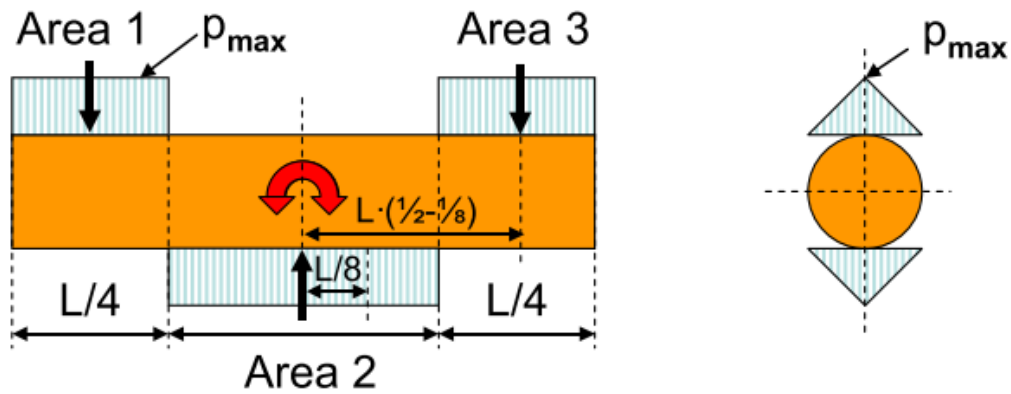

Figure 9 Worst loading case of the canister due to the temporary uneven swelling. The canister is tilted 90 degrees to illustrate the case as freely supported beam. [20]

The deposition hole is not necessarily perfect, and it can be asymmetrical. The worst swelling pressure occurs in case where the deposition hole is banana shaped. After the water saturation there may still remain uneven loading on the canister. During this phase only factors that affect the bentonite buffer density for horizontal cross section of the canister can cause uneven loading. The density difference can be due to imperfections in the bore hole geometry and rock fallout in critical part of the bore hole. In the worst-case scenario both the banana shaped hole and rock fallout cause uneven load on the canister. This load case is illustrated in figure 10.
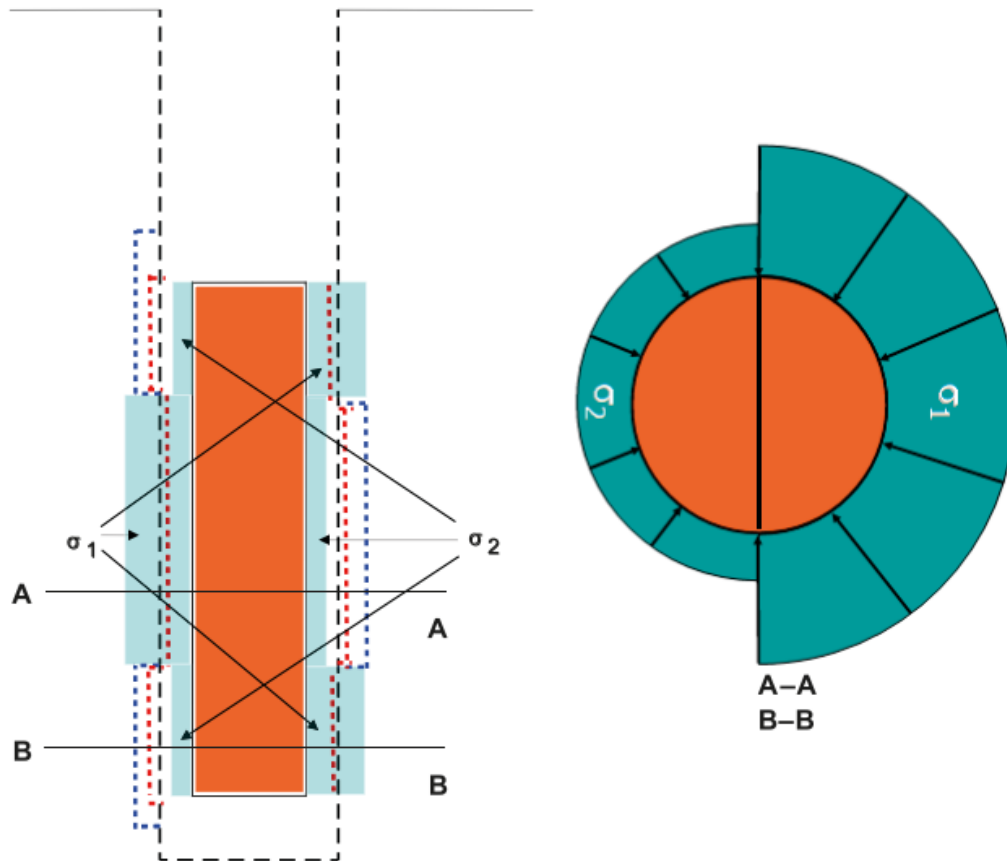
Figure 10 The stress distribution visualized in the combined load case of banana shaped hole and rock fallout in the middle of the canister. The cross-section of B-B can be seen in the right. The cross-section of A-A is mirrored B-B.[10]

During the glacial period the repository site is covered by thick layer of ice. This thick layer of ice can increase the basic ground water pressure of 5 MPa by 35 MPa. This pressure along with the swelling pressure of bentonite will add up to 50 MPa load which is the set design limit for the canister. The first glacial period is thought to begin after approximately 50 000 years. During the glacial period the temperature inside the canister will be lower, but stay between 0 °C and 20 °C. [10]

In rare cases the releasing of stresses in the bedrock can cause shear type rock movement in the bedrock subjecting canister to bending. The shearing can initiate due to earthquakes or due to glacially induced faulting. It has been estimated that the possible earthquakes in the vicinity of the repository should not affect the canister integrity if the repository is placed respect distance away of the deformation zone that could host major earthquakes and the canister holes are not intersected by large fractures. The glacially induced faulting can occur due to deglaciation that causes crustal de-loading or glacial advancement that causes increased crustal loading. The bentonite buffer's function is to soften the impact of the rock shear movement and distribute the loading more evenly. The swelling pressure of the bentonite is directly correlated to the maximum shear loading because the pressure affects the bentonite buffer stiffness.

Due to the long timespan of the deposition the possible rock shear could occur in multiple ways. There could be one large rock displacement or there could be several smaller displacements that cumulate to larger displacement due to repeated earthquakes. The frequency of possible smaller slips is limited to the frequency of earthquakes that could trigger the event. It is argued that during the period of million years only two earthquakes with sufficient magnitude to initiate shearing, could occur in the Forsmark site, thus only two successive rock shear events on one fracture need to be assessed. It is considered unlikely to have even one large earthquake at the site and possibility for two or more large earthquakes happening at the same area is even smaller.[9]

It is estimated that maximum of 5 cm rock shear with velocity of 1 m/s can occur in the repository. The rock shearing could occur in multiple different planes. The maximum strain rate in the insert during the rock shear is estimated to be 0.5 1/s. This is based on Raiko et al. assumption that the maximum strain is 2% and the 5 cm rock shear takes 0.05 s at the velocity of 1 m/s. The maximum average strain rate is 0.02/0.05s = 0.4 1/s.[6]

In some other studies maximum strain rates for the insert were found to be 0.33 1/s and 0.21 1/s. However, these studies also used 0.5 1/s as the pessimistic upper limit for the strain rate.[10]

It is worth noting that the 5 cm rock shear criterion is not an absolute maximum rock shear that could occur at the repository site. The 5 cm is the acceptable upper limit for the rock shear that the canister is expected to handle with good probability without failure and the repository is designed so that exceeding 5 cm shear is very unlikely. In practice the maximum of 5 cm rock shear can be ensured by using respect distances to the possible earthquake sites and by examining the deposition holes and making sure they are not intersected by large fractures [9].

The rock shear scenario has been studied for larger shear displacements as well, but it has been noticed that larger displacements are not safe. Börgesson et al. studied the rock shear for 10 cm and 20 cm rock shear movement in different shear directions and with different bentonite buffer densities as well as for different bentonite types (Ca-bentonite and Na-bentonite) [21]. Particularly in the Ca-bentonite case with higher buffer densities and 20 cm shear displacement, high deformations up to 13% were observed in the simulation results which is very close to the fracture strains of the material and very excessive compared to the required ductility minimum of 3% true plastic strain presented in [10].

A probabilistic approach has been used for analyzing the possible canister failures due to rock shear movements. The probability of canister failure due to rock shear movements was studied by Dillström for rock shear movements of 1-10 cm [22]. It was found that the probability of failure in a canister experiencing 5 cm rock shear was between $5.8 * 10^{-4}$ and $2.2 * 10^{-3}$. The probability of failure quickly raises to unacceptable levels when the rock shear displacement increases over 5 cm. The probability of failure for different size rock shear movements is presented in figure 11.
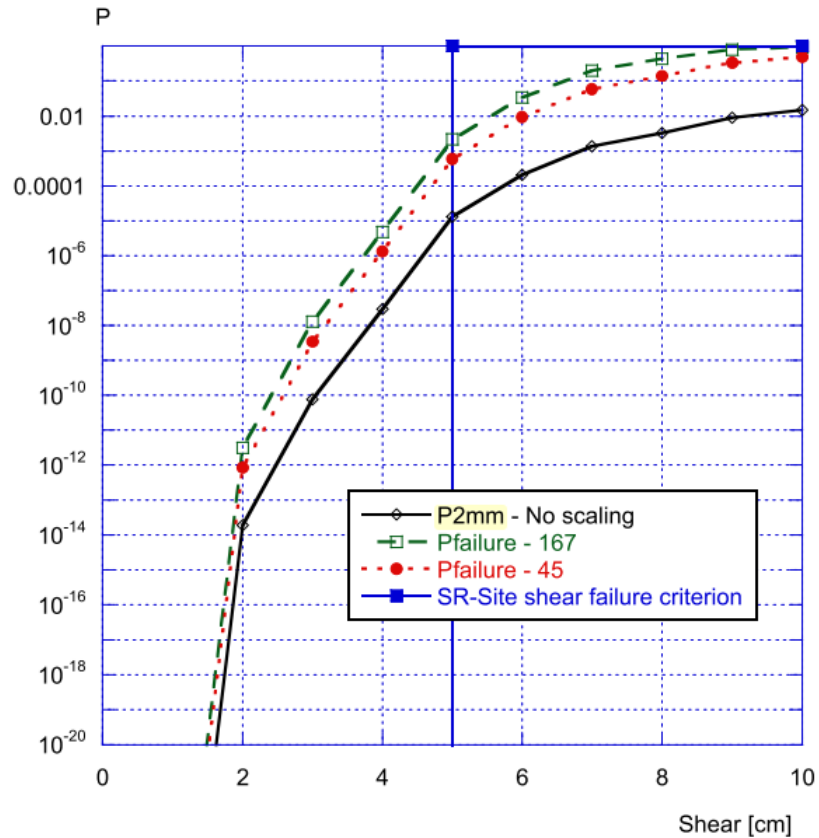
Figure 11. Probability of failure for different defect amounts in the insert and probability for 2 mm stable crack growth against the 5 cm failure criterion [22]**.**

2.1.8 Mechanical testing of the insert

The tensile, compressive and fracture properties of the ductile cast iron was studied by Minnebo et al. [23] Three different inserts were used for studying the mechanical properties. Significant variation between the inserts I24, I25 and I26 was observed in 0.2 % proof stress and flow stress even though same specifications for the ductile cast iron were used. However, the proof stress and flow stress remained at acceptable levels for all the specimens except for the ones manufactured from the top of the I24 insert. This may be due to the top pouring method used for casting the I24 insert. The elongation to failure had significant scatter between samples. The large variation was explained by the presence of casting defects. The variation in elongation to fracture can be seen in figure 12. It is worth noting that two opposing size effects were observed in the tensile tests. Higher specimen volume increases the probability of critical defect being present in the sample but on the other hand the defects will have higher impact on smaller volume specimens, thus the two effects seem to cancel each other. In compressive testing no significant differences in 0.2% proof stress were observed compared to the tensile tests. However, no low ductility behavior was observed in the compressive tests. Additionally, more significant strain hardening was observed in the compressive tests than in tensile tests.
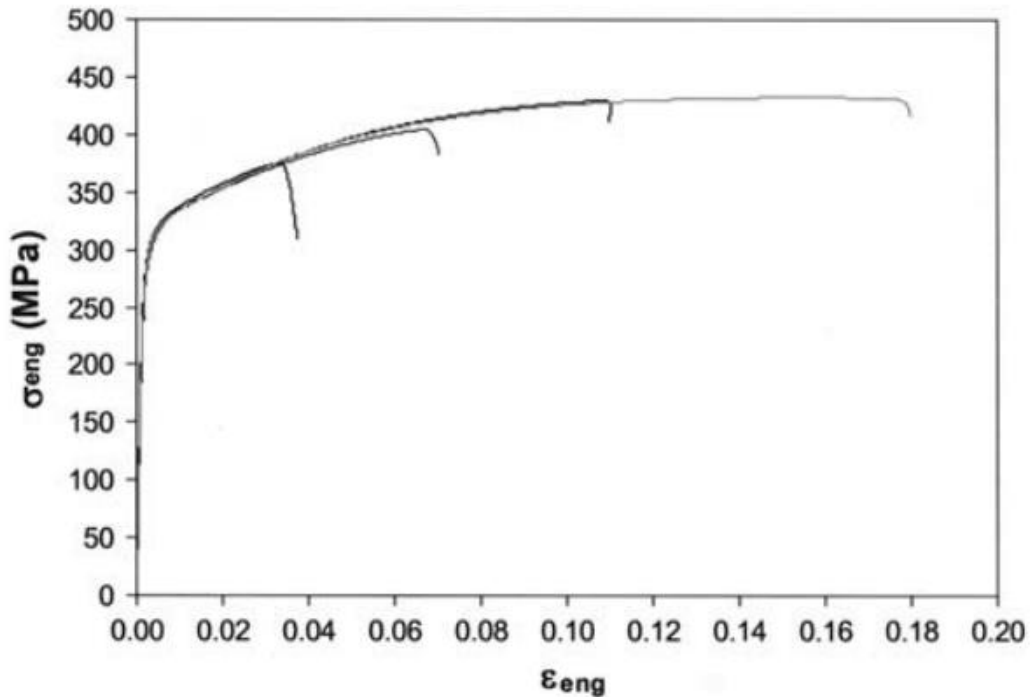
Figure 12 Engineering stress-srain curve showing the scatter in elongation to fracture from I26 insert tests. The stress-strain behavior is identical between samples until failure occurs at different strains.

Nilsson et al. carried out mechanical pressure tests for BWR insert [24]. The motivation behind the tests was to evaluate whether a glacial isostatic pressure load of 44 MPa could result in mechanical failure of the canister by either global plastic collapse or fracture from regions that could experience tensile stresses. As the tensile tests of the insert material have shown rather large variance in results due to different casting defects and inhomogeneous microstructure it remained unclear whether this kind of mechanical failure could happen. The large size of the canister insert makes it more prone to these kind of defects since the probability of critical defects being in the cast goes up us the cast volume increases.

For the pressure tests two mockup canisters each with total length of 1050 mm were used. The total weight of the canister was 5 tons. The mockups consisted of 700 mm long piece of the insert with diameter of 948 mm and 948 mm long copper tube with inner diameter of 952 mm and wall thickness of 50 mm. Additionally two 48 mm steel lids and two copper lids were used for the mockups. The first mockup was cut from the insert section that showed the largest indication of defects from the ultrasonic testing. The first mockup was manufactured from insert I26. In addition to the casting defect the first mockup had relatively large offset of the steel tube cassette of 12 mm which reduced the wall thickness in some parts of the insert. The second mockup was manufactured from insert I24. Unlike the first mockup the second one did not show any indication of casting defects or did not have steel tube channel offset. However, a smaller corner radius of 10-15 mm instead of 20-25 mm was observed in the steel cassette which results in higher stress concentrations in corners.

Four load cycles were performed for the first mockup canister. External pressure loads of 40 MPa, 70 MPa, 100 MPa and 130 MPa were used. With each load cycle the pressure was first

18

steadily increased to the final value and then held for 120 seconds after which the canister was unloaded rapidly. Radial plastic deformation of 5 mm was observed after the 100 MPa loading. After the 130 MPa pressure cycle the first mockup showed substantial plastic radial deformation of 20 mm. During the 130 MPa holding the cold isostatic press pumped more fluid into the press, indicating that the canister continued to deform during the holding time. The first mock-up canister remained intact after the four loading scenarios. The highest deformation occurred at the site of lowest wall thickness. A partial debonding and buckling of the steel tubes was observed as result of the plastic deformation. The fact that plastic deformation occurred already at 100 MPa pressure which is lower than the predicted pressure in FE modelling is probably due to the 12 mm channel offset in the first mockup canister as well as due to the higher yield and tensile stress used in the FE model.

For the second mockup the same four loading cycles were applied. Additionally, a fifth loading cycle was applied with the intent to load the canister until failure. The observed results up to the 130 MPa pressure were similar than in the tests of the first mock-up canister. Some additional deformation compared to the first mockup was seen during the loading between 40 and 70 MPa and the deformation was more symmetrical than in the first mockup. The more symmetrical deformation is probably due to the symmetrical placement of the steel tube cassette unlike in the first mock-up. At 139 MPa a loud bang was heard in the test after which the pressure immediately dropped. The test was interrupted immediately after this. The results show that the canister experienced a global plastic collapse with large deformation in the insert and the steel channels. The maximum indentation observed was almost 200 mm and the insert showed large and very asymmetric deformation after the collapse. Partial debonding of the steel tubes is also seen in the second mock-up.

The crack growth under isostatic pressure load was also studied by Nilsson et al. as part of the pressure tests [24]. Dye penetrant testing was used to identify possible cracks in the surface regions. The dye penetrant testing revealed some surface cracks in the indented parts of the insert surface. Radiographic inspection showed multiple cracks in the steel tube cast iron interface with maximum length of about 40 mm. To get further information about the crack depth and propagation mode the part was cut into smaller pieces and examined with ultrasonic testing. The crack depth was estimated to be about 10 mm which was confirmed with metallographic examinations. The crack depth of 10mm is close to the depth of the region of tensile stresses. Further examination with scanning electron microscope (SEM) revealed details of the crack tip morphology and the crack propagation method. Stretching of the material ahead of the crack tip was shown, which led to separation of graphite nodules from the ferritic matrix, forming voids around the graphite nodules. The crack then propagated through the voids by coalescence of the voids at the crack tip.

As summary it was found that in isostatic pressure testing the cracking of the insert mainly initiates near the steel channels in areas where the insert is subjected to tension and plastic deformation. The cracks are mostly initiated at larger subsurface inclusions near these areas and the cracks grew by stable tearing. The further crack growth is suppressed due to the crack growth resistance of the material and/or the fact that only small area near the channel is in tension, thus the crack arrests when trying to propagate into the compressive region. [24]

In later journal paper of Nilsson et al. the same pressure tests were reported and additionally the effects of the test near the steel channel corners were examined. Based on FE-analysis the cracking in the insert at the cassette corner area was expected to be very unlikely. However, inspection of the insert in the corner regions showed that several cracks were formed during the isostatic loading. Two macro-cracks parallel to the channel corner were observed. The area where the cacks initiated showed significantly smaller graphite nodule size than the rest of the wall thickness. The cracks propagated to the area with consistently larger and more deformed graphite nodules and the crack propagation mechanism showed formation of microcracks at the matrix grain facets in front of the crack tip, which then coalesced together. However, the cracks quickly arrested in the compression after growth of a couple of millimeters. The morphology of the cracks was different than in the tensile regions and resembled intergranular brittle fracture. The authors attributed the crack growth to be driven by the shear stress in the corner region.[25]

2.1.9 Finite element analyses of the insert

FE analysis for Isostatic loading

Many different finite element analyses have been conducted for the isostatic loading case. Ikonen performed a mechanical analysis for VVER 440, BWR and EPR canisters. Finite element model with steel tubes described as separate element to the insert with 5 mm eccentric offset of the steel tube cassette was used for the analysis. The copper layer was not included in the analysis since reliable data for long-term creep of copper under isostatic load was not available that time. This means that in practice the copper layer should provide extra margin against failure. The BWR insert was found to collapse at external pressure of 90.2 MPa which means that the safety margin is around 2.1 if the design load is 44 MPa.[26]

The plastic collapse was studied with finite element modelling by Nilson et al. prior to the mechanical pressure tests of the mock-up canisters. For the FE-analysis a slightly different geometry was used for the mockup canisters that was based on earlier mockup design. In the model the canister length was 1400 mm instead of 1050 mm that was used in the final pressure tests. The longer canister results in slightly higher strains and stresses according to the preliminary parameter studies. 1500 mm experienced 14% strain and 519 MPa effective stress and 1000 mm insert experienced 11% strain and 479 MPa effective stress. In the FE-analysis the copper canister was found to yield at external pressure of 10 MPa and the insert was found to yield at external pressure of 110 MPa. According to the simulations some local yielding already occurs at the corners of the insert for external pressure of 44 MPa. However, a global plastic collapse only occurred at external pressure of 130 MPa. During the plastic deformation only parts of the steel tubes and the cast iron close to the steel tubes experiences tensile stresses. These are the critical areas for crack growth assuming that the cracks could only propagate in tension. The results of the actual mechanical testing of this paper are reviewed in chapter "Mechanical testing of the insert". [24]

Martin et al. studied the plastic collapse of the canister under isostatic load. 3D and 2D finite element models built based on shorter mockup canister were used for analysis. 2D plane strain model resulted in lower collapse pressures than the 3D model. 2D plane strain model was used as the reference model for the studies. The authors note that the results of the 3D models approach the 2D model results as the canister length increases. The plane strain

model was found to experience plastic collapse at 112 MPa external pressure when the steel tube cassette was offset by 12 mm. In the collapse scenario the steel tube cassette was modeled as separate element not bonded to the cast iron insert with frictionless contact assumed between the cassette and insert. The copper shell was also included in this model with frictionless contact assumed between the copper shell and the insert. The steel tube cassette was debonded due to the tendency of some of the steel tubes to debond in the mechanical tests that have been conducted. As the debonding will reduce the overall canister stiffness this modeled case represents the worst case scenario. [27]

In later studies of Hernelind the plastic collapse was studied with detailed finite element model. All details are included in the model for the steel tubes and insert for BWR and PWR canisters. The steel channel tubes were connected by welded support plates. In the model the support plates, base plate and the base screws were glued to the cast iron insert. The steel lid was fixed to the center via screw. The screws were simplified as cylindrical shapes and some small holes in the original drawing were left out of the model. Nominal dimensions with the steel tube cassette in the center was used as reference model for both BWR and PWR inserts. Additionally, case with the steel tube cassette moved 10 mm off-center according to manufacturing tolerances was modeled. The BWR insert was found to collapse at around 97 MPa of external pressure and the manufacturing tolerances did not have any meaningful effect on the collapse pressure. When cylindrical defect was included in the model and yield surface was reduced the collapse pressure decreased to around 85 MPa. The same results for PWR insert were 116 MPa and 104 MPa, respectively.[28]

FE analysis for uneven loading scenario

Börgesson et al. investigated the uneven swelling scenarios of the canister. The maximum bending stress in the insert for the wetting phase was calculated to be 105 MPa. For asymmetrical loading after the full saturation of the bentonite buffer the maximum bending stress in the insert was calculated to be 111.5 MPa. Saturation densities of $2021 \, kg/m^3$ and $1959 \, kg/m^3$ were used for this load case. These densities corresponded to swelling pressures of $\sigma_1 = 7823 \, kPa$ and $\sigma_2 = 3272 \, kPa$ (figure 9). For the wetting phase bentonite buffer density of $2021 \, kg/m^3$ was used.[20]

The asymmetric loading case caused by the banana shaped hole and rock fallout have been simulated by Börgesson and Hernelind [29]. For the finite element analysis saturation densities $2020 \, kg/m^3$ and $1970 \, kg/m^3$ were used. These are close to the values derived earlier by Börgesson [20].The maximum axial tensile stress was found to be about 78 MPa while the maximum principle stress was about 79 MPa. These values are much lower than the analytically derived result of 111.5 MPa axial load. The stresses are well below the yield stress of the cast iron and any yielding should not occur during this asymmetrical loading. [29]

FE analysis for rock shear case

Various finite element analyses for the rock shear case have been performed thus far. Different models that have varying geometries, mesh designs, buffer properties, shear planes etc. have been used. Damage tolerance analyses for varying bentonite buffer densities have

been conducted where 0 °C temperature was assumed for the cast iron insert. For the bentonite buffer 1950, 2000, 2022, and 2050 kg/m^3 densities were evaluated.[10]

Hernelind studied the rock shear case and its effect on the bentonite buffer and the canister. The effect of the shear movement on the canister insert was evaluated through finite element modelling using somewhat simplified geometry. The shear case was studied for 5 cm and 10 cm rock shear movements. The highest value for the plastic strain in the insert was found to be 1% and the highest stress occurring in the insert was 340 MPa in 5 cm rock shear case. For 10 cm shear case the corresponding numbers were 1.9 % and 357 MPa, respectively. These are, however, the cases where the rock shear is affecting the canister simultaneously with the glacial pressure of 30 MPa. If the glacial pressure is not affecting the canister during the rock shear, the maximum values for the strain and stress are 0.5% and 321 MPa for 5 cm rock shear and 1.6 % and 351 MPa for 10 cm rock shear. The largest strain is located at the insert edge close to the corner of the steel tube cassette. The strain distribution can be seen in figure 13. [30]

Based on these results Raiko et al. noted that the maximum effective stress of 340 MPa in the case of 5 cm rock shear corresponds to 2.55 % plastic strain on the static uniaxial stress-strain curve for cast iron. Even though the highest amount of plastic strain occurs in the case where the glacial load is present, it is not the most detrimental loading scenario for the cast iron insert as the compressive glacial load decreases the maximum axial tensile stress in the insert. The maximum axial tensile stress is detrimental for the possible crack growth in the insert, and thus the damage tolerance analyses are calculated without the glacial load. [18]
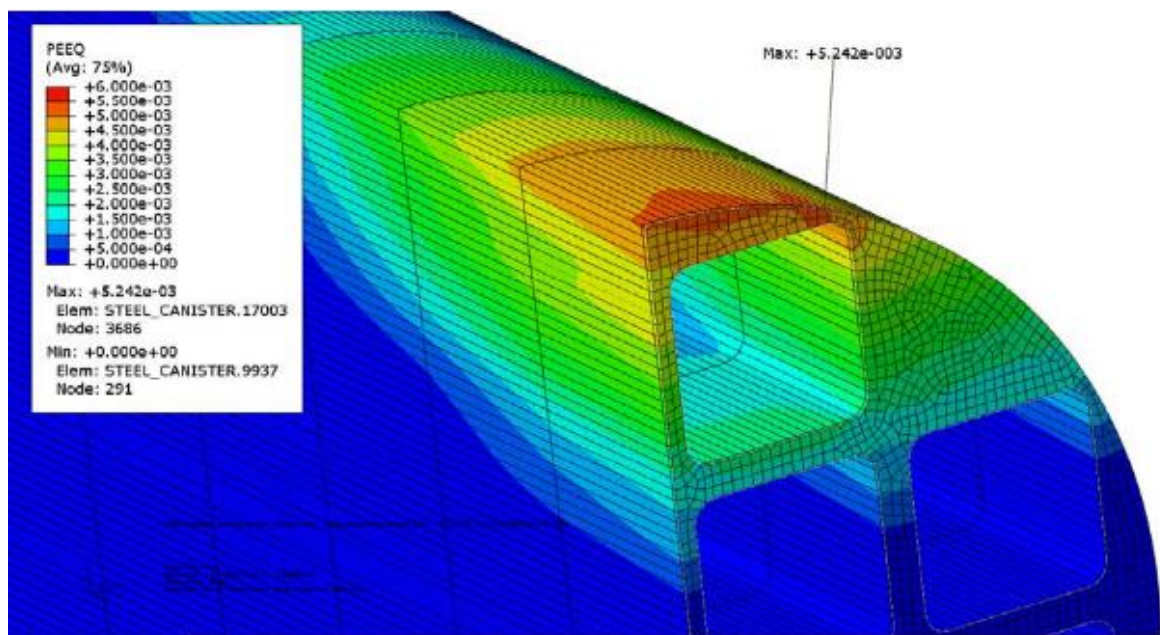
Figure 13 Plastic strain distribution in the insert for the 5 cm rock shear case with 2050 kg/m3 bentonite clay buffer.[30]

Later Hernelind conducted further rock shear analyses for PWR- and BWR-inserts using models that included a much more detailed geometry. The model consisted of the cast iron insert, the steel lid and the copper canister surrounded by the bentonite buffer. Only half of the canister is modeled due to symmetry and the mesh is generated using mostly 8-noded

hexahedral shapes and some 6-noded wedge elements. The model size is defined by approximately 126 000 elements and 160 000 nodes. For the model that takes manufacturing tolerances in to account the maximum plastic strain of 2.7 % and maximum Mises stress of 401 MPa were observed for the BWR insert in the 5 cm rock shear case at 3/4 canister height. The maximum axial stress in this case was 395 MPa. For the model that did not account for the effect of manufacturing tolerances the maximum plastic strain was found to be 1.5 % and maximum Mises stress was found to be 392 MPa in the same 5 cm rock shear scenario. The maximum axial stress was 395 MPa also for this model. For the PWR insert considering the manufacturing tolerances also somewhat increased the strain in the insert. However, for PWR insert the strains and stresses are smaller. For the model that takes manufacturing tolerances in to account the maximum strain was 1.4 % in the 5 cm rock shear case, while it was 0.74 % in the case where the tolerances were not accounted for. The maximum Mises stresses were 349 and 329 MPa, respectively. The maximum axial stresses were very similar between the models like in the BWR insert and they were 330 and 333 MPa.[31]

Dillström studied the effect of the rock shear case on the cast iron insert and compared the effect of different meshes between Hernelinds original and updated models [30][31]. Dillström concludes that similar stresses were found in the original and updated models in the most important regions. The updated models have higher localised stresses due to the mesh design, but they are not entirely accurate, since the mesh grids are not designed to be used in damage tolerance analysis. Many of the stress consentrations can be explained by the use of wedge elements and some of the stress concentrations can be disregarded as the neighbouring elements have substantially lower stresses. The maximum stress in the axial direction for the original global model presented in Hernelind's paper was found to be 333.2 MPa. The maximum axial stress is located at the outer surface of the canister insert. The stress distribution can be seen in figure 12.[32]

Similar maximum strains have been found in the later studies and reasonable ductility limit of 3% true plastic strain for the cast iron insert when safety factor is taken into account is presented by Jonsson et al.[10].
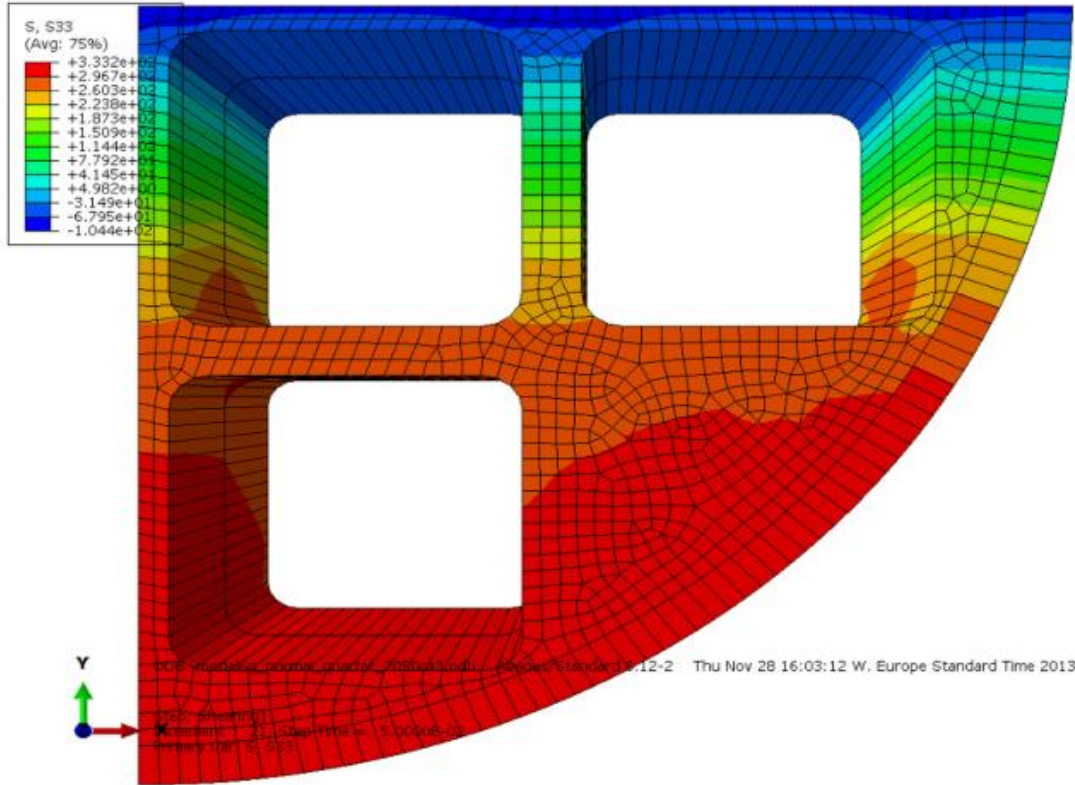
Figure 14. Axial stresses in BWR-insert for 5 cm rock shear load at 3/4 of the canister height for bentonite buffer density of 2050 kg/m³. [32]

2.1.10 Mechanical failure process and failure criteria of the insert

There are three different types of failure processes that may occur for the cast iron insert. The insert may experience plastic collapse, crack initiation, or exceed the acceptable plastic strain.

The design target of the insert against isostatic pressure load is 50 MPa. The criteria for the design load should not exceed 2/3 of the maximum load of the insert. The mock-up cast iron inserts of small size have been studied and loaded to failure. In the studies the inserts collapse between 130 and 140 MPa. This is more than double the design target of the insert.[10] The pressure tests by Nilsson et al. [24] are reviewed more in detail in chapter "Mechanical testing of the insert".

In the case of load-controlled load case like the isostatic loading K_{Ic} data, based on crack initiation is used for the damage tolerance analysis. A crack initiation in the insert is not allowed for load-controlled loading scenarios. The safety factor of $S_{FK} = 3.16$ is used which is the requirement for normal operational load from ASME Code.

For the crack initiation in the case of displacement-controlled load the damage tolerance analysis is based on J-integral analysis. A crack initiation can be allowed in the case of displacement-controlled load. The stable crack growth criterion for the cast iron insert is:

$$J(a) = \frac{J_{2mm}}{2} \tag{1}$$

24

Where $J(a)$ is the J-integral value for postulated crack, J_{2mm} is the J-integral value that correspond to 2 mm stable crack growth in fracture toughness tests and 2 is the safety factor that corresponds to safety margin of $S_{FK} = 1.41$ for emergency load event in ASME code. The discrepancy in the safety factor comes from the relationships between J and K_I which follows $J \sim K_I^2$. Due to this the safety factor used in J-integral analysis should be of form $S_{FJ} = (S_{FK})^2$. The rock shear case is classified as low probability case due to the fact that only 4 canisters out of 6000 are expected to be subjected to shearing of 5 cm (chapter: " Excavation damage zone and crack growth in bedrock"). [10][6]

The rock shear case is the only situation where the DCI insert could be subjected to significant plastic deformation. The worst case for the rock shear case is estimated to occur when the shear plane is at 75% of canister height perpendicular to the axis of the canister. The canister is required to withstand 5 cm rock shear with a velocity of 1 m/s [6]. In the case of this type of rock shear the BWR and PWR inserts are subjected to 0.5% plastic strain. In the case of 10 cm rock shear the strain is 1.7%. When taking the safety factor in to account the acceptable requirement for the ductility of the insert is 3% true plastic strain at distance of 100 mm or more from the middle of the cast iron insert cross-section. For distances smaller than 100 mm from the center point of the cross-section there are no ductility requirements. [10]

2.1.11 Temperature inside the canister

The fuel rods are stored in pools at the nuclear power plants before the encapsulation and disposal process. Appropriate decay heat is usually achieved in between 30 to 50 years after which the fuel elements are ready for disposal [6]. The decay heat power of the fuel decreases rapidly as time passes. It is estimated that the decay heat power halves in the first 50 years [33].

At the actual deposition the maximum surface temperature of the canister is reached about 20 years after the start of deposition. The temperature stays near the maximum value for another 40 years until it starts to slowly decrease after 60 years of deposition. After 600 years the outer surface temperature of the canister will be below 50 °C [6]. The elevated temperature and heat generation is estimated to be relevant only during the first 1000 years of the deposition [6].

Ikonen modeled and studied the temperature inside the disposal canister in his work. The maximum allowable temperature of external surface of the canister is limited to 100 °C. The initial heat powers of the canisters were set to 1700 W, 1830 W and 1370 W for the BWR, EPR and VVER 440 fuel elements, respectively. In the study it is estimated that in this reference case the maximum temperature in the middle of fuel rod bundle for BWR, EPR and VVER 440 fuel are 213 °C, 229°C and 233°C, respectively. The maximum temperature in the cast iron insert in this reference case was 193 °C for BWR insert and 190 °C for EPR insert. Ikonen also modeled the worst-case scenario for the temperatures. In the worst case the maximum temperature of the outer surface of the canister was set to 120 °C which is more than the design specification and the heat powers of the fuel elements were set to 1.2 times of the values in reference case. Additionally, more pessimistic values for the copper

emissivity, conductivity of steel, conductivity of cast iron and fuel rod surface emissivity were used. In the aforementioned case, the temperature inside the fuel rods rose to 286 °C in BWR canister and to 304 °C inside the EPR canister. These temperatures correspond to maximum cast iron insert temperatures of 264°C and 261°C, respectively. The temperatures in both the reference and worst-case models are rather pessimistic since the modelling was based on the assumption that the gap between the copper shell and the cast iron insert is in vacuum and the only heat transfer mechanisms are thermal radiation and conduction between the metal parts. The reference case temperatures were also modeled in a case where the gap between the copper shell and the insert is filled with argon, thus allowing convection and better heat transfer. In this case the maximum temperature reached inside the fuel rod was 145 °C in BWR canister and 170 °C in EPR canister. These fuel rod temperatures correspond to cast iron insert temperatures of 115°C and 114°C in BWR and EPR canisters, respectively. [1]

Raiko repeated some of the thermal analyses using different assumptions that more accurately represent the evolution of the canister temperature. Maximum temperature of 95 °C for the outer surface of the canister and 1700 W decay power for all the fuel elements was assumed. Additionally, 36 $W/m^2/K$ thermal conductivity was used for the cast iron insert. For the gap between the insert and copper shell width of 1.5 mm was used with emissivity of 0.22 and 0.6 for copper and cast iron surfaces respectively. The insert is filled with argon whose thermal conductivity is 0.018 $W/m^2/K$. The conductivity used for air was 0.030 $W/m^2/K$. The maximum temperatures of the fuel rods were 193°C and 166°C, when the gap between the copper shell and the cast iron insert was vacuum or filled with air. The corresponding insert temperatures were 139°C and 103 °C. [6]

In a later report maximum fuel temperature for the fuel elements was found to be 147.1-203.0 °C, when the pessimistic temperature of 100 °C was used for the copper tube and decay power of the fuel elements was 1700 W. These temperatures corresponded to 112.7-118.1 °C temperature for the cast iron insert. In conclusion, the temperature of the insert should not raise above 125 °C assuming that the bentonite buffer and rock have sufficient thermal conductivity and the bentonite buffer stays below the designed temperature limit of 100 °C. [10]

2.2 Plasticity of crystalline materials

2.2.1 Dislocations

Crystalline materials contain structural line defects that run through the crystals. These line defects are called dislocations. Dislocations enable the deformation of the material while maintaining its basic crystal structure. The movement and multiplication of dislocations under external stress usually manifests as plastic deformation of material. There is clear correlation between plastic deformation and dislocation density and the dislocation density increases as the plastic deformation increases. The dislocation density of material is usually expressed as total length of the dislocation line per unit volume. A well annealed metal usually contains about 10^{10} to 10^{12} m of dislocation line per cubic meter, whereas heavily cold rolled metals typically contain somewhere between 10^{14} and 10^{15} m of dislocation line per cubic meter.

A dislocation is defined with the help of a Burgers circuit. A Burgers circuit is essentially a path between atoms in the lattice that forms a closed loop. When the circuit around dislocation is repeated in dislocation free crystal the circuit will not form closed loop. The vector that is required to close the circuit in perfect crystal is called Burgers vector. There are two general types of dislocations, edge dislocations and screw dislocations. When the dislocation line is normal to the slip direction the dislocation is called an edge dislocation and when the dislocation line is parallel to the slip direction the dislocation is called a screw dislocation. In other words, in edge dislocations the Burgers vector is normal to the dislocation line and in screw dislocations the Burgers vector is parallel to the dislocation line.

There are two basic types of dislocation movement, glide and climb. Glide occurs when the dislocation moves in a plane that contains its line and Burgers vector, and climb occurs when the dislocation moves out of the glide surface. Dislocation that is able to glide is called glissile, and dislocation that is not able to glide is called sessile. Slip is the most common manifestation of deformation in crystalline material and it occurs when multiple dislocations glide. The slip occurs in specific planes in the crystal lattice and the slip plane is usually the plane with highest density of atoms. The slip direction corresponds to the shortest lattice translation vector. For example, in body centered cubic (BCC) material like ferrite the slip usually occurs in the closed-packed plane of {110} and the slip direction is [111]. However, the slip is more complex in BCC crystals than for example in FCC crystal, since the slip has also been observed in {112} and {123} planes [34].

Due to the different possible slip planes in the same [111] slip direction the slip might occur in different {110} planes or combination of {110} and {112} planes, depending on the applied stress, which is why the observed slip lines often appear as wavy and ill-defined. The active slip plane depends on multiple factors such as crystal orientation, composition, temperature and strain rate. For example, iron alloyed with silicon or iron deformed in low temperature seems to be restricted to specific {110} slip plane.[35]

2.2.2 Diffusion

It is critical to understand diffusion when dealing with physical metallurgy especially at elevated temperatures. Diffusion is based on phenomena where atoms move from higher concentration regions towards lower concentration regions. Even though the individual atomic movements are random, the atoms continue to redistribute until the material composition is uniform. This is because there are more atoms to move down to concentration gradient than there is to move up. This is known as Fick's first law of diffusion:

$$J = -D\frac{dc}{dx} \qquad (2)$$

Where J is the diffusional flux, D is the diffusion coefficient and c is concertation, thus $\frac{dc}{dx}$ is the concertation gradient. The diffusional flux represents the number of atoms diffusing in unit time across unit area.

The Fick's first law of diffusion only applies in steady state conditions where the concentration at each point is invariant, and the concentration gradient does not change with time. However, in many applications the concentration gradient tends to change as a function of time. This is the basis of Fick's second law which can be expressed in one dimension as:

$$\frac{dc}{dt} = D_x \left(\frac{d^2 c}{dx^2} \right) \qquad (3)$$

The diffusion coefficient is also dependent on temperature and the diffusion coefficient D can be changed dramatically by changing the temperature. The temperature dependence of the diffusion coefficient can be described in its simplest form by equation:

$$D = D_0 \exp\left(-\frac{Q}{RT}\right) \qquad (4)$$

where D_0 is temperature independent constant, Q is the activation energy, T is the absolute temperature and R is the universal gas constant. For example, in ferrite the diffusion of iron atoms increases by factor of 10^6 as the temperature increases from 500 °C to 900 °C and in austenite by factor of 10^2 as the temperature increases from 910 °C to 1100 °C. [36]

The diffusion and movement of atoms trough crystal lattice occur in different ways depending on the type of atom diffusing. Interstitial atoms are atoms small enough that they fit between the spaces of the host atoms present in the lattice. For example, in ferrite, nitrogen, hydrogen and carbon can be present as interstitial atoms between the iron atoms. The interstitial atoms need to squeeze between the host atoms when diffusing which is why the thermal energy needed for the activation is higher for larger atoms. The activation energy for interstitial diffusion of carbon and nitrogen in ferrite is approximately 80 kJ/mol.[36]

The self-diffusion of metal and the diffusion of substitutional atoms occurs through vacancies in the crystal lattice. Vacancies are empty spaces in the lattice or in other word sites that are missing an atom. The probability of atom jumping to the next site depends on the probability of the site being vacant and the probability that the atom has sufficient activation energy for the jump. The activation energy for the substitutional diffusion has been found to be lower than that for the self-diffusion in pure metals and it has been suggested that the vacancies associate with solute atoms. The binding of the vacancies to the substitutional atoms increases the effective vacancy concentration in the vicinity of the solute atoms and thus increase the jump rate of solute atoms. However, the vacancy migration is slowed since the vacancy tends to stay in the vicinity of the solute atom as it diffuses through the lattice. [36]

Grain boundaries and dislocations also act as additional paths for diffusion of large atoms. The grain boundaries act as channels that are approximately two atoms wide. The solute atoms can diffuse trough these channels at faster rate with coefficient D_{gb} than trough lattice

with coefficient D_L. If the grain size is d and the grain boundary thickness is δ the total diffusion flux can be described as sum of both contributions:

$$J = -\left(D_L + D_{gb}\frac{\delta}{d}\right)\frac{dc}{dx} \tag{5}$$

Where the effective diffusion coefficient is:

$$D_{eff} = \left(D_L + D_{gb}\frac{\delta}{d}\right) \tag{6}$$

Similarly, the cores of dislocations can act as pipes through which the solute atoms can diffuse faster with coefficient D_p. The contribution of the dislocations to the total flux depends on the relative cross-sectional area of dislocations and matrix. The apparent diffusivity trough crystal can be described by equation:

$$D_{app} = D_L + D_p A \tag{7}$$

Where A is the total cross-sectional area of the dislocations per unit area of matrix. [36]

2.2.3 Dislocation locking

Different point defects like vacancies and substitutional interstitials interact with dislocations in the material. The point defect in the crystal causes surrounding stress field that interacts with the dislocation and increases or decreases the elastic strain energy of the crystal. The change in the strain energy is called the interaction energy E_I.[37]

The energy of point defects in crystalline structure changes in the vicinity of dislocations by E_I. The equilibrium defect concentration c changes from the concentration value c_0 far from the dislocation. The defect concentration c at a point (x,y) is:

$$c(x,y) = c_0 \exp\left[-E_I(x,y)/kT\right] \tag{8}$$

The point defects tend to congregate in regions where the interaction energy E_I is large and negative which leads to areas with higher concentration of solute atoms forming in the material. These dense atmospheres of solute atoms are called Cottrell atmospheres. At the occupied site where E_I is large, negative extra work will be required to separate the dislocation from the solutes. This means that extra stress is required to make the crystal slip, thus making the materials stronger. To form these atmospheres, the temperature needs to be sufficient for solute migration to occur in the material. However, if the temperature is too high, the atmospheres can "evaporate" into the solvent matrix due to entropy contribution to the free energy. Dense atmospheres of $c \geq 0.5$ can be expected even in material with dilute equilibrium defect concentration of $c_0 = 0.001$ at temperatures of $T = 0.5\,T_m$ where T_m is the melting temperature, in regions where $-E_I \geq 3kT_m$. This mechanism of dislocation

locking is behind the phenomenon called strain aging, which is discussed more in detail in the next section.[37]

2.3 Strain aging

Strain aging is an embrittlement and hardening mechanism of cast irons and carbon steels that happens in specific conditions that are a combination of plastic strain and temperature. The strain aging can either occur during the plastic deformation or after the plastic deformation. If the aging occurs during the plastic deformation it is called dynamic strain aging (DSA). Strain aging that occurs after the plastic deformation is called static strain aging (SSA). Cottrell and Bilby proposed in 1949 that strain aging is the result of diffusion of carbon or nitrogen atoms that collect around dislocations formed during the plastic deformation [38]. The carbon and nitrogen atoms around the dislocations increase the stress needed to move the dislocation, effectively immobilizing the dislocation. Today this mechanism is generally accepted to be behind the strain aging. Strain aging increases the hardness of the material while simultaneously reducing the ductility. Strain aging usually manifests as an increase of tensile strength of the material, negative strain rate sensitivity in DSA, and reduction in total elongation to fracture.

Static strain aging occurs when the material is strained beyond its yield point and then unloaded. The diffusion of carbon and nitrogen atoms leads to migration to the strain fields of dislocations since this results in an overall reduction in strain energy. This causes the solute atoms to gather around the dislocations forming interstitial concentrations or atmospheres called Cottrell atmospheres. Due to the solute atom concentrations, extra stress is required to move the dislocations and the dislocations are locked in place. This is usually seen as sharpening of the yield point and increase in yield strength. If high enough stress is applied to the dislocation, it can be separated from solute atoms allowing it to move again and be unaffected by the solutes. However, if the material is subjected to sufficient heat after this and left to age for sufficient amount of time, the solute atoms diffuse back to the dislocation re-introducing the locking effect.[39][37]

The breakaway of dislocation from the Cottrell atmospheres is somewhat controversial as the cause of the sharp yield point in strain-aged material. An alternative theory has been proposed suggesting that once the atmospheres have formed they stay locked and the yielding phenomenon is caused by newly formed dislocation and their movement. There is probably not one correct theory and the precise mechanism behind the yield point phenomenon depends on the effectiveness of the dislocation pinning. If the dislocation pinning is weak the yielding can probably occur due to unpinning of the dislocations but if the dislocations are effectively locked by interstitial atmospheres or precipitates the yield point phenomenon is probably the result of new rapidly formed dislocations.[39]

The amount of carbon and nitrogen needed for severe strain aging to occur is very small at around 0.002 wt% for carbon and 0.001-0.002 wt% for nitrogen. However, dislocation pinning and strain aging can occur at even lower solute concentrations. As low as 10^{-6} wt% of carbon is sufficient to introduce one interstitial atom per atomic plane along the dislocation lines present for dislocation density of $10^{-12}\ m^{-2}$, which is typical for annealed iron. The static strain aging can readily occur at temperature range of only 20-150 °C due to the diffusion of carbon and nitrogen being very rapid in iron compared to other solutes. [39]

Codd et al. studied the dislocation locking in ferritic iron and found that nitrogen locking is substantially stronger than carbon locking. The locking was found to affect the ductile-brittle transition temperature so that stronger locking results in a higher transition temperature. Elastic and chemical interactions between the solutes and dislocations are suggested as the reason for the differing locking effects. The elastic interaction is caused by residual chemical bonding between the dislocation and the impurity atom. [40]

Dynamic strain aging occurs when the material is subjected to yielding at elevated temperature. The elevated temperature increases the carbon and nitrogen diffusion rate and enables the locking to occur during the deformation. When the test specimens are deformed at a constant deformation rate, sharp changes in stress can be observed in the stress-strain curve. These abrupt movements are usually referred as serrations, serrated plastic flow or jerky flow. The term jerky flow refers to lower temperature flow that manifests as small irregularities in the stress-strain curve, while the term serration refers to larger and more regular stress changes in the stress-strain curve that occur at higher temperatures [41]. The serrated yielding is also called the Portevin-Le Chatelier effect. The serrations are caused by the fast dislocation locking. The diffusion of the interstitial or substitutional locking elements is fast enough that the dislocations lock and release multiple times during the constant deformation rate. During the serrated yielding the deformation is inhomogeneous in space as well as time. [37]

Mouri et al. have studied dynamic strain aging in nodular cast iron. The fatigue and tensile behavior of ductile cast iron varies depending on the temperature range. The fatigue behaviors can be divided to three different temperature ranges. In the temperature range of 20 - 127°C the dislocation velocities are faster than the diffusion of carbon atoms. In the range of 127 - 300°C the dislocation and diffusion speed of the carbon atoms are compatible. Above 300°C the carbon diffusion is faster than the rate of the dislocation movement. The dynamic strain aging occurs in the temperature range of 127 - 300°C and already at low stress levels [3][42]. However, for static strain aging of ductile cast iron specific temperature range is not available from literature.

Static strain aging has been widely used in automotive industry to strengthen the steel frames of the cars. Usually in automotive industry this process is called bake hardening, which is a high temperature static strain aging process usually applied in the temperature range of around 150-200°C. The higher strength of these bake hardening steels allows the car frames to be constructed using thinner gauges while maintaining the strength. This results in weight saving, thus contributing to fuel economy. The basic concept of bake hardening, and static strain aging is illustrated in figure 15.
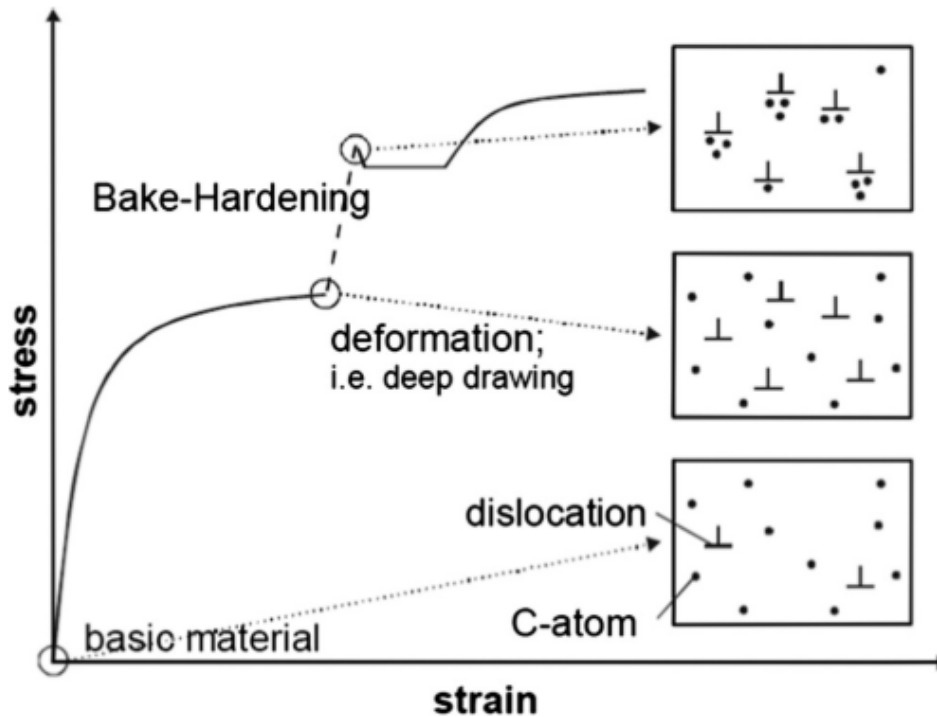
Figure 15 Schematic explaining the concept of bake hardening by stress-strain curve. The solute carbon atoms diffuse to the regions of dislocations formed during the plastic deformation inducing Cottrell locking. [43]

Although effects of static strain aging (SSA) has been quite extensively studied on steels [44][45] it has not been studied on cast irons. Same principles should apply between the cast irons and steels. However, the different silicon content in the materials changes the activation energy of carbon diffusion [2]. This can affect the conditions such as temperature ranges and pre-strains where SSA can occur. The rest of this chapter deals only with static strain aging.

2.3.1 The role of temperature in strain aging

Increasing aging temperature tends to increase the strain aging effect. Because increasing temperature accelerates the diffusion of solutes in the material the strain aging occurs more rapidly in higher temperatures. However, at higher temperatures it is possible to induce over-aging in the material. When overaged, the material becomes softer and the ductility of the material increases rather than decreases. Gündüz studied static strain aging behavior of dual phase steel and found that over-aging occurred at 150°C, 200°C and 250 °C aging temperatures [46]. Ramazani et al. studied bake hardening effect in FP600 and TRIP700 steels and found no over-aging to occur in the TRIP700 steel when aged in 220 °C, while DP600 steel showed evidence of the over-aging phenomenon at 170 °C temperature [43]. There is not much literature about this over-aging phenomenon in cast irons, but due to the higher silicon content it is reasonable to assume that this happens at higher temperatures than with steels. Lui and Chao studied high temperature properties of spheroidal graphite cast iron and found that it is prone to intermediate temperature embrittlement [47]. The ductility minimum of the cast iron was found to be around 400 °C and the embrittlement temperature was between 300-400 °C for creep rupture, fatigue- and tensile tests. The same temperature

range for carbon steels is between 150-250 °C [47]. These results indicate that the over-aging phenomena may occur at 300-400°C range in ductile cast irons.

De et al. studied static strain aging behavior of ultra-low carbon bake hardening steels [48]. According to the study there seems to be an incubation period at the start of the strain aging where the yield point elongation does not occur. In the paper the incubation period observed was 30 minutes for all pre-strain levels used. However, the incubation period depended on the aging temperature and the period became shorter as the aging temperature was increased. In the study it was found that the yield point elongation (YPE) increased after the incubation period until approximately 1000 minutes of aging. After this point the YPE saturated and remained constant or dropped slightly with further aging. With 1% pre-strain small additional increase in yield stress was observed after the first aging stage with temperatures higher than 140 °C. According to the authors this might be due to a low temperature carbide formation or solute atom clustering. Similar results on the strain aging have been observed in other studies according to the review paper of Baker et al. [49].

2.3.2 The effects of aging time

It is important to note that strain aging is not a linear process as a function of time. Usually as time passes there are several distinct hardening stages where the yield strength increases at different rates. The number of distinct stages and the nature of the hardening stages can vary depending on the material and aging methodology used. However, there are usually some similarities that can be observed between different studies. The first aging stage is almost always attributed to the formation and saturation of Cottrell atmospheres and the following stages are usually results of further carbon clustering or low temperature carbide formation.

In bake hardening steels at least four different stages for the strain aging behavior have been observed in the study of Vasilyev et al. [50]. In the study very sensitive internal friction measurements and dynamic Young's modulus measurements were carried out in order to track the complicated strain aging process in the studied steel. The changes in the Young's modulus are very small due to strain aging but allow the quantitative measurement of strain aging process over time without destructive testing. The first stage where the Young's modulus increases rapidly was observed in all temperatures. In the second stage the Young's modulus increased much slower than in the first stage and decreased slightly at the end of the second stage. This effect is probably due to the atmospheres at the dislocations saturating, thus stopping the further pinning of dislocations. While this happens some desegregation of carbon atoms from the grain boundaries takes place explaining the decrease in Young's modulus. At the third stage at room temperature and at 50 °C the Young's modulus increases again. However, different pattern can be observed in 70 °C and 100°C aging temperatures, where a more complex pattern of increasing and subsequently decreasing seems to be happening. The desegregation process contributing to the negative Young's modulus change is thermally activated and is seen to be most pronounced at the 100°C temperature. At the start of the fourth stage increase in Young's modulus can be observed in all aging temperatures. However, at 100 °C aging temperature this is followed by a continuous decrease in Young's modulus as the aging is continued further.

In the review paper of Baker et al. several distinct aging stages for bake hardening steels were also recognized [49]. These stages occurred up to 10 000 minutes of aging. The first aging stage is Cottrell locking state during which the Cottrell atmospheres form and saturate in the vicinity of dislocations. The second stage is the cluster formation stage, where the aging is attributed to the formation of fine clusters to the saturated Cottrell atmospheres. In the last precipitation stage the tensile strength of the material is further increased and the ductility is decreased with only a small increase in yield strength. This last stage is attributed to the matrix precipitation hardening.

Separate hardening stages have also been observed in dual-phase ferrite-martensite steel. Three different strengthening stages were observed in the study of Waterschoot et al. The first stage similarly to the other studies is the Cottrell's atmosphere forming stage, and the second stage is attributed to carbon cluster forming and carbide precipitation due to further segregation of remaining carbon to the dislocation cores. The third stage is thought to be due to tempering of the martensite. The magnitude of hardening in the precipitation stage is dependent on the interstitial carbon content in the ferrite matrix.[44]

2.3.3 The role of strain in strain aging

Zhao et al. studied static strain aging in a pipeline steel and found that the amount of pre-strain applied to the test specimens affected the amount of high-angle grain boundaries in the samples [45]. The grain boundaries between two grains have varying degree of misorientation between them. High-angle grain boundaries in this case mean grain boundaries with greater than 15-degree misorientation. The amount of high-angle grain boundaries reduced nonlinearly with increasing pre-strain. The 1% and 2% pre-strained samples showed very similar fraction of high-angle grain boundaries compared to the non-pre-strained sample, while 2% pre-strained sample still had slightly lower fraction of them. The 3% pre-strained sample showed significantly less high-angle grain boundaries having only around 34% fraction of them compared to around 66% and 63% fraction in the 1% and 2% pre-strained specimens. The amount of applied pre-strain affects the dislocation density of the specimens with dislocation density gradually increasing as higher pre-strains are used [45][46].

Gündüz studied static strain aging in dual-phase steels and found that increasing the pre-strain measurably increases the ultimate tensile strength (UTS) of steels. However, in the study it was found that increasing the pre-strain negatively affected the increase in stress produced by aging. This is believed to be due to the fact that as dislocation density increases, the amount of dislocations needed to be pinned to achieve similar increase in stress than in lower pre-strained specimens increases [46]. Similar effect on aging susceptibility is reported in study conducted by Seraj et al. The aging susceptibility of manganese-silicon steel was found to decrease as the pre-strain was increased from 5% to 7% [51]. Although increasing the pre-strain seems to cause increase in UTS, De et al. did not find clear correlation between the amount of pre-strain and change in yield stress produced by aging when studying ultra low carbon bake hardening steel [48].

In addition to the amount of applied pre-strain the way the pre-strain is induced may affect the strain aging process. Koyama et al. studied static strain aging of twinning-induced plasticity steel in room temperature and found that both strain rate and strain holding time

had impact on the level of strain aging that occurred. The change in true stress was found to increase linearly as the strain rate or strain holding time increased logarithmically. The authors found that increasing the amount of pre-strain had roughly exponential effect on the change in true stress. The authors credit these effects mostly to be caused by dynamic strain aging during the pre-straining, carbon segregation to dislocations and re-ordering of carbon under external stress. [52]

2.3.4 Grain size and solute atoms

Baker et al. did literature review on bake hardening steels[49]. The paper examines factors affecting the high temperature strain aging process called bake hardening. There seems to be no clear consensus on the effect of grain size in this process. The effect of ferrite grain size on the bake hardening properties of steels have been studied. Generally, studies indicate that finer grain size increases the bake hardening properties of steels. However, multiple other studies do not find correlation between grain size and bake hardening response.

According to the review of Baker et al. [49] low solute atom content is essential in order to keep the bake hardening steel stable at ambient temperatures. The excess carbon levels are kept between 15-25 wt.-ppm to ensure the stability at ambient temperatures. Higher concentrations of solute atoms increase the level of strain aging response and allow the process to occur at lower temperatures, thus allowing aging to happen at room temperature. This is because higher number of solute atoms is available to pin the existing dislocations and the formation of Cottrell atmospheres is more rapid due to higher solute atom content.

2.4 Other possible embrittlement mechanisms the insert

In addition to strain aging there are other embrittlement mechanisms that could affect the cast iron insert in the repository. Although this thesis focuses on strain aging and more specifically on static strain aging it is important to be familiar with other notable forms of embrittlement that could affect the canister insert in the repository especially when the mechanisms could affect the insert simultaneously and synergistically. The synergistic effects of these mechanisms are not well known.

2.4.1 Hydrogen embrittlement

It is well known that hydrogen can diffuse into metals and cause embrittlement of the material. It has been found that the susceptibility for hydrogen embrittlement increases as the ferrite content of the material increases.[53] For this reason the hydrogen embrittlement is important to consider when studying the ductile cast iron with fully ferritic matrix.

The effects of internal hydrogen in ductile cast iron have been previously studied by Matsunaga et al. In the study it was found that hydrogen charging resulted in marked decrease in the percentage reduction of area. Most of the hydrogen was found to be diffusive and segregate at the graphite/ferrite matrix interface and in cementite of pearlite. The fracture mechanism was found to change due to the hydrogen charging and there appeared to be interconnecting cracks between neighboring graphite nodules unlike in the fully ductile fracture of the as received material. [54]

Hydrogen embrittlement in the canister insert material has been previously studied by Forsström et al.[55] and Sahiluoma et al. [56]. In both studies the hydrogen charging was

found to markedly reduce the total elongation of the material as well as reduce the time to fracture in constant load testing. In both studies the complete change of fracture mechanism was observed, and the matrix of the hydrogen charged specimens was found to crack by brittle cleavage fracture mechanism.

In the work of Sahiluoma the hydrogen uptake of the cast iron was found to increase markedly during plastic deformation. The hydrogen charging reduced the elongation to fracture and time to fracture in slow strain rate testing and in constant load testing. In thermal desorption spectroscopy (TDS) two distinct peaks for hydrogen desorption were observed, one between 400 and 500 K and one at 600 K with heating rate of 10 K/min. The author attributed the lower temperature peak between 400 and 500 K to correspond to hydrogen trapped at small voids and cracks in the ferrite matrix and at the interface of graphite nodules. The Higher temperature peak at 600 K was attributed to the hydrogen trapped in the graphite nodules.[56] In the study of Forsström et al. the hydrogen desorption was found to manifest in three different peaks at temperature of 400 K, 500 K and 700 K with heating rate of 6 K/min. The peak at 400 K was found to shift to 450 K under load and when the absorbed hydrogen content is increased significantly. The peak at 500 K was found to shift towards 560 K with hydrogen charging but had no significant response to increased loading.[55]

2.4.2 Radiation embrittlement

As the nuclear fuel decays, it emits radiation that can have impact on the canister structure. The ionizing radiation can cause damage in the crystalline structure of the cast iron insert, possibly contributing to redistribution of atoms and rejection of solute atoms from the crystal. This could affect the chemical composition of the insert and may increase the risk of failure.

The effects of neutron-irradiation have been studied extensively on the steel alloys and weld metals used in the nuclear reactor pressure vessels (RPVs). The growing understanding of the phenomenon has caused closing of at least one facility. There are several different mechanisms behind the radiation embrittlement. One of the mechanisms is the generation of point defects such as interstitials and vacancies and dislocation loops in the material. It has been shown that these defects are mostly repaired by diffusion but over time the defects can accumulate and alter the material properties. Other important hardening mechanism is the development of Cu-rich nanoclusters or precipitates in the material, which is accelerated by the neutron irradiation induced high vacancy concentration. In steels it has been found that the alloy content is strongly correlated with the level of neutron embrittlement and the tendency for the neutron embrittlement can be reduced or eliminated in certain temperatures by reduction of the residual element content in the material. Copper has been found to be the single most harmful alloying element regarding the cluster formation, but nickel and manganese have later been found to also exacerbate the formation of the Cu-rich nanoclusters synergistically. As the diffusion can repair most of the defects induce by neutron irradiation, the embrittlement effects are lesser in higher temperatures and get more severe as the irradiation temperature is lowered.[57]

The hardening and embrittlement which is induced by clustering of Cu particles is well known in pressurized water reactors that are mostly composed of alpha ferrite. [58] The studies of Brissonneau et al. raised concerns that similar aging process due to radiation

enhanced solute clustering could occur in the cast iron and lead to degradation of the mechanical properties of the insert [59]. However, later report by Olsson et al. studying the irradiation induced Cu clustering in cast iron FeCu alloy found that no hardening due to Cu precipitation occurred in the cast iron during one week of electron irradiation. In the study the acceleration rate was estimated to be 2750 meaning that the one week irradiation would correspond to 45 years in the storage conditions.[58] The safety regarding irradiation induced Cu precipitation was also confirmed in the work of Chang. In the study no Cu precipitation was found in the cast iron samples after one week of 2 MeV electron irradiation.[60] In latest report regarding irradiation induced damage in the insert it was concluded that the irradiation should have no significant impact on the mechanical properties after 10 000 years.[61]

3 Methods

3.1 Material and sample preparation

The material used for the experiments is spheroidal graphite cast iron of grade EN-GJS-400-15U. The piece of the cast iron insert where the specimens are manufactured is from the casting I73 and the piece of the cast iron insert was provided by Posiva Oy. The chemical composition of the cast iron insert is presented in table 3.

Table 3 Chemical composition of cast iron grade EN-GJS-400-15U from casting 173 in wt.%

C	Si	Mn	S	P	Ni	Cu		Mg	Fe
3.48	2.48	0.22	0.004	0.01	0.04	0.02		0.04	Bulk

Several blocks of material were cut from the cast iron insert close to the insert surface to manufacture tensile specimens for the tensile tests. The material is cut from the insert according to figure 16. The tensile specimens were cut with electro-discharge machining (EDM) according to geometry show in figure 17. The EDM affected surface layer of the tensile specimens was removed from the gauge section using mechanical grinding. For the grinding 320 grit emery paper was used first and then the surface was finished with 500 grit emery paper. For the tensile tests measured with digital image correlation the specimens were only ground with 320 grit emery paper to ensure good contact between the paint and the specimen. As the grinding removed some material and because the cross-section area changes during the pre-straining, each specimen was measured before the pre-straining and before the final tensile test.
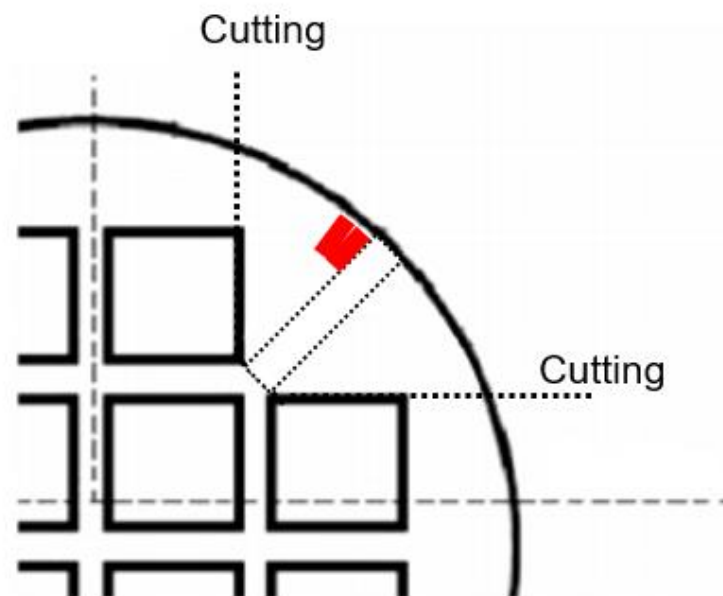
Figure 16 Locations where the tensile specimens were cut from the casting I73 marked in red.
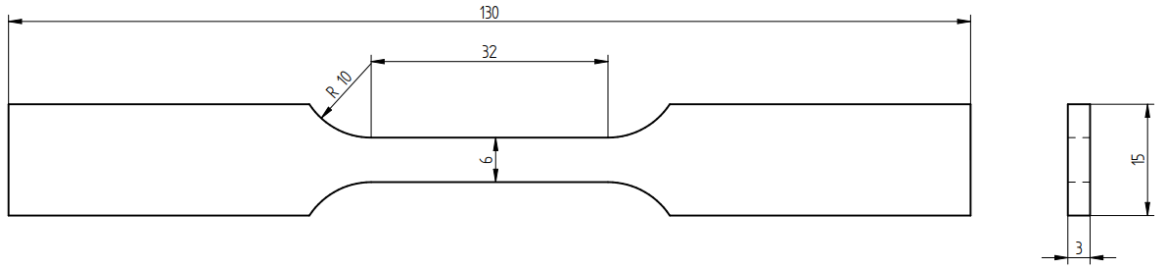
Figure 17 Tensile specimen geometry

3.2 Experimental methods

Constant extension rate tensile testing (CERT) was used for the tensile specimens in room temperature. The extension was measured with an extensometer. To observe the reference behavior of the as-received material a basic tensile test was conducted. The other specimens were first strained to the nominal pre-strain of 1%, 2% or 3% with constant extension rate of 0.016 mm/s and then the load was removed with constant speed of 0.10 mm/s. The specimens were strained a little over the nominal strain to achieve plastic strain that is close to the nominal value. The specimens were strained to total strain of 1.15%, 2.15% and 3.15%. The samples were then aged at room temperature, 100 °C, 200 °C, 300 °C and 400 °C for different durations to induce static strain aging. For the 100 °C and 200 °C aged specimens aging times of 1 day and 11 days were used. 300 °C and 400 °C specimens were aged for 1 day. Additionally, two specimens were aged at 100 °C and at 200 °C without pre-straining them first to study if any aging would occur in the specimens due to possible residual strains. The room temperature samples were aged for even longer time of 84 days. After the aging treatment the specimens were removed from the furnace and cooled down in room temperature for 30 min to 1 hour. After the specimens were cooled down tensile tests were conducted with the same constant extension rate of 0.016 mm/s. The tensile tests were done during the same day after removing the samples from the furnace to minimize the possibility of further aging at room temperature.

It should be noted that during the 11-day aging process for the 100 °C and 200 °C specimens there was an approximately two-hour power outage that occurred, during which the heat treatment furnaces were shut down. During this time, the temperature inside the furnaces dropped somewhat significantly, by about 20 °C in the 100 °C furnace and by an unknown amount in the 200 °C furnace. However, it is quite safe to assume that the possible effects of this are minimal and negligible in such prolonged aging.

The microstructural samples for specimens 1 and 11 were cut from the wide ends of the tensile specimens after the tensile testing was conducted. The other microstructural samples were cut from the as received material in locations that correspond to the locations where all the tensile specimens were cut from (Same distance from the insert surface right next to the specimens). The specimens were hot mounted using Struers multifast resin and prepared using wet grinding with up to 2400 grit paper and then polished using diamond paste first with 3-micron particle size and then 1 micron particle size. For the etching of the sample surfaces 2% Nital solution was used.

3.3 Digital image correlation (DIC)

Digital image correlation is optical method that is used to measure the full-field coordinates and displacements from the surface of the test specimen by taking a sequence of images of a pattern on the surface of specimen. For accurate measurement the pattern on the surface of the specimen, whether it is applied or not, should accurately follow the deformation of the material. This is the fundamental assumption behind the whole measurement process. The images taken from the pattern can be used to generate full field coordinates of the shape, motion and deformation of the test piece and the coordinate fields can in turn be used to calculate displacements, strains, strain rates, velocities and curvatures. [62]

The main benefit of the full field measurements compared to traditional point measurements with strain gauges is that the full field measurements enable the measurement of localized deformation and gives more information of how the strain evolves in the specimen during testing.

As the whole DIC measurement is based on the assumption that the pattern accurately follows the deformation of the specimen, the pattern is the most essential part to successful DIC data. For optimal measurements, the pattern feature size should be 3-5 pixels regardless of whether the pattern is light or dark. In local DIC the coordinate point depends on a small subset of the image in the vicinity of the given point. Each measurement point is centered inside a subset. Each subset should contain enough information so that it can be distinguished from all the other subsets in the region-of-interest. A subset should include a minimum of three features of the pattern in all directions. The spacing between the measurement points is called step size.[62]

DIC was carried out on some samples to obtain full field strain measurements of the strain aged specimens. A reference tensile test in room temperature as well as pre-straining and tensile testing of strain aged specimens were conducted using DIC. The software used for the DIC measurements was Vic-3D.

For the DIC tests the speckle pattern was applied with spray paint. A white base coat of paint was sprayed to the specimen surface to increase contrast and black spray paint was used to apply the small speckles to the specimen surface. A laser printed tattoo paper was first used to apply the pattern for the reference tensile test but, the usage of the tattoo paper was rejected due to it not following the deformation of the specimens accurately. Excessive stretching of the tattoo paper was observed at locations where there were no visible signs of localized yielding. All the DIC experiments that are reported in results were carried out using spray painted speckle patterns.

A reference tensile test for the as received material was carried out using constant crosshead speed of 0.016 mm/s. Additionally three specimens were pre-strained to 1%, 2% and 3% nominal pre-strain while the deformation was measured with DIC. As the strain data from the DIC measurements is not available live during the tensile testing a predetermined crosshead displacement was used to induce the specified amount of pre-strain. Crosshead displacements of 0.95 mm, 1.3mm and 1.7 mm were used to achieve the nominal strains of 1%, 2% and 3%. These crosshead values are approximations based on data from the previous tests. After this the specimens were aged at 100 °C for 1 day. Finally, CERT using DIC was

conducted for the specimens with same crosshead speed of 0.016 mm/s. The speckle pattern was removed from the specimen surface with acetone before the aging. After the aging was completed the base paint coat and speckle pattern was reapplied to the specimen surface.

The DIC images were recorded every 500 milliseconds during the tensile tests. For the DIC calculations subset size of 23 pixels and step size of 5 pixels was used for all the samples. The spatial resolution of the images was between 48 and 49 pixels/mm. As the crosshead speed was quite slow and data acquisition rate was quite high the DIC calculations for the tensile experiments were done using every 12th image from all the captured images to reduce noise in the data. Additional DIC calculation was made using all the captured images to examine the strain localization at the start of the yielding (after yield point) since the time interval of 6 seconds between every 12th image was too long to closely follow how the strains develop during the onset of yielding. This calculation was also used to plot the stress-strain and stress-time curves of the experiments. For the pre-straining and unloading the DIC calculations were done using every 6th image from all the captured images because the total displacements were so much smaller than in the tensile experiments that every 12th image would have included too little data.

In materials with yield point the plastic deformation usually nucleates as a band at certain location and propagates uniformly at a front through the specimen during the yield plateau or Lüders strain. These bands are referred to as Lüders bands. The formation of Lüders bands occurs at the onset of plastic deformation in the material. Although the band propagating trough the specimen at front is the typical behavior, the development of Lüders bands can also be more complex and less uniform in some cases. The complex arrays of Lüders bands are often referred as stretcher strains but they are still Lüders bands.[39]

In this work all localized bands of deformation in the specimens are referred as Lüders bands. The digital image correlation allows tracking the nucleation and propagation of possible Lüders bands in the tensile specimens. The DIC method enables us to see where the deformation starts in the different specimens (i.e. where the Lüders bands nucleate) and how the plastic deformation propagates trough the material and finally how the plastic deformation localizes before leading to fracture.

4 Results

4.1 CERT

Pre-straining

The stress-strain curves of pre-straining and unloading of all the specimens compared to the reference tensile test are shown in figures 18-21. From the figures it is evident that the yielding behavior of the as-received material is almost identical to the pre-strained specimens in the pre-straining region. The yielding is smooth and typical for ductile cast iron without a clear yield point.
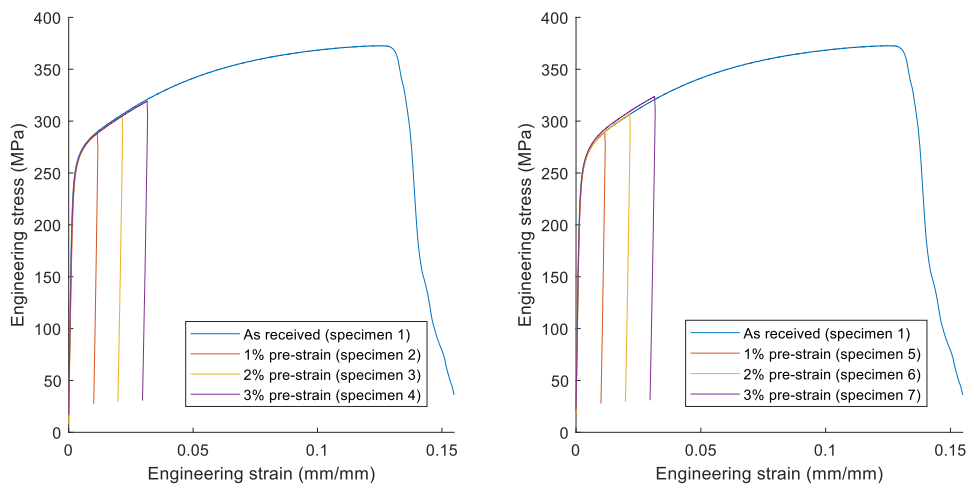
Figure 18 Pre-straining and and unloading of specimens 2,3,4,5,6 and 7 presented in stress-strain curves and compared to the reference tensile test of specimen 1.
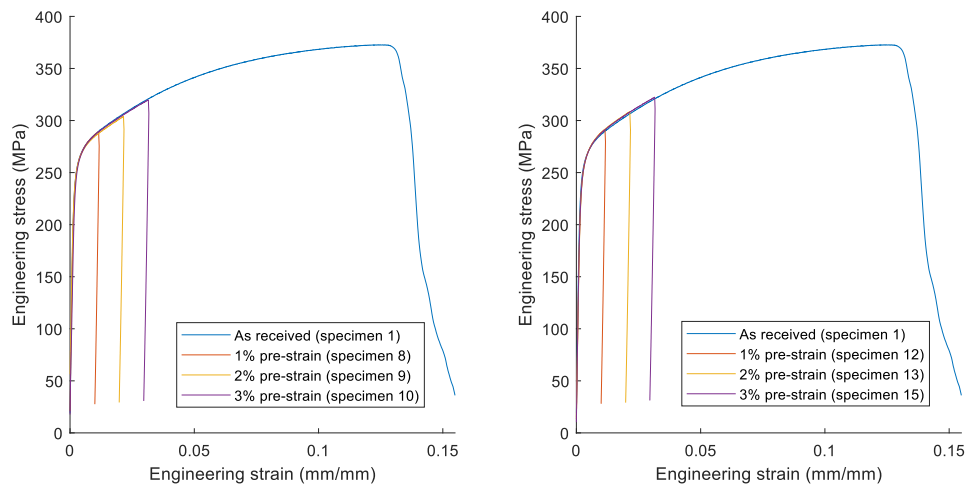
Figure 19 Pre-straining and and unloading of specimens 8,9,10,12,13 and 15 presented in stress-strain curves and compared to the reference tensile test of specimen 1.
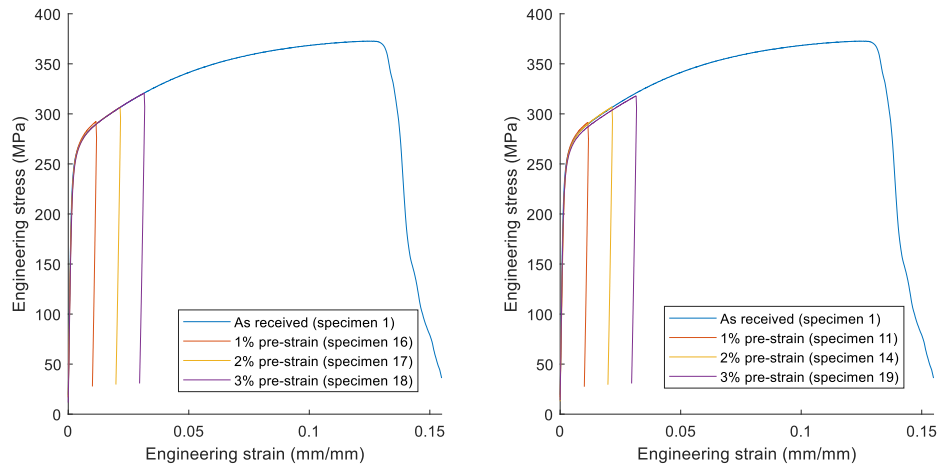
Figure 20 Pre-straining and and unloading of specimens 16,17,18,11,14 and 19 presented in stress-strain curves and compared to the reference tensile test of specimen 1.
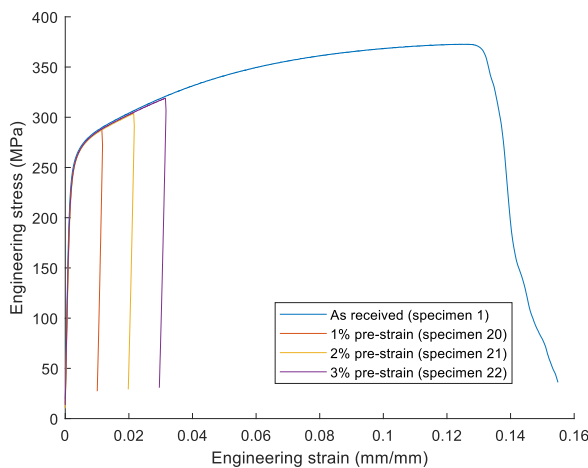
Figure 21 Pre-straining and and unloading of specimens 20,21, and 22 presented in stress-strain curves and compared to the reference tensile test of specimen 1.

Tensile tests of aged specimens

The stress-strain curves of the aged specimens compared to the reference tensile test can be seen in figures 22-28. The stress-strain curves comparing the same pre-strain level with 1 day aging time at different aging temperatures can be seen in figures 29-31. It can be clearly observed that the static strain aging of the specimens brings pronounced yield point to the material behavior for all the observed pre-strain levels, temperatures, and aging times. The yield stress clearly increases as the amount of pre-strain is increased with the yield point being very consistent for the same pre-strain level across different specimens, which suggests that the newly formed dislocations are effectively locked during the strain aging. There seems to be some yield point elongation that increases as the pre-strain is increased although the lower pre-strain levels do not show clear yield plateau. There is no clearly observable difference in the yield stress between 100 °C and 200 °C aged specimens and between the 1 day and 11-day aging time. This suggests that the static strain aging effect observed is due to the formation of Cottrell atmospheres and locking the newly formed dislocations. The formation of the Cottrell atmospheres and the locking saturates already

43

during the 1-day aging period at temperature of 100 °C. From figures 29-31 it seems that aging in 300 °C and 400 °C results in a lower increase of the yield stress compared to aging at 100 °C and 200 °C and after aging at 400 °C the yield point is clearly less pronounced. The differences in the yield point increase between the 300 °C aged specimens compared to the 100 °C and 200 °C aged specimens gets larger when the pre-strain is increased. The specimens aged at room temperature show significantly smaller increase in the yield stress than the specimens aged at 100°C and 200 °C. The increase in yield stress is similar to the samples aged at 300 °C.

The effects of the aging on the total elongation of the specimens cannot be accurately judged, because the material seems to have a lot of variation between specimens when it comes to the total elongation. However, by combining the results it is clear that the strain aging reduces the total elongation to some extent even when the pre-straining is taken into account. During the testing some small pores were visible on the surface of some of the specimens. It should be noted that some of the specimens fractured outside of the extensometer gauge length, which can be seen in the stress-strain curves as the elastic stress returns to zero in straight line after the fracture point.

The specimens aged at room temperature seem to have better total elongations than the specimens aged at higher temperatures. It should be noted that although the yield strength levels of the specimens aged at RT and 300 °C are similar the RT specimens seem to have better elongation to fracture and slightly lower strain-hardening rate. The variation in the total elongation of the specimens is probably partly due to various casting defects present in the material as well as the difference in the microstructure in different parts of the cast.
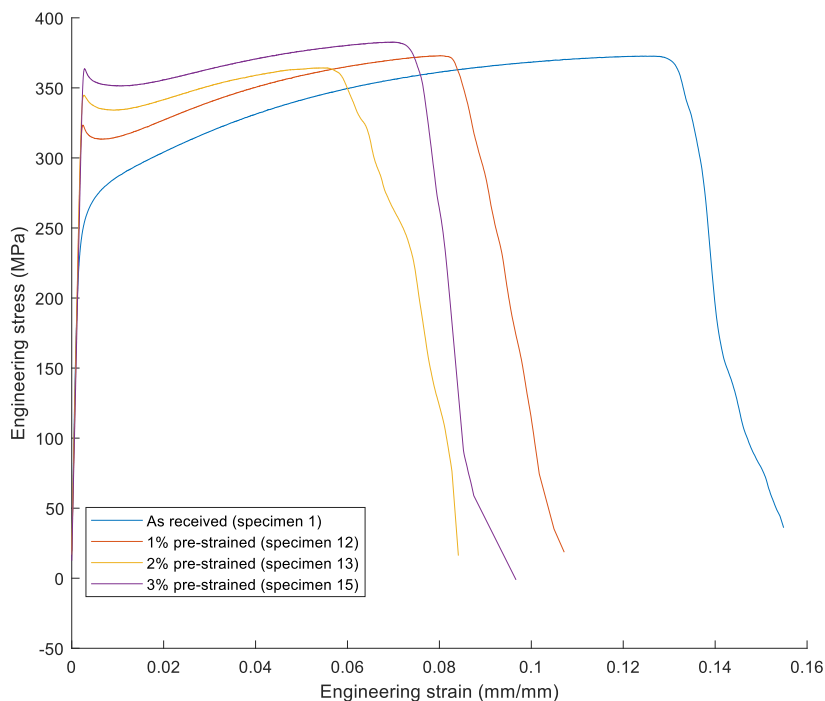
Figure 22 CERT stress-strain curve for specimens aged at 100 ℃ for 1 day.
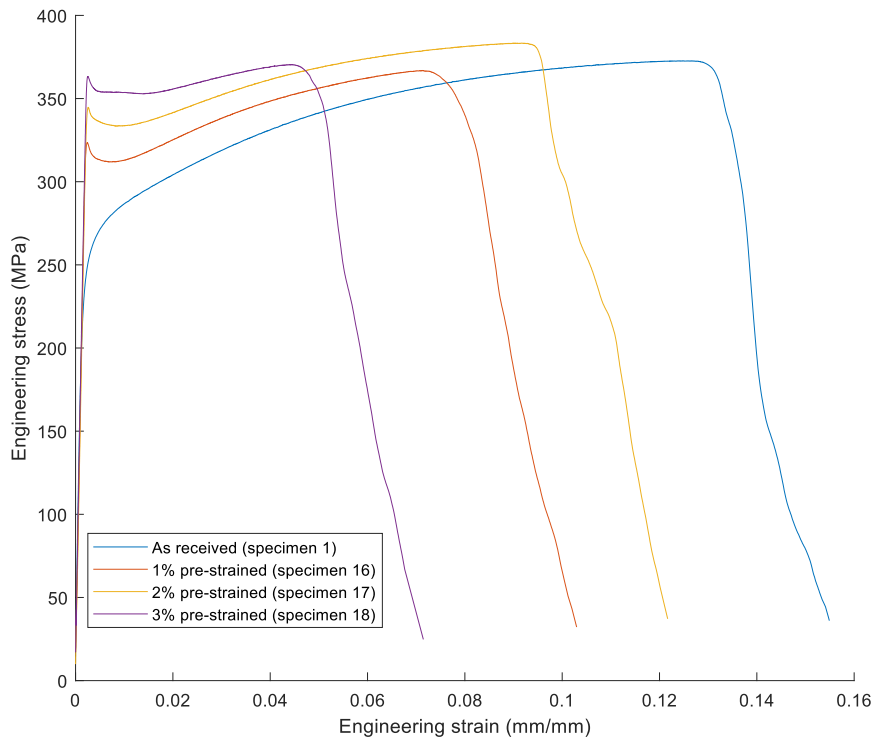
Figure 23 CERT stress-strain curves for specimens aged at 200 ℃ for 1 day.
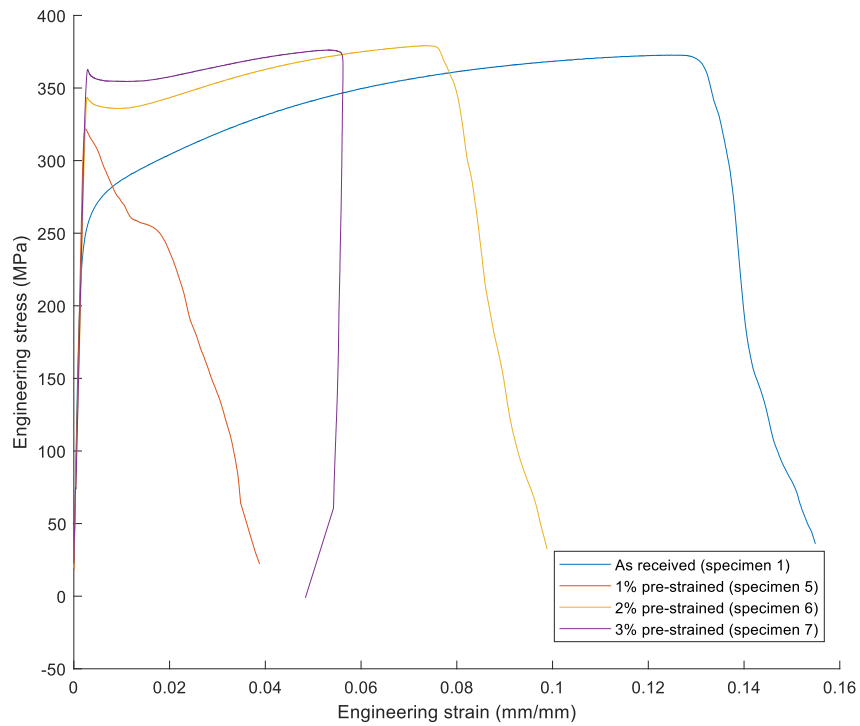
Figure 24 CERT stress-strain curves for specimens aged at 100 ℃ for 11 days.
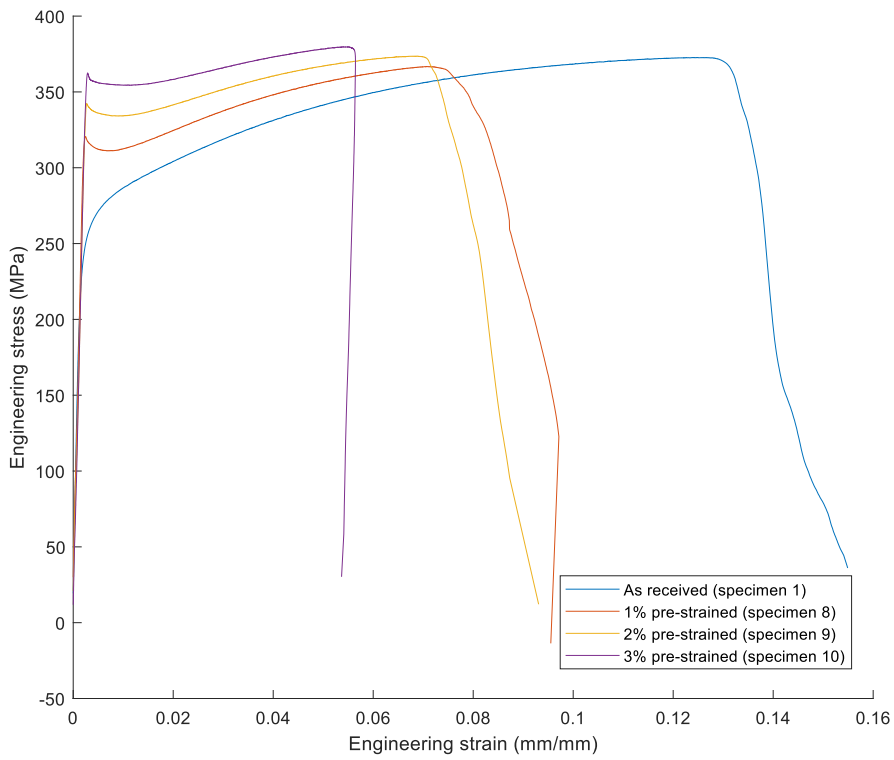
Figure 25 CERT stress-strain curves for specimens aged at 200 ℃ for 11 days.
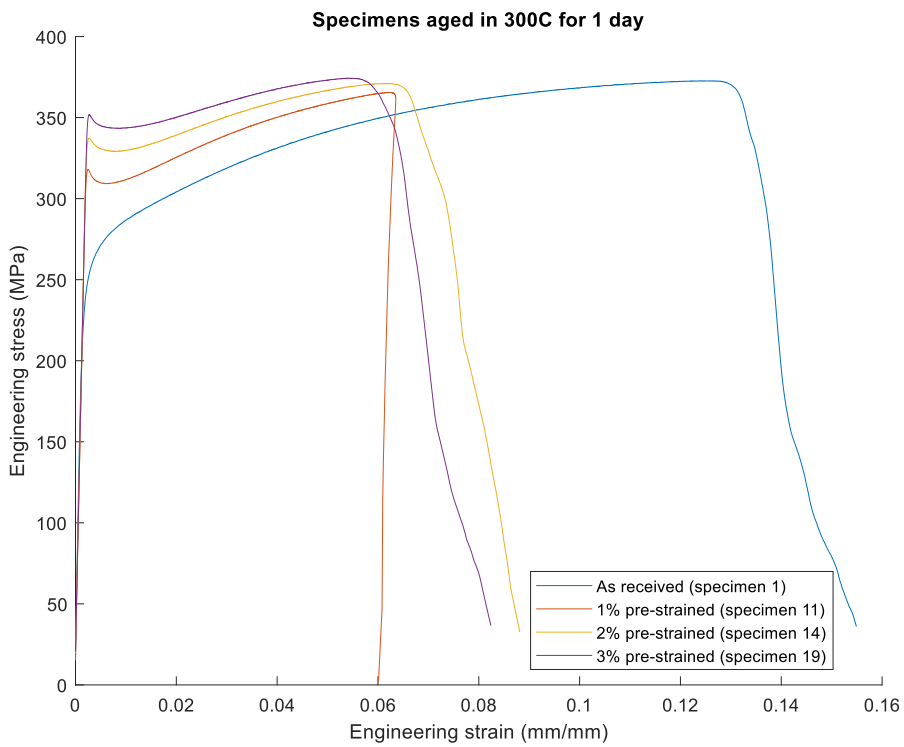
Figure 26 CERT stress-strain curves for specimens aged at 300 ℃ for 1 day.
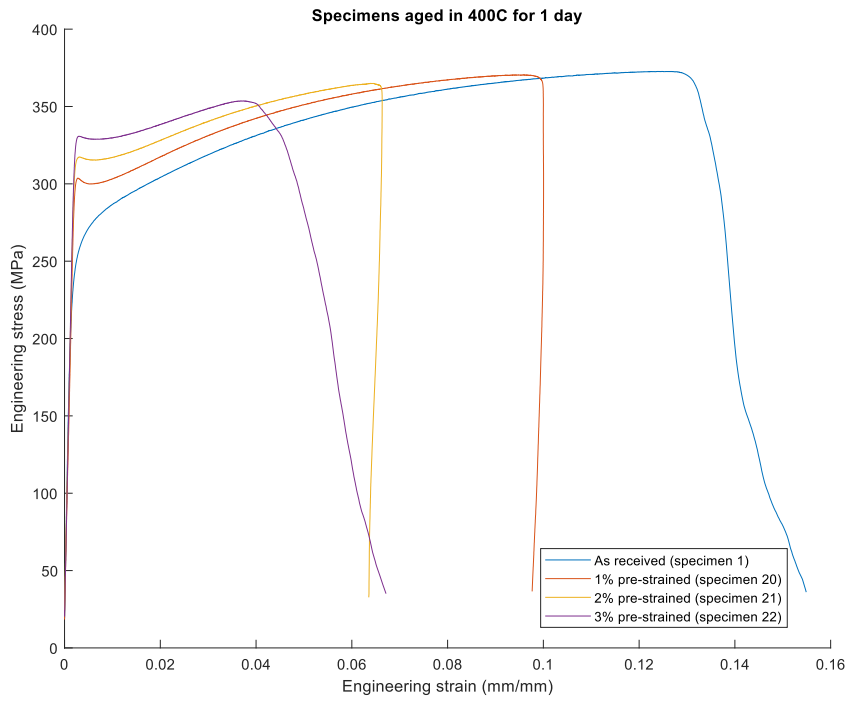
Figure 27 CERT stress-strain curves for specimens aged at 400 ℃ for 1 day.
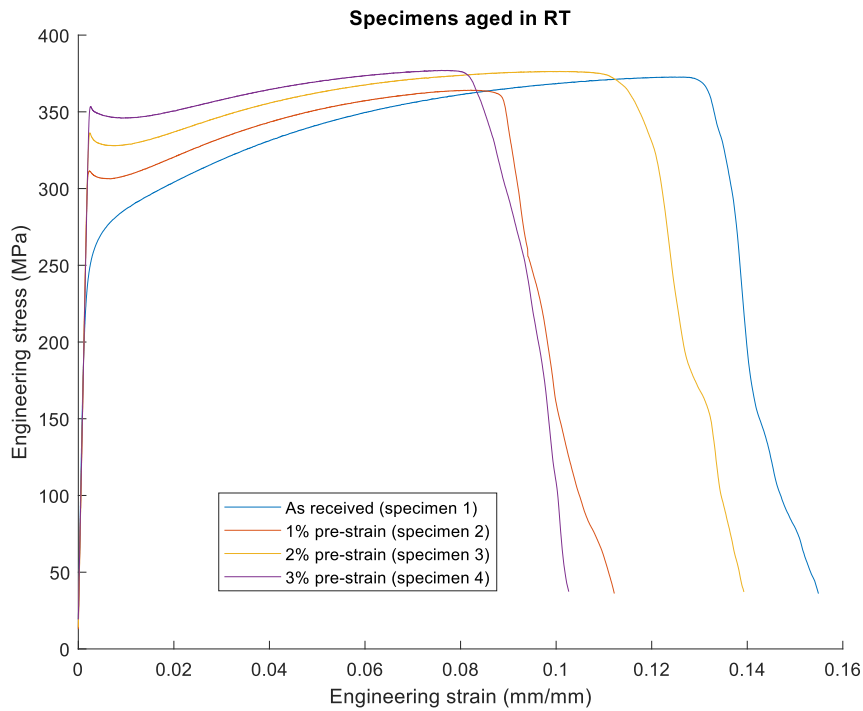
Figure 28 CERT stress-strain curves for specimens aged in room temperature for 84 days.
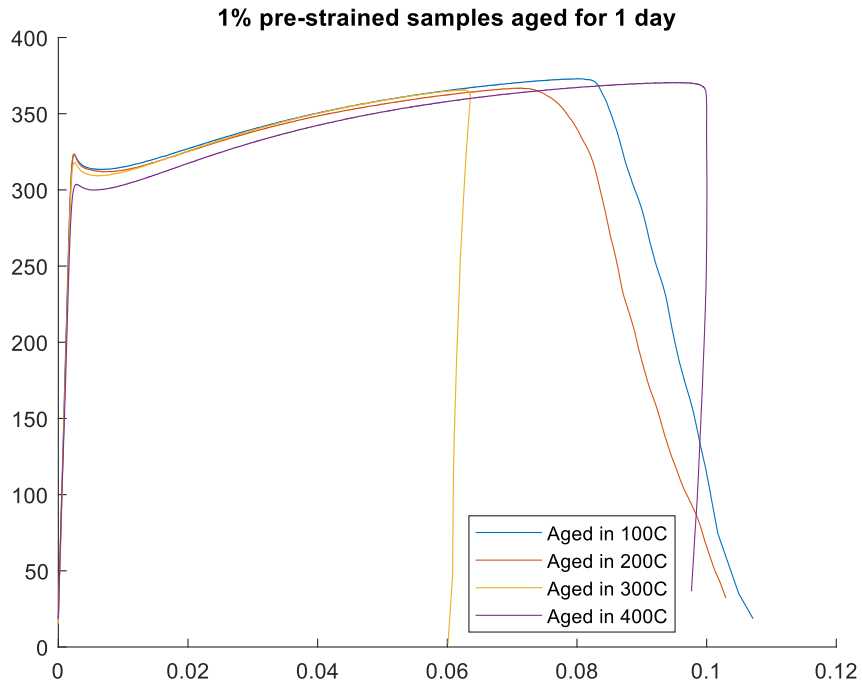
Figure 29 CERT stress strain curves for 1% pre-strained samples aged for 1 day in different temperatures.
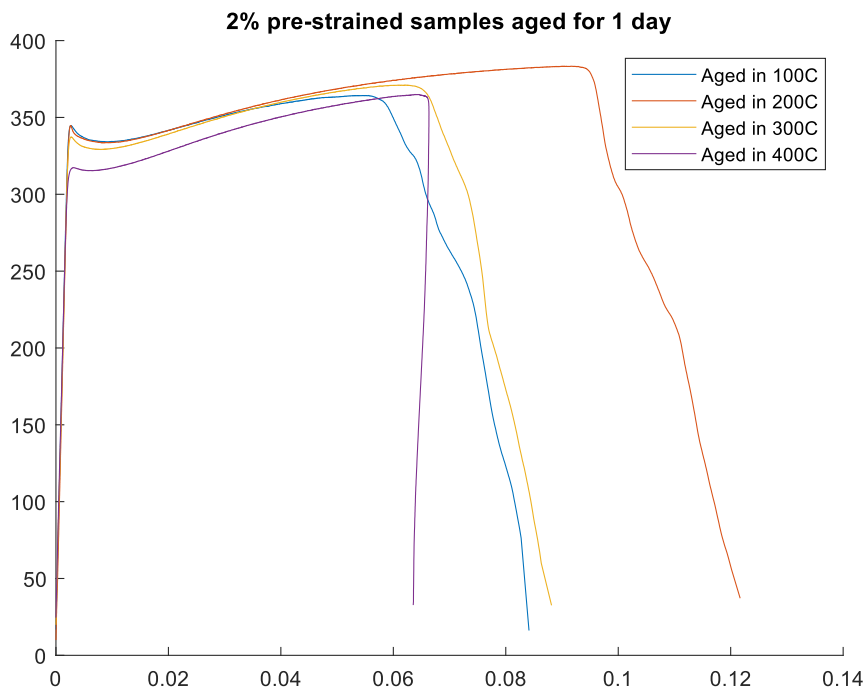
Figure 30 CERT stress strain curves for 2% pre-strained samples aged for 1 day in different temperatures.

48
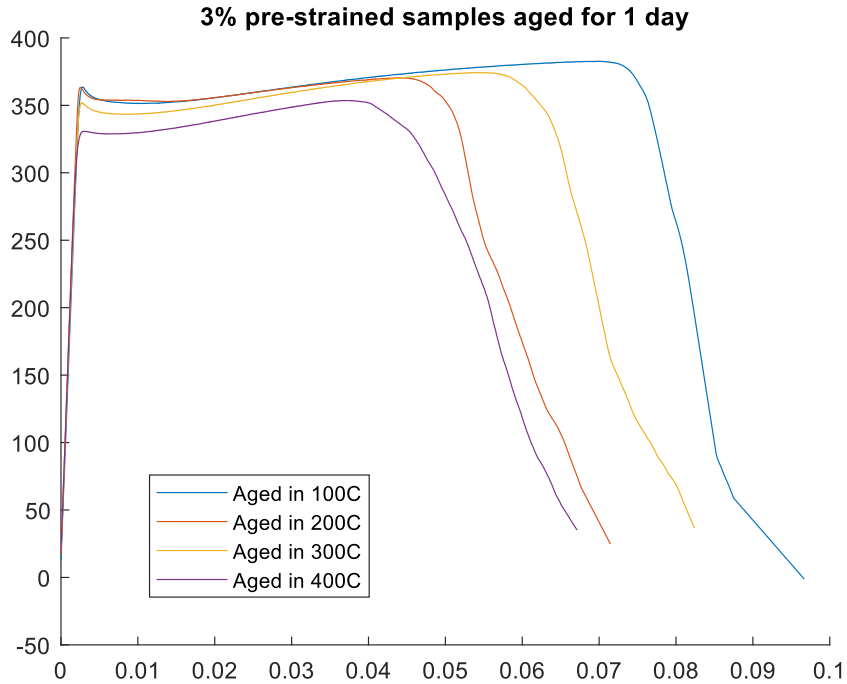
Figure 31 CERT stress strain curves for 3% pre-strained samples aged for 1 day at different temperatures.

The CERT results of the non-pre-strained and aged samples compared to the as received material are shown in figure 32. The aged specimens follow almost identical yielding behavior compared to each other and to the reference tensile test done at room temperature, until each specimen fractures at different elongation. There is no clearly observable aging that occurs without pre-straining in these specimens. The difference in elongation to fracture can be explained by the natural scatter in the material. The small differences in the 0.2% proof stress are probably due to the small differences in the microstructure of the material or measurement error rather than the aging. The two aged specimens are located closer to the surface of the insert than the as-received specimen.
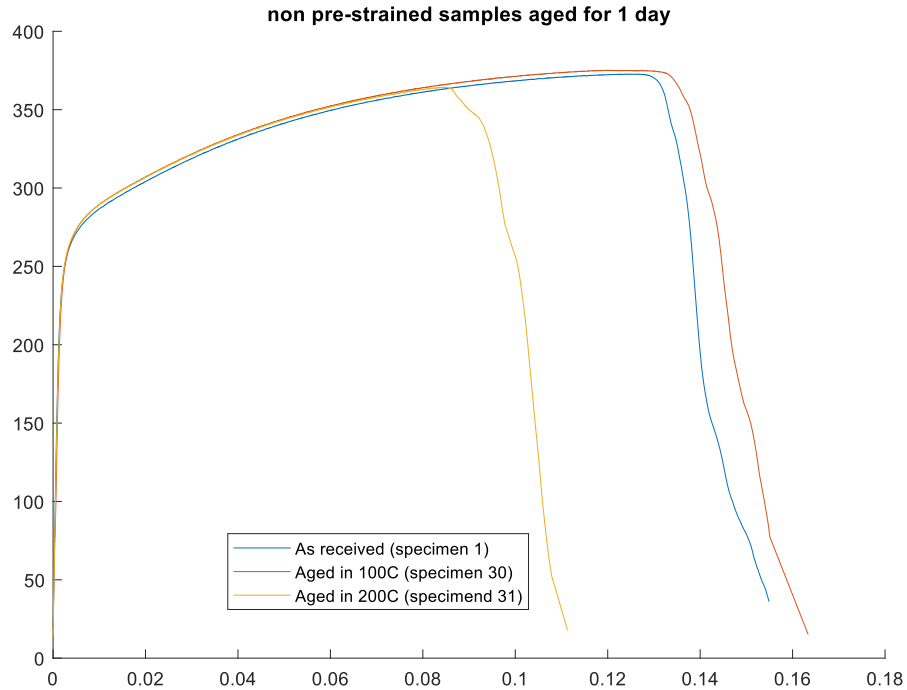
Figure 32 **Stress-strain curves of non pre-strained samples aged at 100 ℃ and 200 ℃ for 1 day compared to asreceived material.**

The results of the tensile experiments are combined in table 4. The yield ratio (YS/UTS) increases remarkably as the result of static strain aging. The yield ratio seems to increase as the pre-strain is increased rising to values of over 0.95 for the 3% pre-strained samples. The yield ratio changes quite drastically even at the pre-strain levels of 1%, increasing over 20% compared to the reference sample. The increase in yield ratio seems to be lower for the specimens that are aged at 400 °C and 300 °C. However, the difference between the specimens aged at 300 °C, 200°C and 100°C is small and can be attributed to the variations between the specimens.

The yield stress increase produced by aging seems to get larger as the pre-strain is increased. However, when aged in 400 °C for 1 day the yield stress increase produced by aging gets smaller as the pre-strain is increased.

Instead of total elongation at fracture the elongation at the highest stress/force is reported since some of the specimens fractured outside the gauge length of the extensometer and the extensometer data after the elongation starts to localize is not available for all the specimens. However, it is worth noting that by looking at the graphs the uniform elongation A_{gt} (elongation at maximum force) and the elongation at fracture A_t are in practice very close to each other for the studied material. The A_{gt} value in this case just makes possible to compare the data between specimens without approximations.

Table 4 CERT results

Pre-strain	Specimen ID	Aging temperature (℃)	Aging time (h)	Yield Stress (MPa)	Ultimate tensile strength (MPA)	Yield ratio	Increase in yield stress produced by aging (MPa)	Elongation at maximum force A_{gt} (%)
0 % (as received)	1	-	-	264	373	0.708		12.5
1 %	2	25	2016	311	364	0.854	23	8.4
	12	100	24	323	373	0.866	32	8.0
	5		262.5	322	322	1	33	0.24
	16	200	24	323	367	0.880	31	7.1
	8		262.5	321	367	0.875	31	7.1
	11	300	24	318	365	0.871	27	6.2
	20	400	24	304	370	0.822	15	9.6
2 %	3	25	2016	336	376	0.894	31	10.1
	13	100	24	344	364	0.945	36	5.5
	6		262.5	344	379	0.908	37	7.4
	17	200	24	345	383	0.901	38	9.2
	9		262.5	342	374	0.914	38	6.9
	14	300	24	337	371	0.908	30	6.3
	21	400	24	317	365	0.868	13	6.4
3 %	4	25	2016	353	377	0.936	34	7.6
	15	100	24	364	383	0.950	41	7.0
	7		262.5	363	376	0.965	39	5.4
	18	200	24	363	370	0.981	43	4.5
	10		262.5	362	380	0.953	43	5.5
	19	300	24	352	374	0.941	34	5.4
	22	400	24	331	354	0.935	12	3.8

4.2 DIC

Pre-straining the samples

The full-field strain measurements from the pre-straining and unloading of the specimens are shown in figures 33-35. Each of the images show five snapshots of the strain measurements during the pre-straining. The first four snapshots show the strain measurements as the specimen is loaded and the final image shows the remaining strains after the specimen is unloaded. For specimen 29 the time during the last snapshot is not available since the returning crosshead speed for the unloading was mistakenly set to a slower value and the DIC measurements were paused during the unloading. However, the DIC measurements were continued after the unloading and the final snapshot shows the remaining strains after the specimens is completely unloaded.
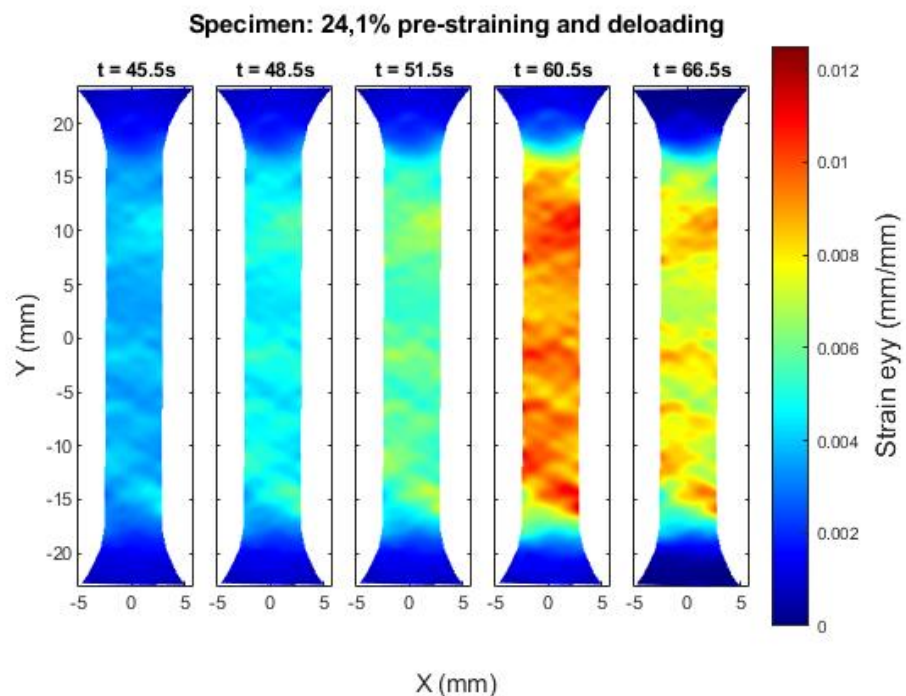
Figure 33 Full-field strain measurements of specimen 24 showing the strain in Y-direction (e_{yy}) at different times during the 1% pre-straining process.
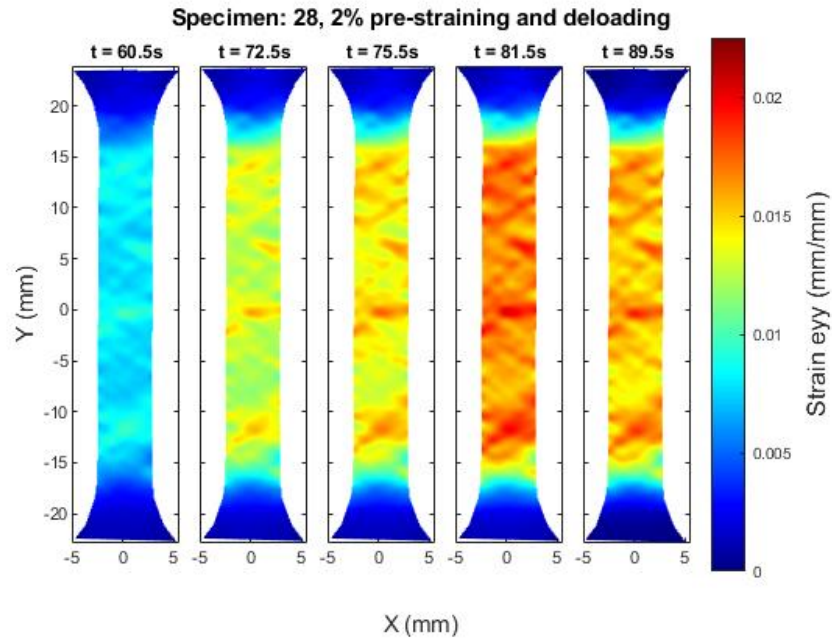
Figure 34 Full-field strain measurements of specimen 28 showing the strain in Y-direction (e$_{yy}$) at different times during the 2% pre-straining process.
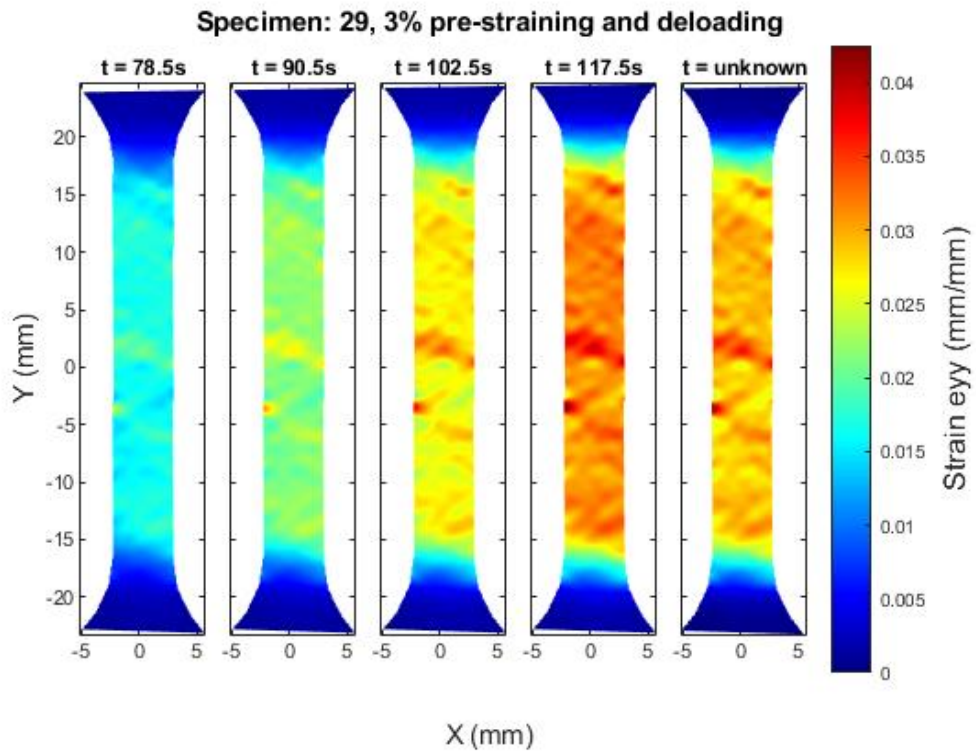
Figure 35 Full-field strain measurements of specimen 29 showing the strain in Y-direction (e$_{yy}$) at different times during the 3% pre-straining process.

Tensile tests

Stress-strain curves from the CERT tests done using DIC are shown in figure 36. The curves are plotted using analog force data from the force sensor and digital strain data acquired through the DIC software using its digital extensometer function. Figure 37 shows the stress-time curve of the tensile tests. The time data in figure 37 is calculated from the DIC image index with the picture time interval to get the time curve that corresponds to the time stamps of the DIC images accurately.
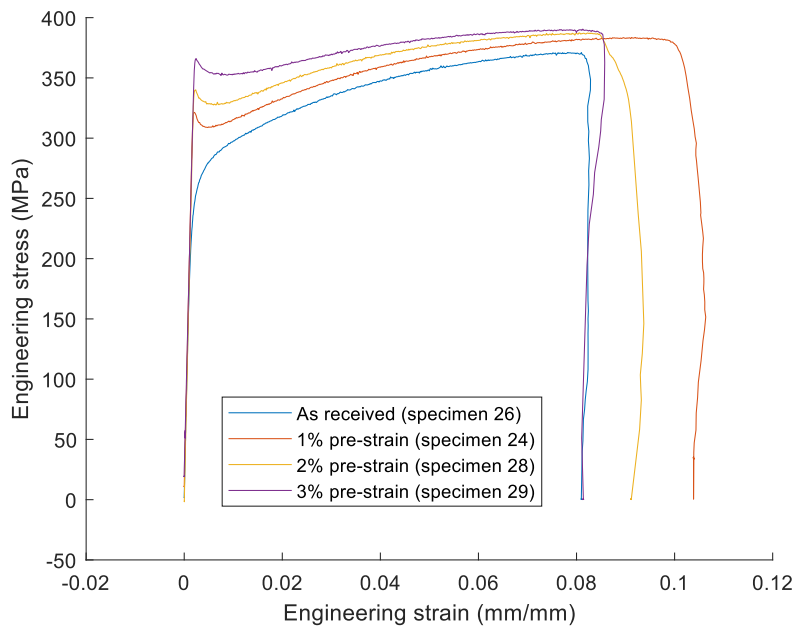
Figure 36 Stress-strain curves of specimens 26, 24, 28 and 29
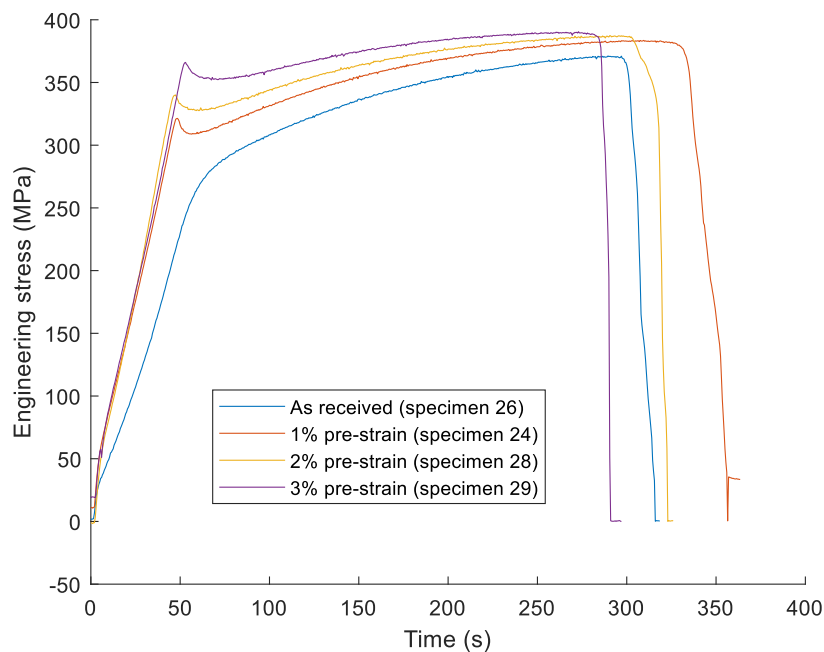
Figure 37 Stress-time curves of specimens 26, 24, 28 and 29

Figures 38-41 show the full-field strain measurements after the onset of yielding in each specimen. Fig. 38 shows the deformation of the as received specimen after the onset of yielding. As expected, there is no Lüders deformation in the specimen 26 as the specimen yields continuously without pronounced yield point. The deformation in specimen 26 seem to nucleate from the specimen shoulders but after that the deformation will quickly propagate through the whole gauge length. The start of the uniform elongation is almost instantaneous. There is no clear Lüders bands observed in specimen 26 and instead the deformation seems to appear as large amount of non-defined diffuse bands that randomly develop throughout the gauge length resulting in uniform elongation shortly after the onset of yielding.
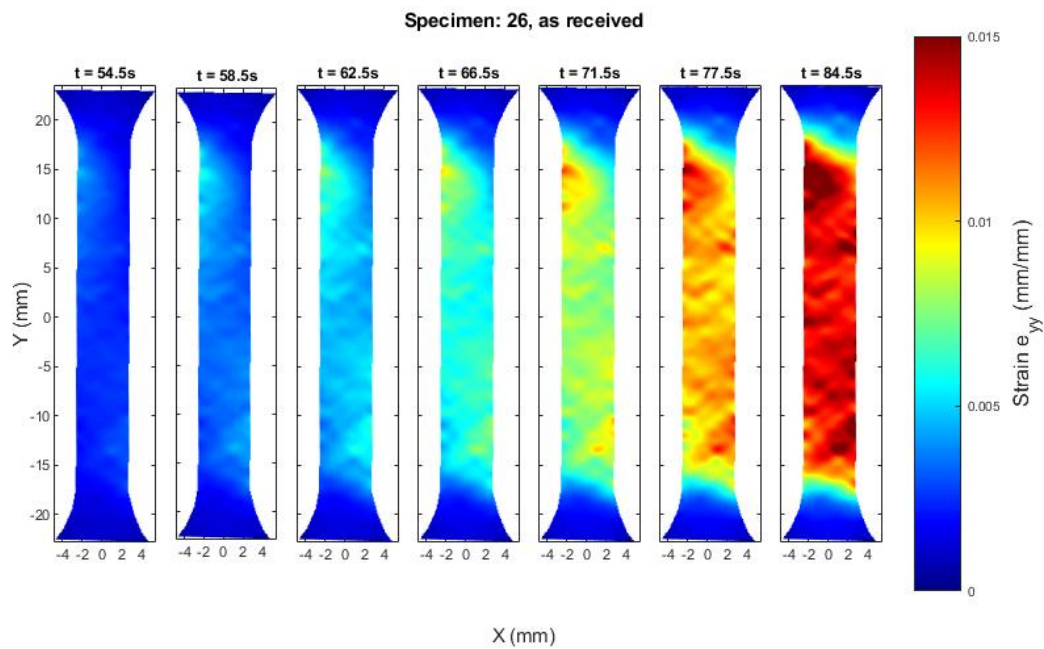
Figure 38 Full-field strain measurements of specimen 26 after the yielding starts. The figure shows fast nucleation of multiple diffuse deformation bands across the whole gauge length indicating the absence of Lüders effect and immediate start of uniform elongation.

Fig. 39 shows the full-field strain measurements of the specimen 24 after aging. The specimen 24 seems to have Lüders deformation to some extent. The deformation is much more localized than in the as received specimen as multiple distinct Lüders bands seem to nucleate from both specimen ends. However, the effect is not very typical Lüders deformation as there is no clear band fronts propagating trough the gauge length, but the bands seem to get stuck shortly after nucleation causing strain localizations in these areas.
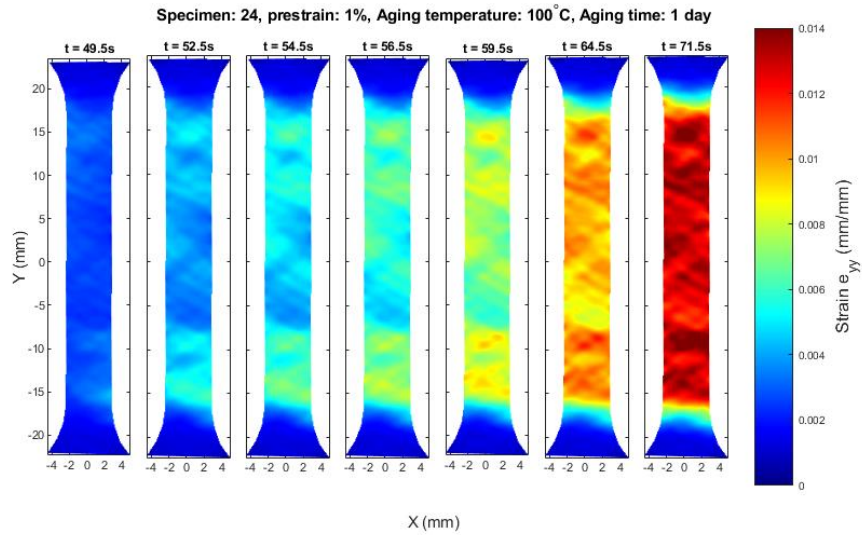
Figure 39 Full-field strain measurements of specimen 24 after the yield point showing complex nucleation of and propagation of multiple Lüders bands.

Fig. 40 shows the strain measurements of specimen 28 after the yield point. The specimen 28 shows Lüders effect to higher extent as there seems to be distinct Lüders band nucleating from one end of the gauge length and propagating towards the other end of the specimen. However, the Lüders band does not seem to have definite front as there is no clear front between un yielded and yielded material. The band front seems to be diffuse as the material yields more inside the band than at the front. This Lüders band seems to get stuck at around third of the gauge length not propagating further. The other end of the specimen does not show typical Lüders type deformation and the yielding starts similarly to the as received material with some diffuse type Lüders bands forming randomly across the specimen until somewhat uniform strain field across the whole gauge length is achieved.
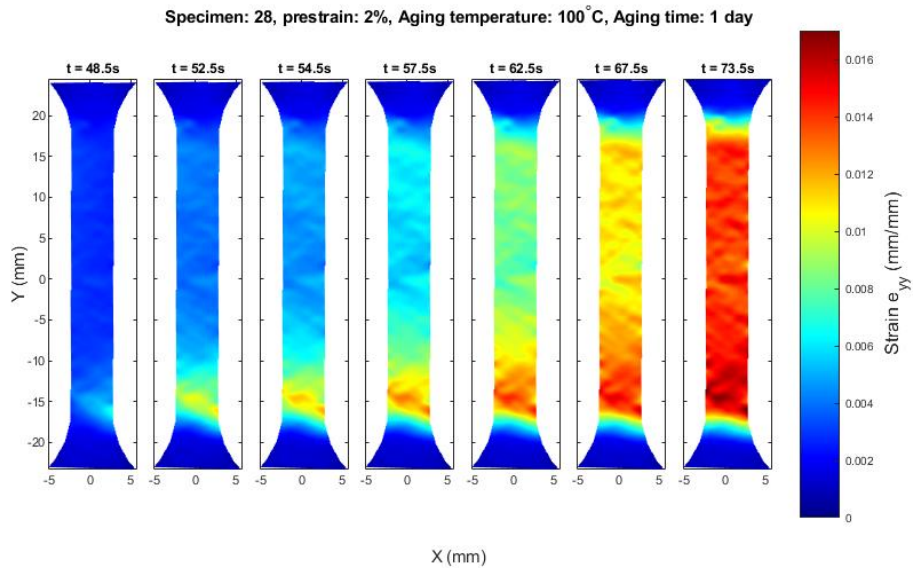
Figure 40 Full-strain measurements of specimen 28 after the yield point clearly showing the formation and propagation of diffuse Lüders band. The Lüders band nucleates from the bottom end of the gauge length and quickly propagates through the entire gauge length after which the uniform deformation in the strain hardening region across the whole gauge length starts.

56

Figure 41 shows the full-field strain measurements of specimen 29 after the yield point. The specimen 29 does not show typical Lüders band nucleating from gauge length end and propagating through the specimen in a front. There seems to be multiple Lüders bands nucleating along the gauge length immediately after the yield point. The most prominent band nucleates at the middle part of the specimen at the same location where the strains started to localize at the end of the pre-straining as shown in fig. 35. This is different from specimens 24 and 28 as they do not show clear localization of the stains in same locations as in the end of pre-straining. The Lüders bands in specimen 29 get stuck almost immediately as formation of other bands near the band front, or casting defects in the specimen prevent the band movement and further propagation. The strong correlation between the strain fields in pre-straining and final tensile testing indicates that there is defect at the location or that the dislocations that are formed during the pre-straining and locked during the aging are unpinned from the solute atoms allowing them to move again.
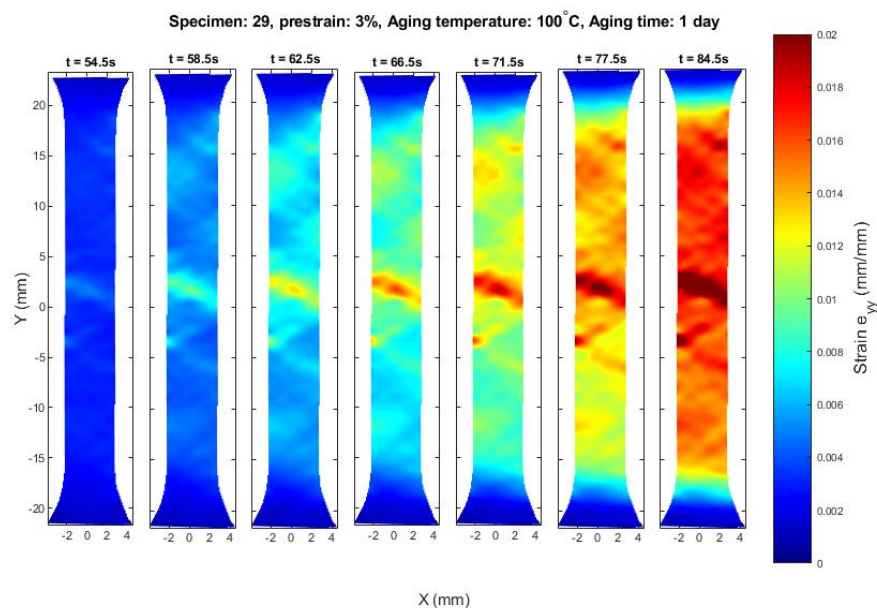
Figure 41 Full-field strain measurements of specimen 29 after yield point showing immediate localization of strain in the point where the specimen ultimately fractures. The Lüders bands still propagate through the whole specimen and the specimen deform uniformly despite the immediate strain localization.

Figure 42, Figure 43, Figure 46, Figure 47, Figure 50, Figure 51, Figure 54 and Figure 55 show the strain measurements of all the specimens along the Y-axis of the gauge length during the whole tensile test. The strain along Y-axis is the computed mean value of strains along the X-axis of the specimen. In Figure 42 the strains develop quite evenly distributed along the Y-axis until the strain localizes in the middle of the specimen where it finally ruptures. At the end of the tensile test there seem to be multiple smaller strain localizations across the gauge length. From Figure 43 it can be observed that the strain localization in the final fracture area starts already at around approximately 150 seconds. At this point there are other small strain localizations that develop similarly and the strain localization at the middle starts to grow more rapidly at approximately 225 seconds.
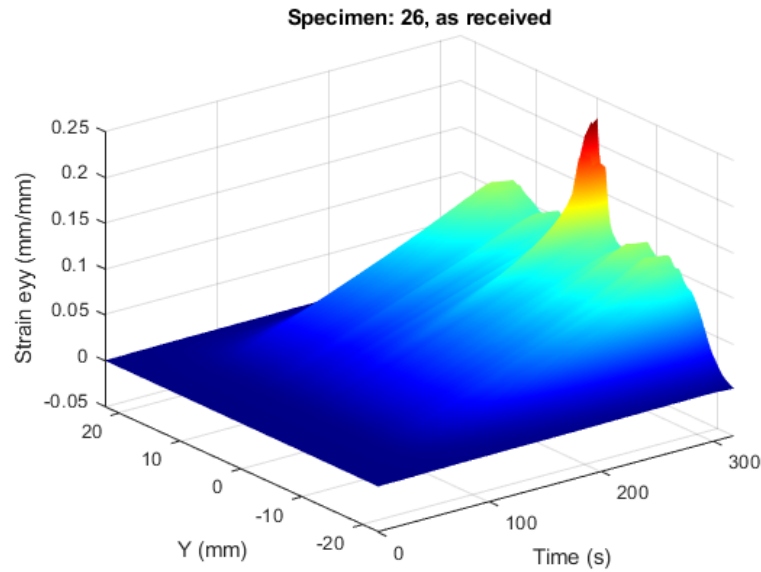
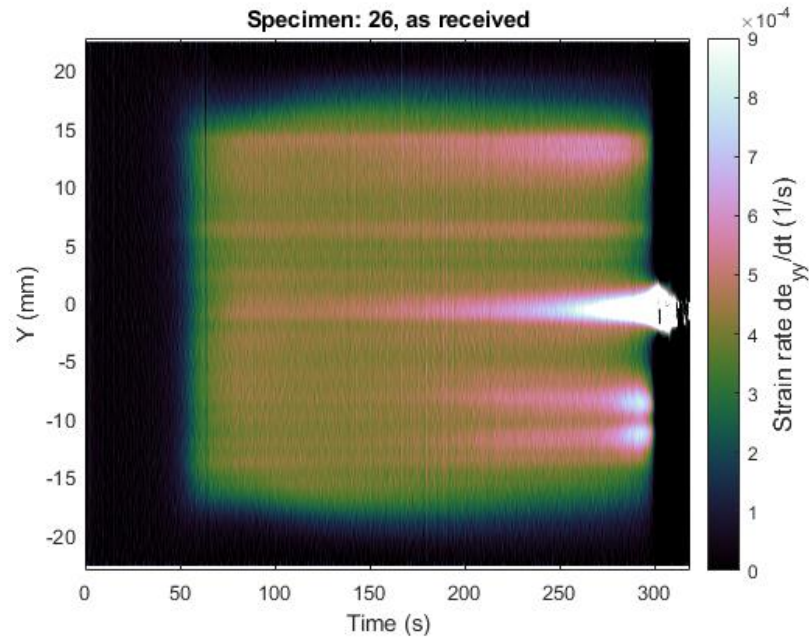**Figure 42 Strain measurement of the reference tensile test conducted for specimen 26 along the gauge length of the specimen. The strains at each position Y are the calculated mean strains along the X-axis (width) of the specimen. Y-axis of the figure indicates the position Y along the gauge length of the specimen. X-axis of the figure indicates the time during the tensile test.**
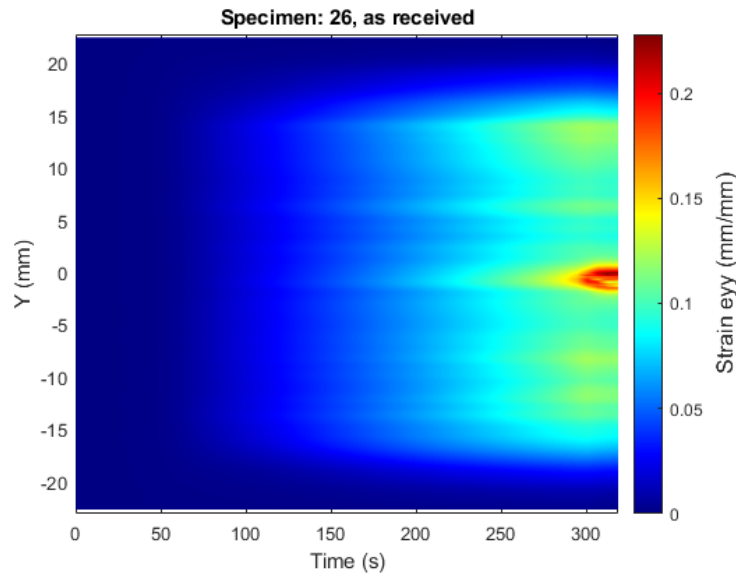
Figure 43 Strain measurement of the reference tensile test conducted for specimen 26 along the gauge length of the specimen. The strains at each position Y are the calculated mean strains along the X-axis (width) of the specimen. Y-axis of the figure indicates the position Y along the gauge length of the specimen. X-axis of the figure indicates the time during the tensile test.

Figure 44 shows the strain rates along the gauge length instead of accumulated strains during the tensile test. The figure clearly confirms that there are no Lüders bands forming and propagating trough the specimen as they should be seen as diagonal lines of higher strain rates in the figure.

58

Figure 44 Strain rate measurement of the reference tensile test conducted for specimen 26 along the gauge length of the specimen. The strain rate at each position Y is the calculated mean strain rate along the X-axis (width) of the specimen. Y-axis of the figure indicates the position Y along the gauge length of the specimen. X-axis of the figure indicates the time during the tensile test.

Figure 45 shows the full-field strain measurements at the end of the tensile test, visualizing the nucleation and propagation of the final fracture. The multiple smaller strain localizations are also clearly visible in the figure.
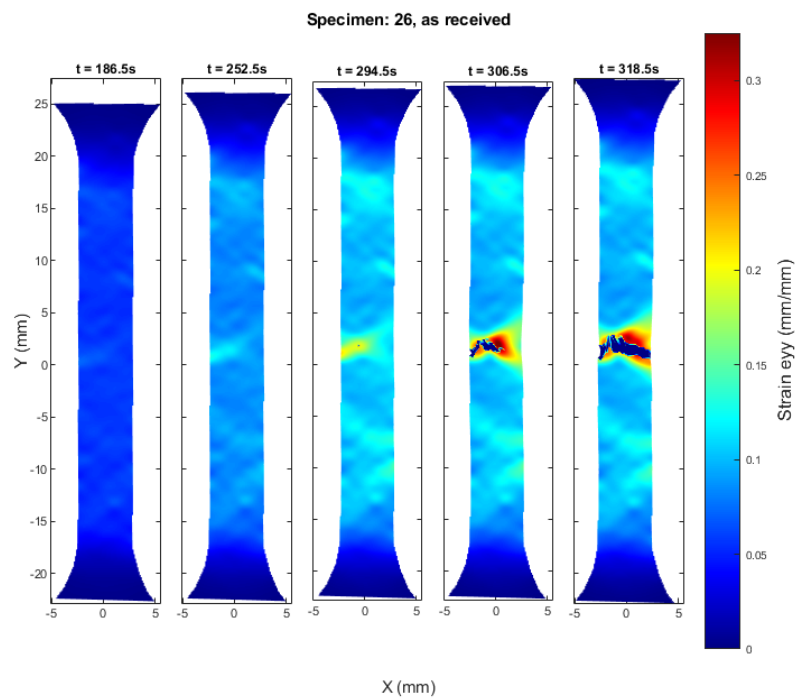
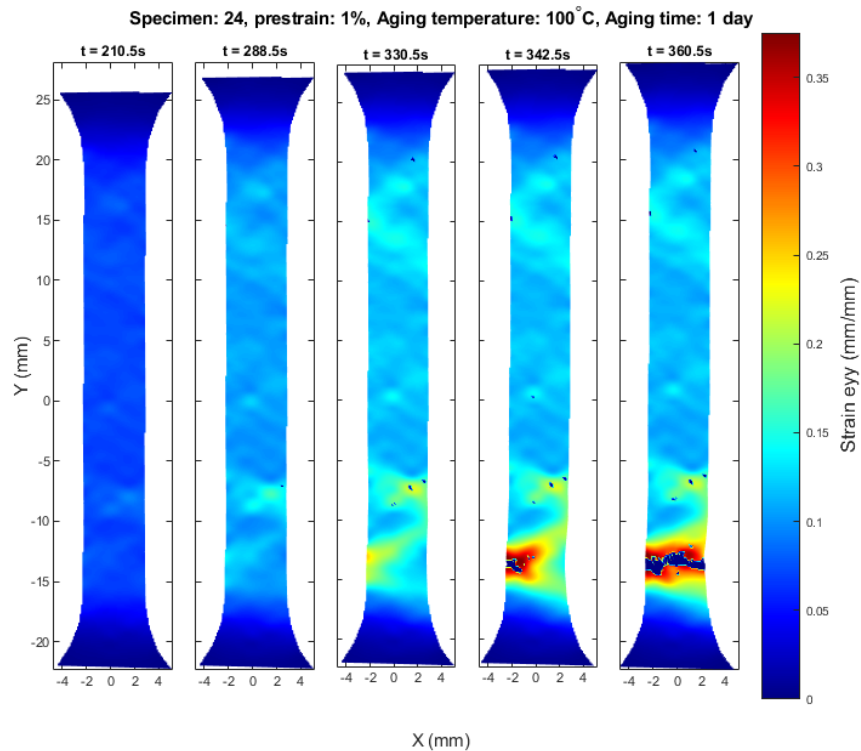**Figure 45 Full-field strain measurements of specimen 26 at the time t. Color indicates the level of strain in Y-diretion (e_{yy}).**

Figure 46 clearly shows the more localized nature of the yielding in specimen 24. Two big strain localizations can be seen during the tensile tests at the bottom end of the gauge length as in Figure 39. They are barely visible even after yield point but start to grow more rapidly at around 150 seconds as can be seen from Figure 47. The strain localizations seen in the upper half of the gauge length in Figure 39 are not very pronounced in this figure indicating that the bands nucleated at the yield point around that region propagated more evenly during the tensile test. However, the two major bands at the bottom end that are seen also in Figure 39 got locked in place very fast and the strain localizes further in these regions during the test.
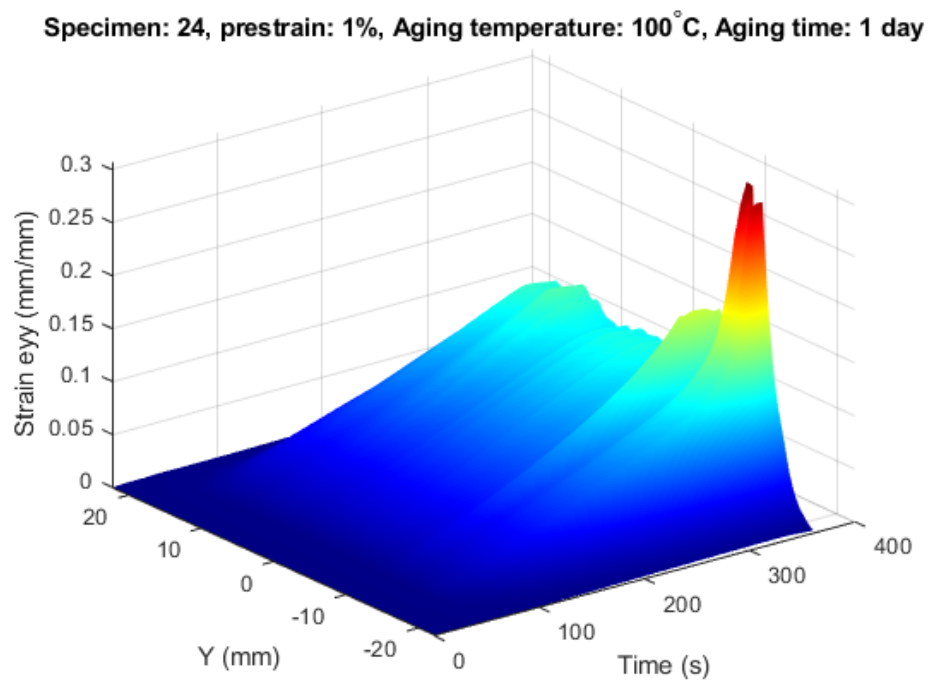
Figure 46 Strain measurement of specimen 24 along the gauge length of the specimen. The strains at each position Y are the calculated mean strains along the X-axis (width) of the specimen. Y-axis of the figure indicates the position Y along the gauge length of the specimen. X-axis of the figure indicates the time during the tensile test. Z-axis of the figure indicates the strain in Y direction.
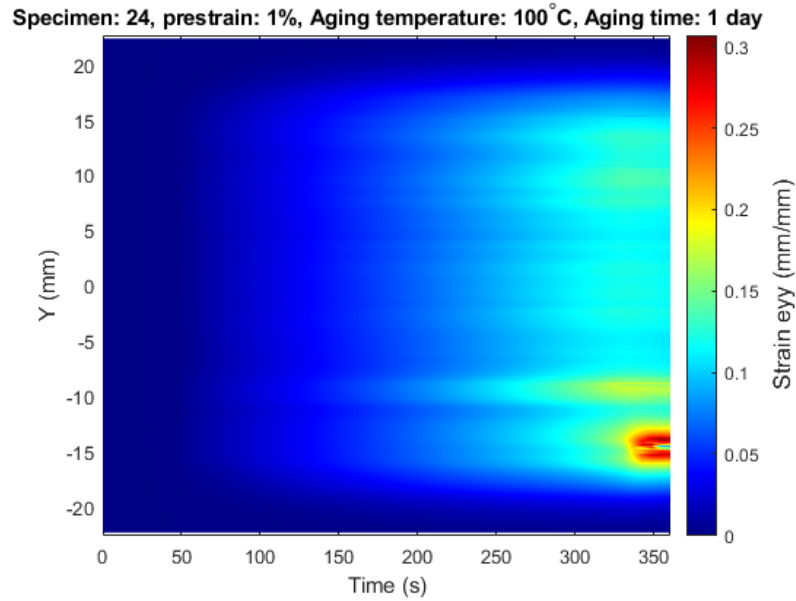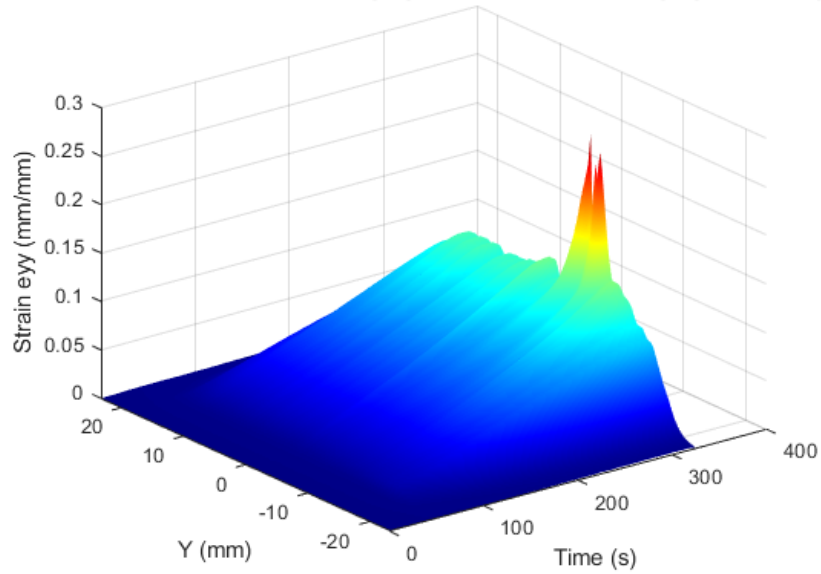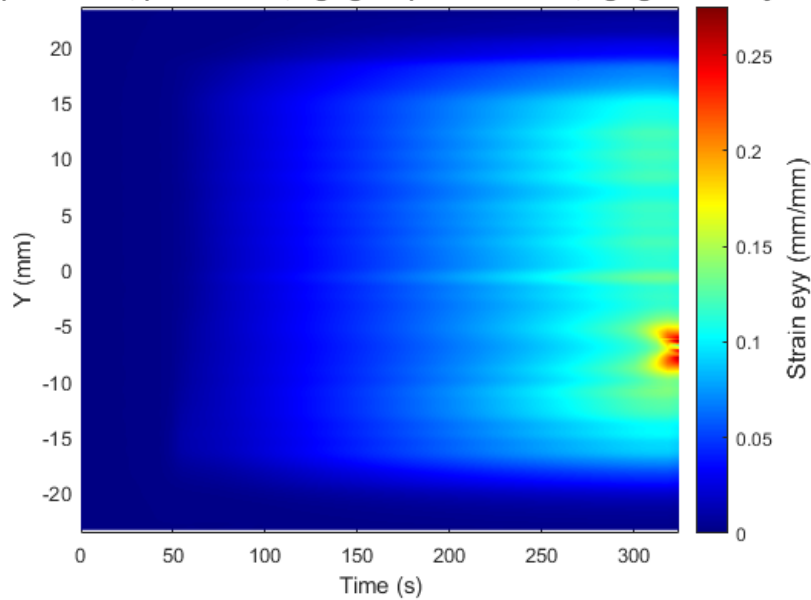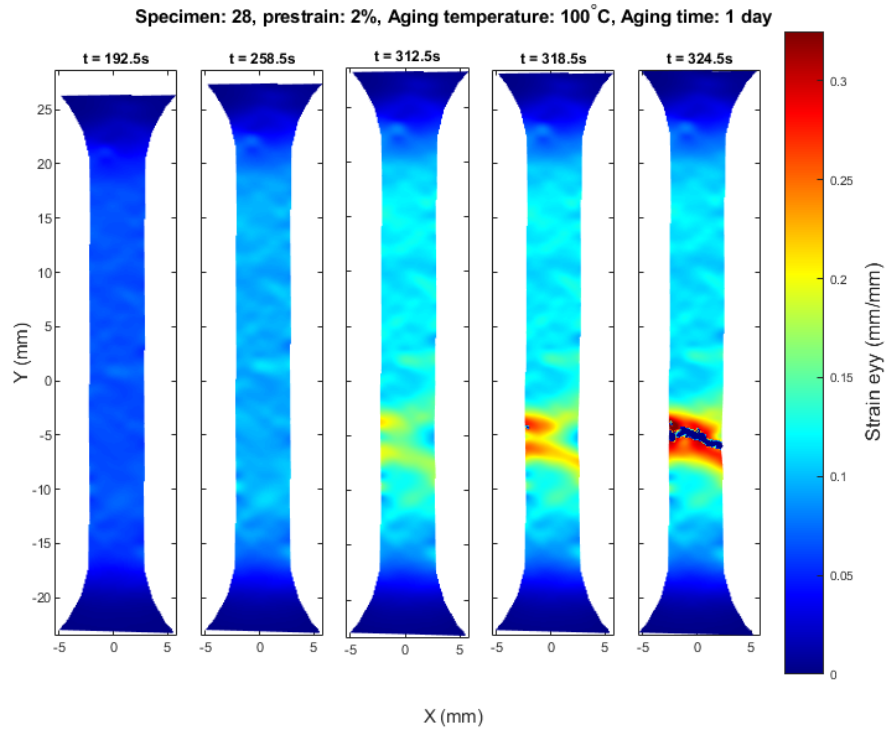
Figure 47 Strain measurement of specimen 24 during the tensile test. The strains at each position Y are the calculated mean strains along the X-axis (width) of the specimen. Y-axis of the figure indicates the position Y along the gauge length of the specimen. X-axis of the figure indicates the time during the tensile test. The strain in Y-direction (eyy) is indicated in color.

Figure 48 shows the strain rates along the gauge length during the tensile experiment. The figure confirms that most of the strain localizations do not propagate through the gauge length. There is one vague Lüders band that nucleates from the upper part of the specimen and propagates trough the gauge length until it gets stuck to Lüders band/strain localization at the bottom part of the gauge length.
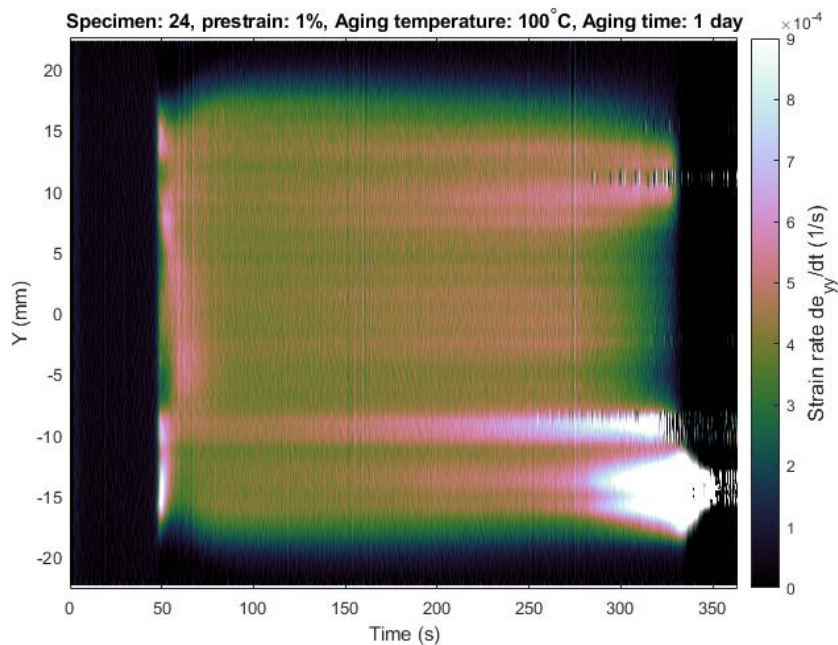
Figure 48 Strain rate measurements of specimen 24 during the tensile test. The strain rate at each position Y is the calculated mean strain rate along X-axis of the specimen.

61

Figure 49 shows how the final fracture propagates in specimen 24. It can be clearly seen that the crack nucleates at the site where one of the major Lüders bands first nucleated around the yield point and got stuck shortly after the nucleation.

Figure 49 Full field strain measurements of specimen 24 at the time t during the tensile test. Color indicates the level of strain in Y-diretion (eyy).

The yielding behavior in specimen 28 is much different during the tensile test from the specimen 24. From Figure 50 we can see that the yielding behavior is much more even across the whole gauge length. From Figure 51 it can be vaguely seen that the yielding starts from bottom end of the gauge length at the yield point and propagates towards the other end of the specimen as was observed in Figure 40. However, after the propagation the yielding is very uniform across the whole gauge length compared to specimen 24. From Figure 51 multiple small strain localizations can be observed after around 150 seconds but strangely the most prominent strain localizations are not the ones leading to the final fracture.

Specimen: 28, prestrain: 2%, Aging temperature: 100°C, Aging time: 1 day

Figure 50 Strain measurement of specimen 28 during the tensile test. The strains at each position Y are the calculated mean strains along the X-axis (width) of the specimen. Y-axis of the figure indicates the position Y along the gauge length of the specimen. X-axis of the figure indicates the time during the tensile test. Z-axis of the figure indicates the strain in Y-direction (eyy).

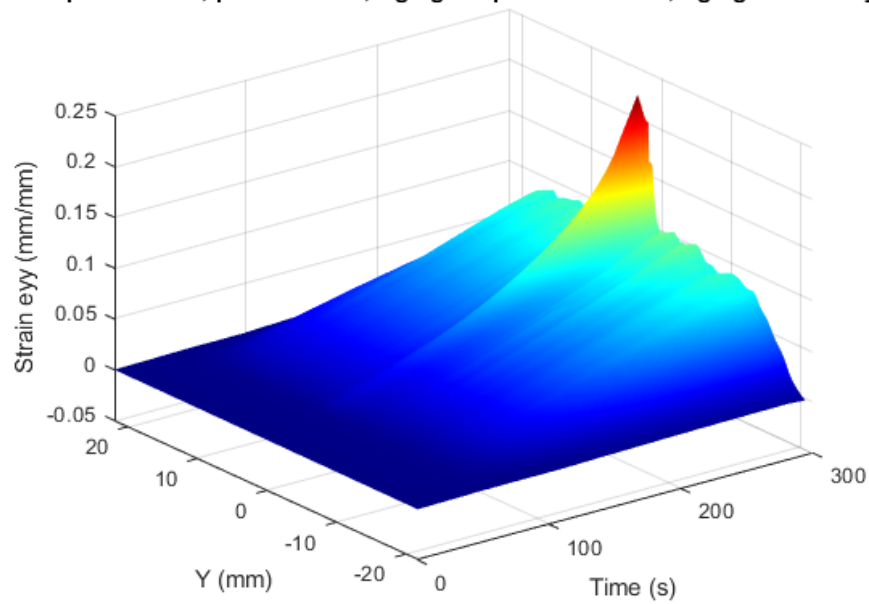Specimen: 28, prestrain: 2%, Aging temperature: 100°C, Aging time: 1 day

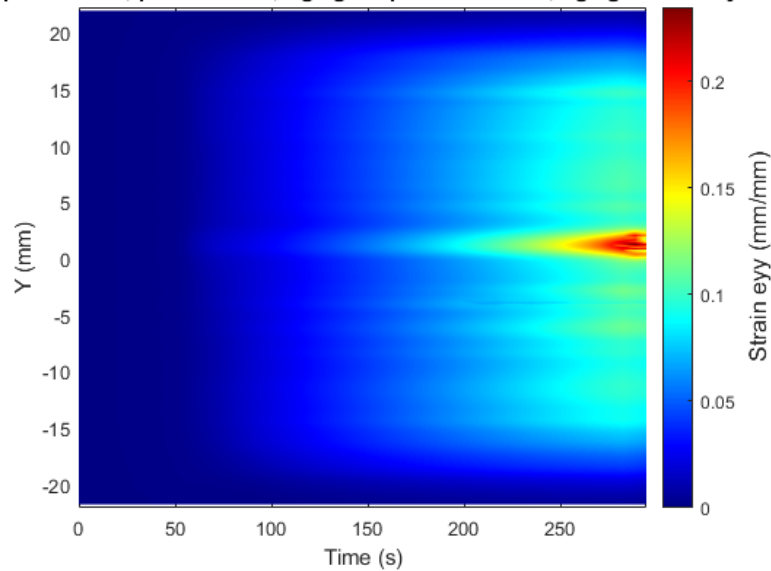**Figure 51 Strain measurement of specimen 28 during the tensile test. The strains at each position Y are the calculated mean strains along the X-axis (width) of the specimen. Y-axis of the figure indicates the position Y along the gauge length of the specimen. X-axis of the figure indicates the time during the tensile test. Color indicates the strain in Y-direction (eyy).**

63

The strain rate measurements during the tensile test in Figure 52 confirm that there is a quite pronounced Lüders band propagating from the bottom part of the gauge length that nucleates towards the other end and gets stuck before the middle point, which can be seen as diagonal line of pronounced strain rate. The figure also confirms that the strain in the upper part of the gauge length does not move as a clear Lüders band.
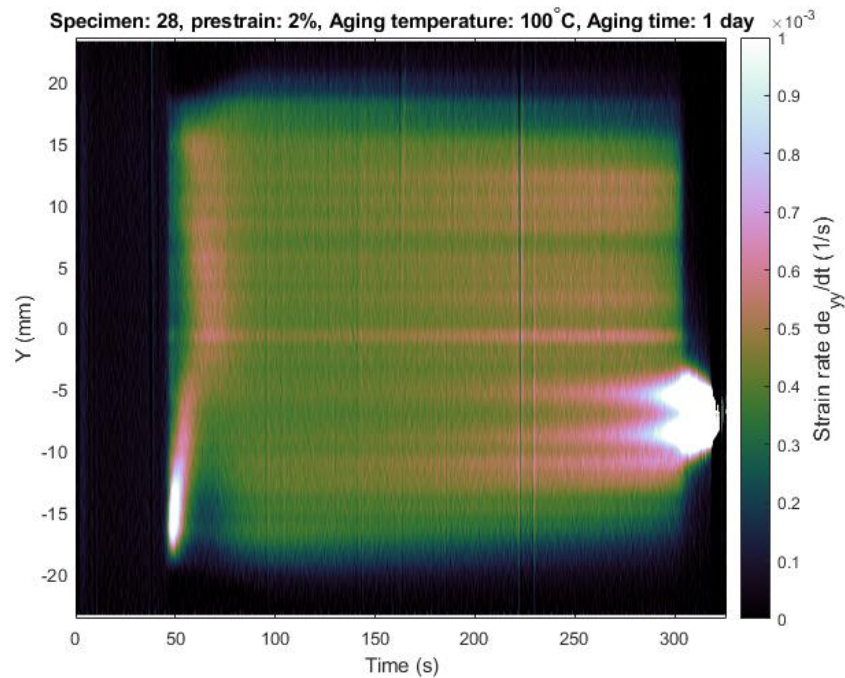
Figure 52 Strain rate measurements of specimen 28 during the tensile experiment. The strain rate at each position Y is the calculated mean strain rate along X-axis of the specimen.

Figure 53 shows how the final fracture nucleates and propagates in specimen 28. Unlike in the specimen 24 the specimen 28 seems to not fracture at location where the Lüders band first nucleated. However, the fracture seems to start around the area where the first Lüders band that nucleated from bottom end of the specimen got stuck (see Figure 40).

Figure 53 Full-field strain measurements of specimen 28 at the time t during the tensile test. Color indicates the level of strain in Y-diretion (e_yy).

The yielding behavior of specimen 29 during the tensile testing is shown in Figure 54. It can clearly be seen that the strain localizes at the position where the most prominent Lüders band first nucleated in Figure 41. The localized strain in the middle area of the gauge length is visible in the strain measurements during the whole tensile test. Figure 55 shows that the strain localization is clearly present during the whole tensile test, but the strain starts to localize faster after around 125 seconds. Despite the strong localization of strain in one place that is present throughout the whole tensile test, the rest of the specimen still yields quite evenly throughout the test. However, as seen in Figure 41, it takes longer for the uniform elongation to start than in specimens 24, 26 and 28 as the strain is still distributed quite unevenly at the time of 84.5 seconds. This is expected from the earlier tensile tests as the 3% pre-strained specimen show yield plateau to some extent unlike specimens that are pre-strained 1% or 2%.
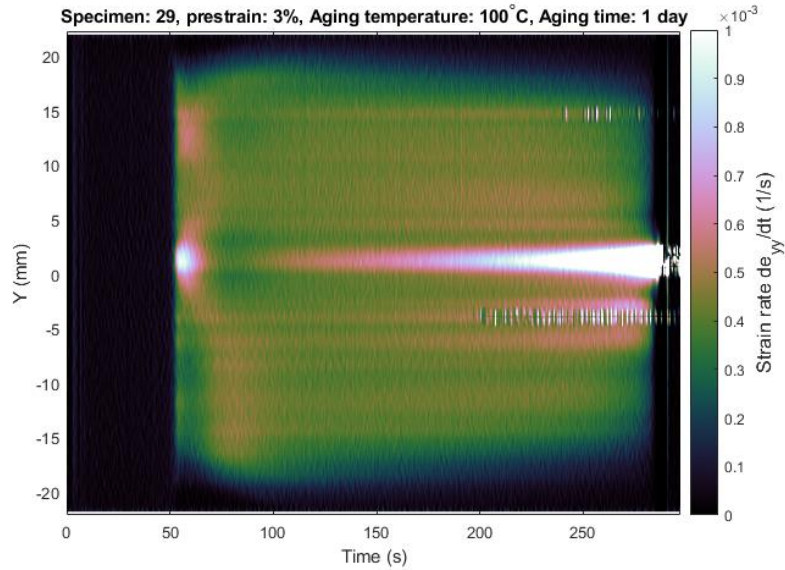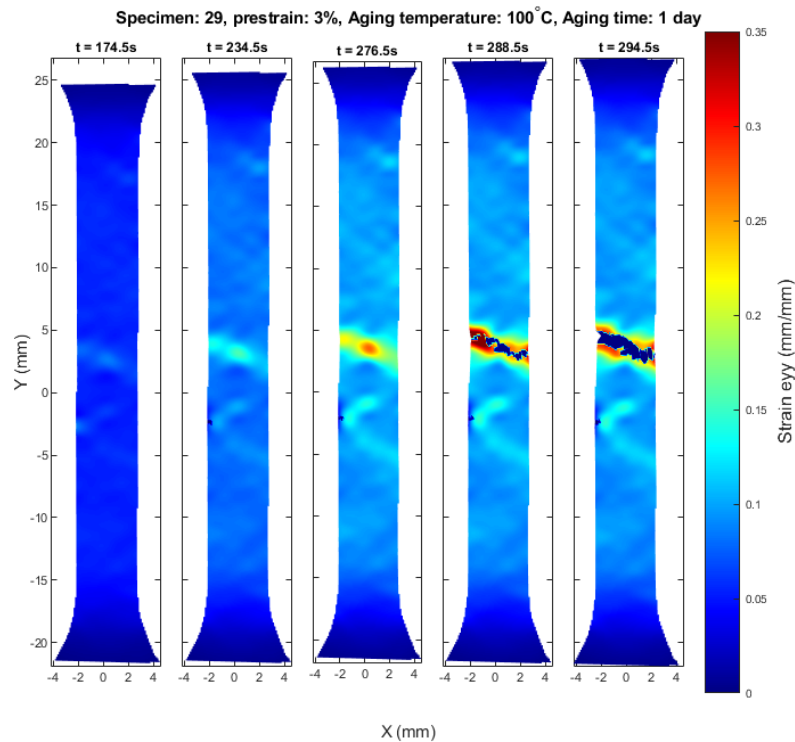
Figure 54 Strain measurement of specimen 29 during the tensile test. The strains at each position Y are the calculated mean strains along the X-axis (width) of the specimen. Y-axis of the figure indicates the position Y along the gauge length of the specimen. X-axis of the figure indicates the time during the tensile test. Z-axis of the figure indicates the strain in Y-direction (eyy).

Figure 55 Strain measurement of specimen 29 during the tensile test. The strains at each position Y are the calculated mean strains along the X-axis (width) of the specimen. Y-axis of the figure indicates the position Y along the gauge length of the specimen. X-axis of the figure indicates the time during the tensile test. Color indicates the strain in Y-direction (eyy).

Figure 56 shows the strain rate measurements of specimen 29 during the tensile test. The strain rate measurements clearly confirm that there are no clear Lüders bands that propagate trough the gauge length in specimen 29.

Figure 56 Strain rate measurements of specimen 28 during the tensile experiment. The strain rate at each position Y is the calculated mean strain rate along X-axis of the specimen. There are no clear diagonal lines of increased strain rate which indicate the absence typical Lüders bands that propagate trough the gauge length as front.

Figure 57 shows the strain measurements at the end of the tensile test in specimen 29. The crack nucleates in the site where the most prominent Lüders band nucleated at the start of yielding. The other Lüders bands in the vicinity of the most prominent one can also be seen as smaller strain localizations at the time of fracture.

Figure 57 Full-field strain measurements of specimen 29 at the time t during the tensile test. Color indicates the level of strain in Y-diretion (e_{yy}).

4.3 Microstructure

A sample from specimens 1 and 11 was prepared for microstructural analysis. The specimens 1 and 11 are from the opposing extremes of the block from which the specimens were manufactured regarding radial distance of the specimen from the middle of the cast. The distance between the specimens in the cast is about 33 mm. The microstructure of the specimen 1 can be seen from Figure 58. The microstructure is well in line with previous examinations from literature [12] and fulfills the requirement of graphite nodules being at least 80% of forms V and VI according to standard EN ISO 945. However, a more general look at the microstructure with lower magnification reveals the very inhomogeneous nature of the material with the graphite nodule density and size varying remarkably within one small sample. The inhomogeneous microstructure can be seen from Figure 59. Specimen 11 seems to have notably bigger nodule size than specimen 1 and has also clearly more homogeneous graphite nodule distribution and size. Specimen 11 microstructure can be seen from Figure 60 and Figure 61. It should be noted that specimen 1 is unaged specimen and specimen 11 is aged in 300 ℃ for 1 day. The more homogeneous graphite nodule distribution and larger graphite nodule size might be partly due to the diffusion of graphite during the aging process. However, the temperature of 300 ℃ is still relatively low when considering the microstructure and is expected to have very small effect on the graphite nodule distribution and size.
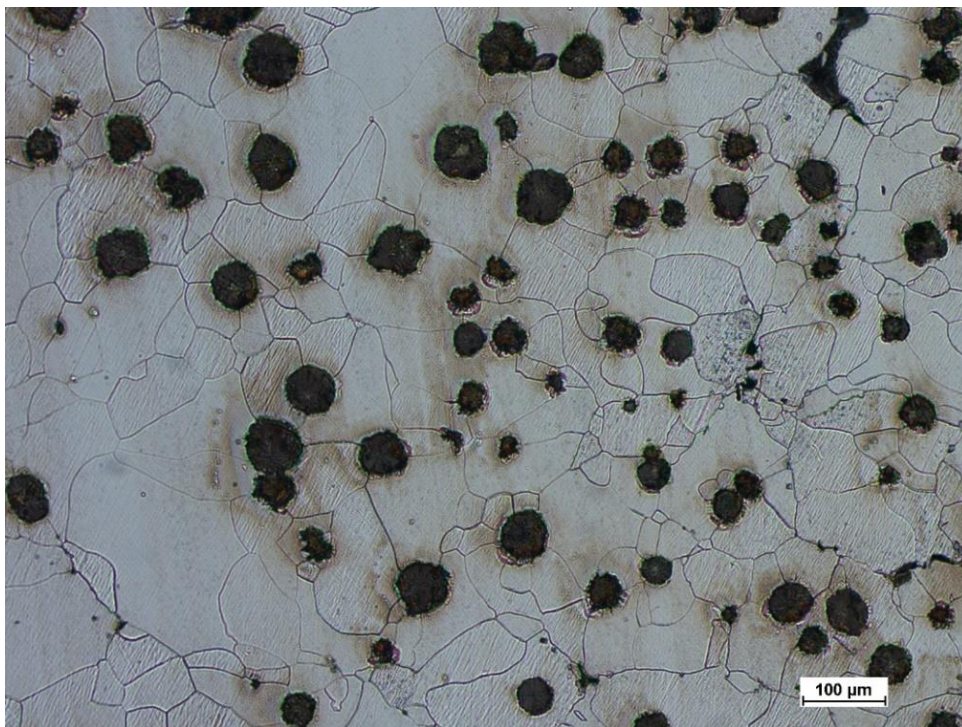
Figure 58 Micrograph from specimen 1 showing typical microstructure for the cast iron insert.
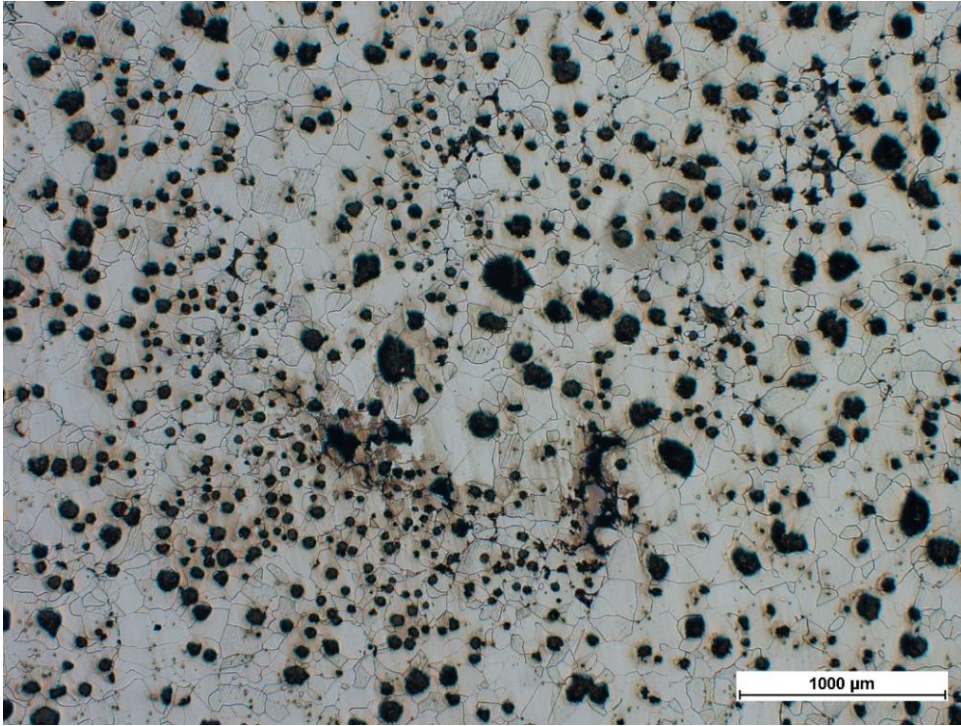
Figure 59 Micrograph from specimen 1 showing the inhomogeneous nature of the material.
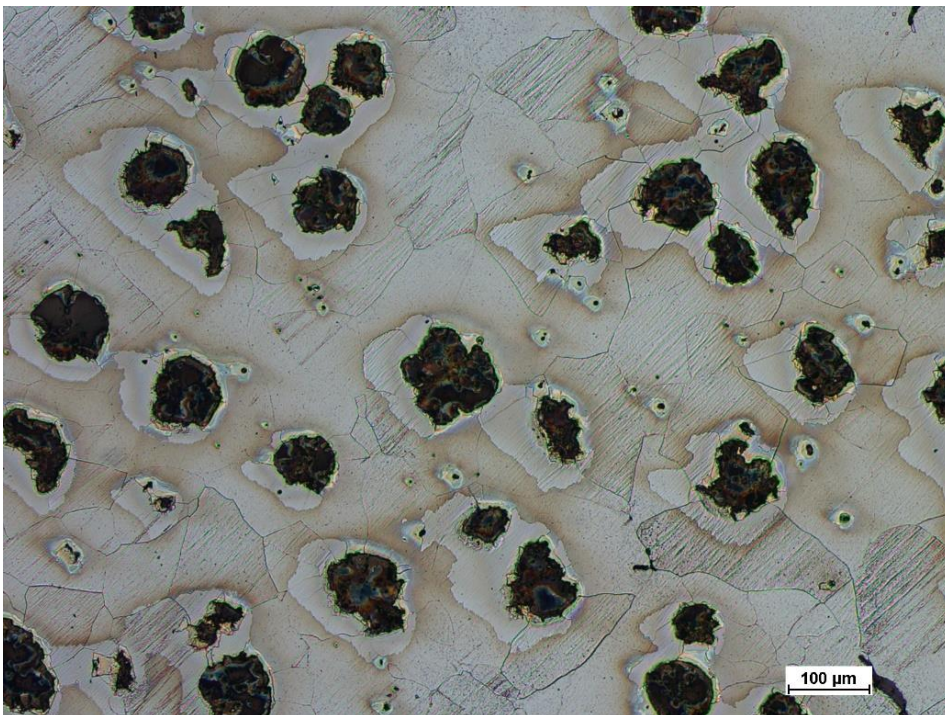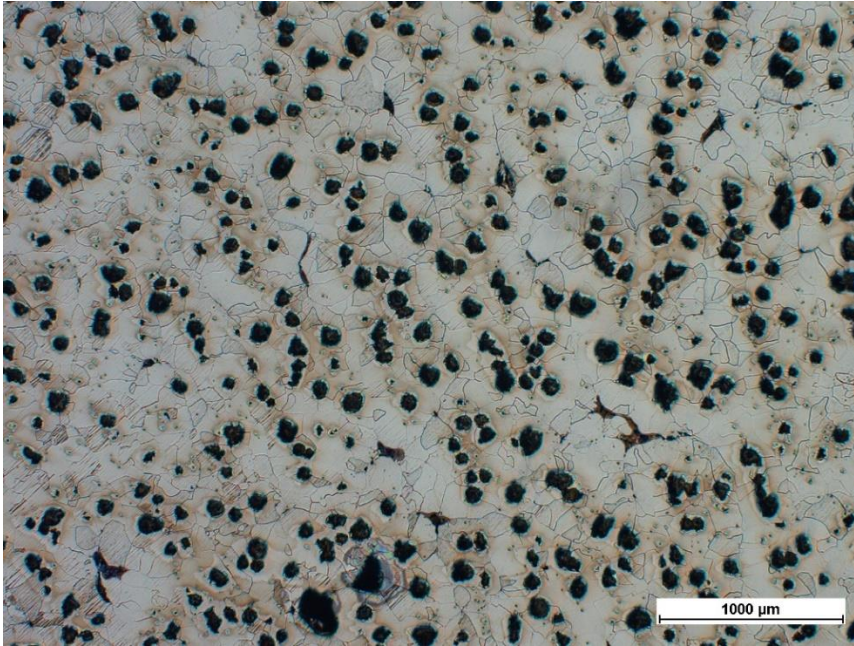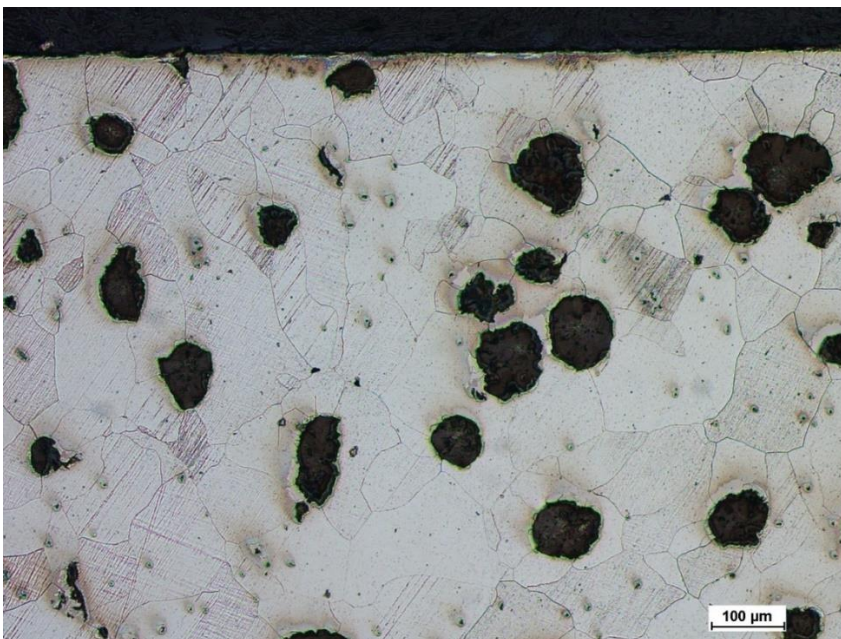

Figure 60 Micrograph from specimen 11.

Figure 61 Micrograph from specimen 11. The microstructure and graphite nodule distribution is more homogenous than in specimen 1. Note the amount of porosity in the material.

To exclude the possible effect of aging on the microstructure and to confirm the results, additional samples for microscopic examination were prepared from the as-received material. The microstructure was studied through the whole depth of the cast where the specimens were cut from to identify the possible scatter in the microstructure between specimens. Figure 62 and Figure 63 show microstructures close to the surface of the cast representing the part of the cast where the outer specimens (specimens 11, 22, 33) are cut from. From Figure 62 and Figure 63 we can see that the microstructure closely resembles the microstructure from the end of specimen 11 as expected which confirms that the aging temperature should have no effect on the microstructure.

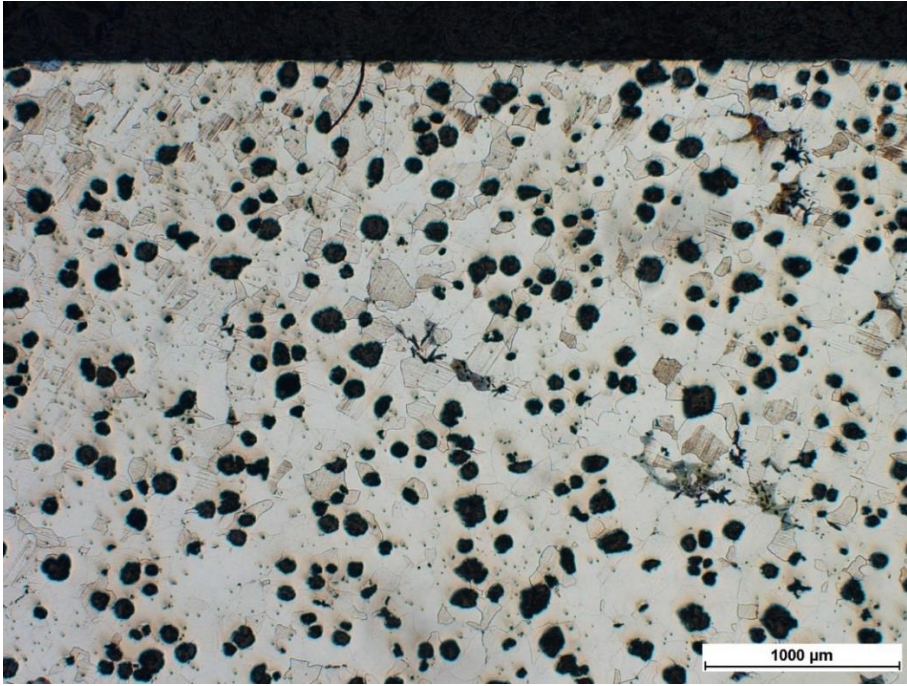**Figure 62 Micrograph close to the surface of the cast with 100x magnification.**

Figure 63 Micrograph from close to the surface of the cast with 25x magnification.

Figure 64 and Figure 65 show microstructure which correspond to the specimens that are cut furthest away from the surface (specimens 1, 12, 23). The microstructure in Figure 64 is very similar to the microstructure from the specimen 1 seen in Figure 58 as expected. However, the lower magnification image in Figure 65 looks more homogeneous than the microstructure in Figure 59 regarding the size and distribution of the graphite nodules. This confirms that there is natural scatter in the material.
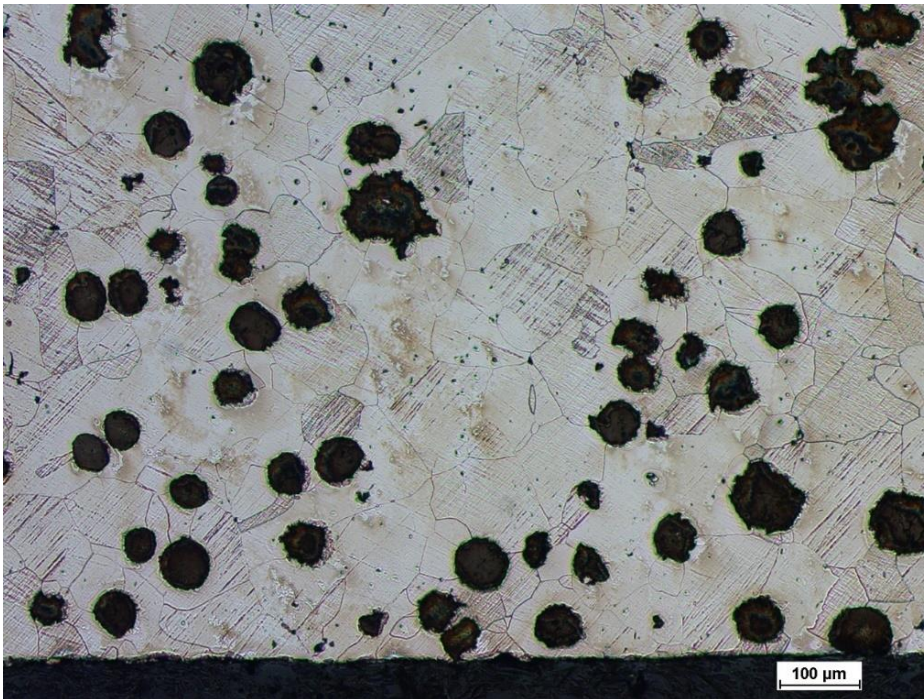
Figure 64 Micrograph from part of the cast corresponding to the specimens cut furthest from the surface with 100x magnification.
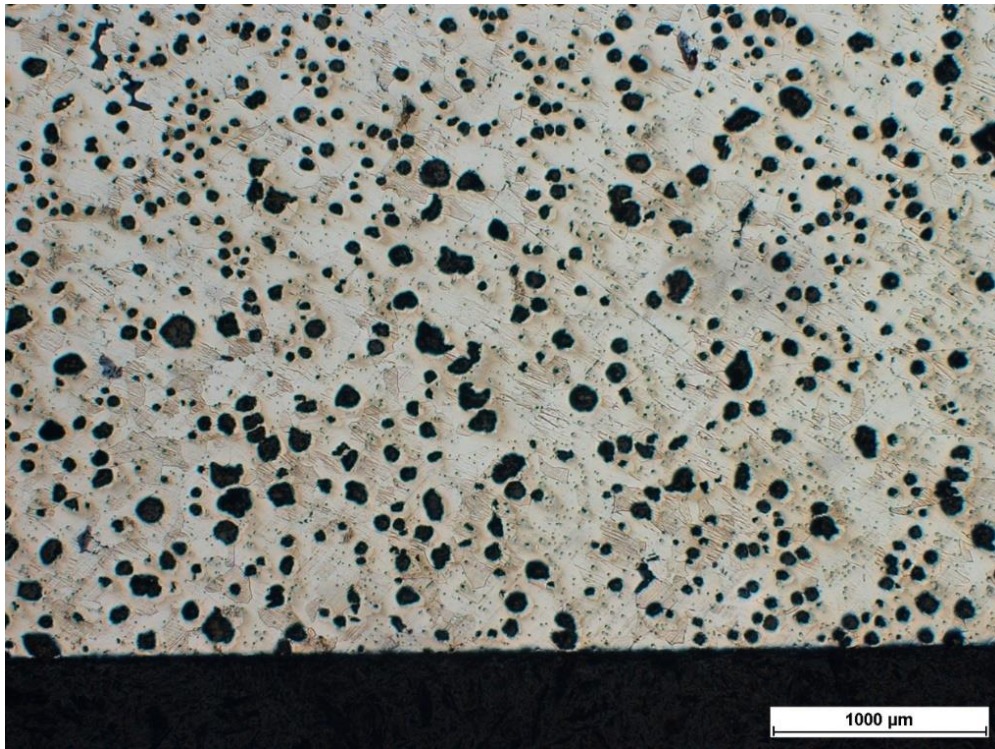
Figure 65 Micrograph from part of the cast corresponding to the specimens cut furthest from the surface with 25x magnifications.

4.4 Casting defects and crack initiation

In some specimens the low pre-strain values were already enough to detect some small localization of deformation and in some specimens even visible cracking initiated during the pre-straining. There was also visible pores or cavities in several specimen surfaces after the specimens were ground. In specimen 18 visible crack was observed before the final tensile test. A macro photograph of the crack can be seen in Figure 66. In specimen 22 there were some pores or cavities visible in the surface of the specimen and some visible deformation could be observed as seen in Figure 67. Specimens 11 and 21 also had some visible pores. Example of visible pores in specimen 11 can be seen in Figure 68. The differences in the colors of the specimens are due to the different temperatures they were aged at. Specimen 18 was aged at 200 ℃ while specimen 22 was aged at 400 ℃. The specimen 11 was not yet pre-strained nor aged when taking the picture.
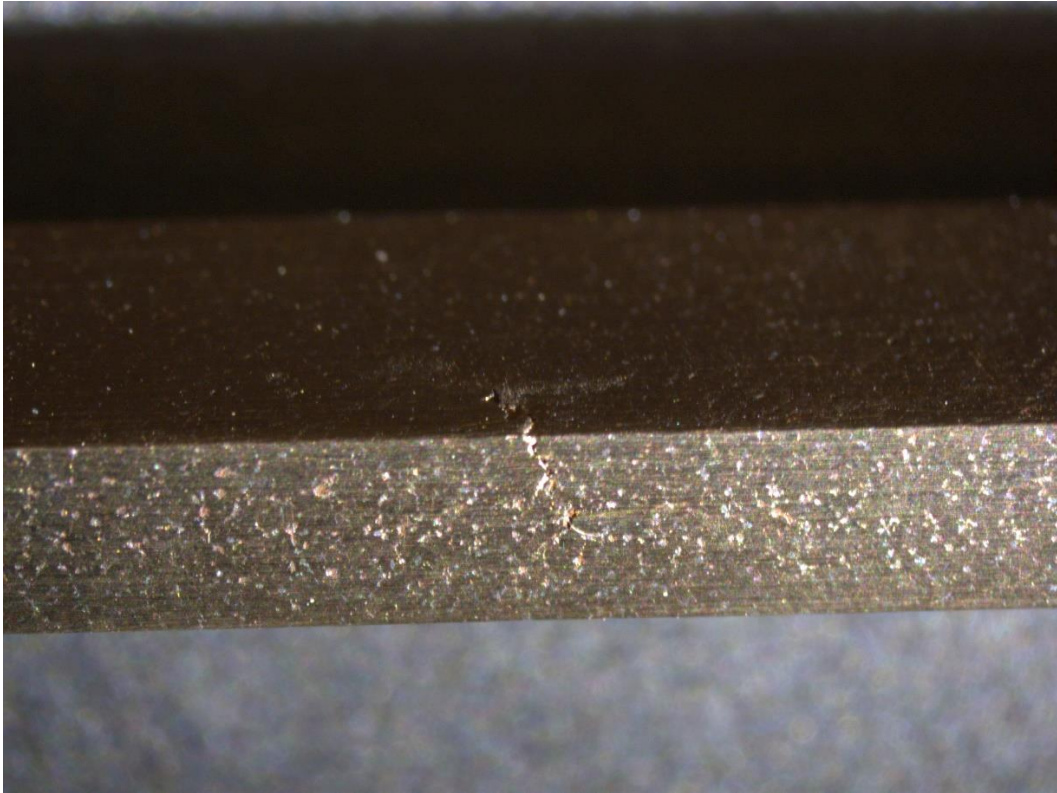
Figure 66 Visible crack on the surface of the specimen 18 after the 3 % pre-straining.
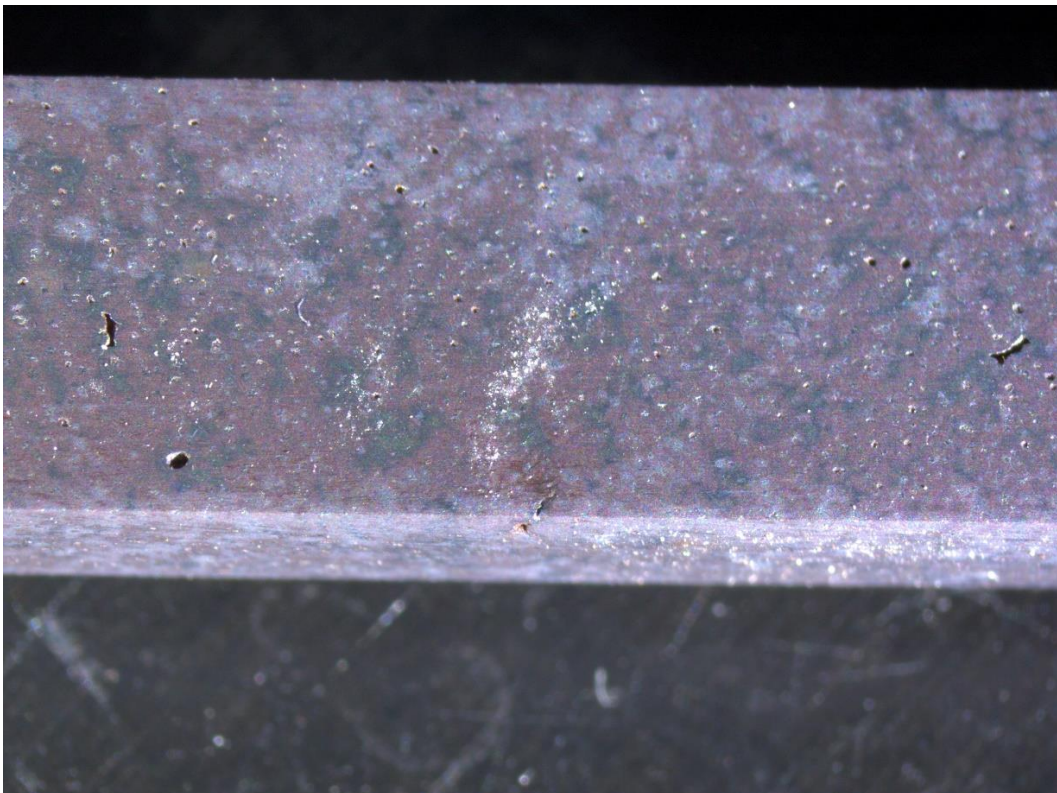
Figure 67 Visible deformation and pores on the surface of specimen 22 after 3 % pre-straining.
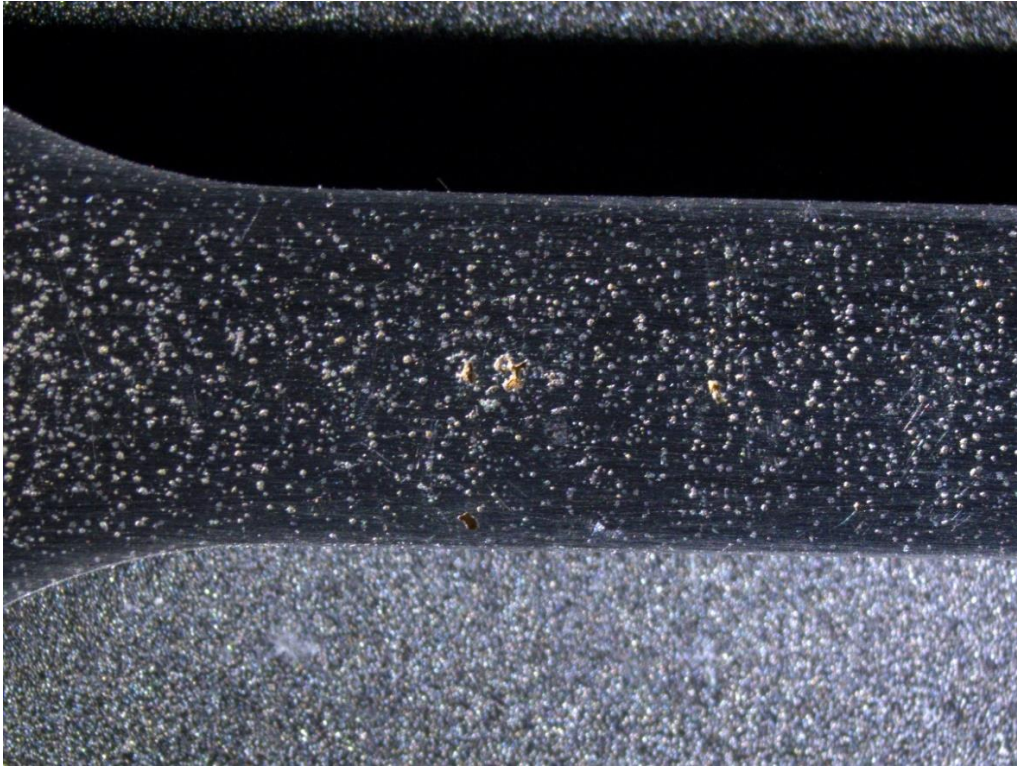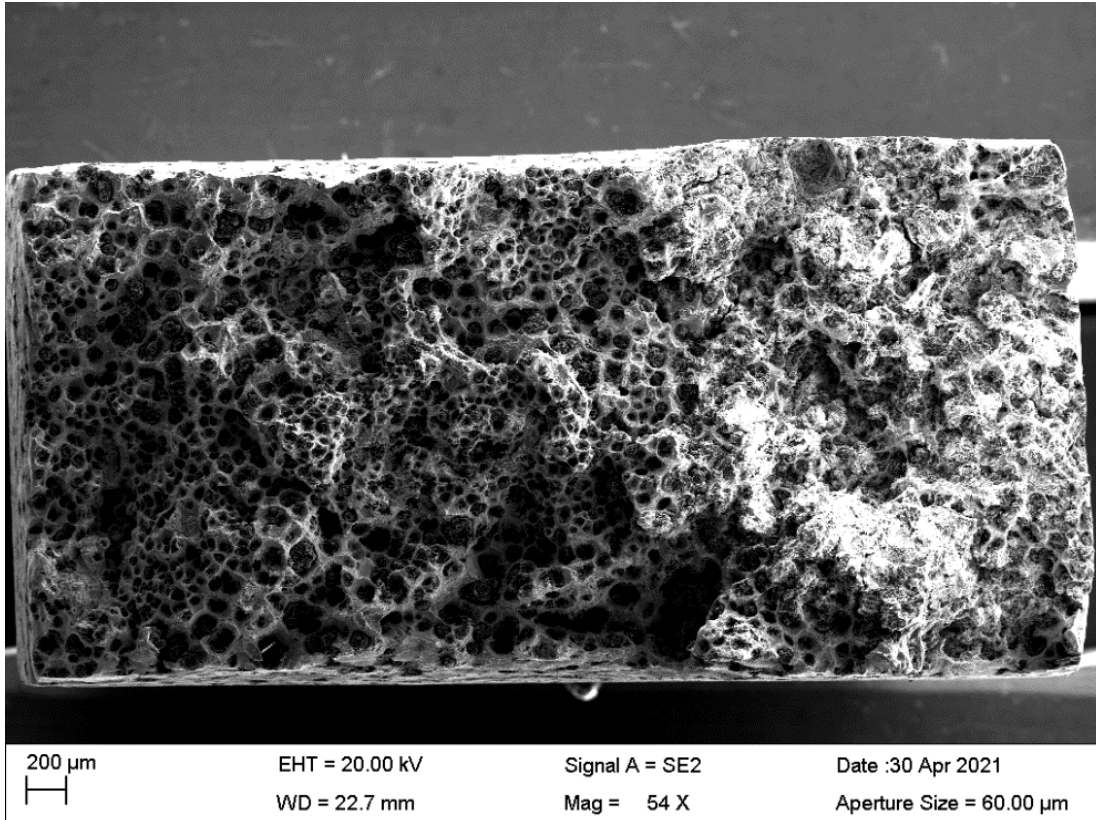
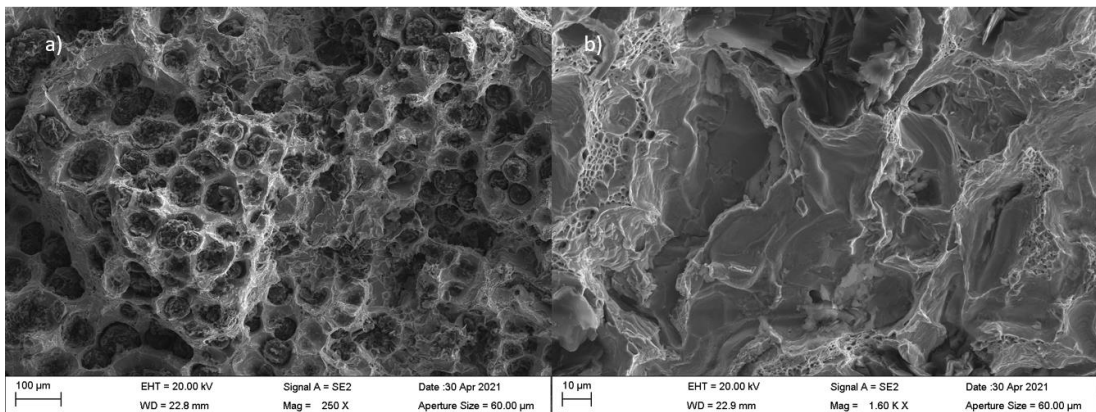**Figure 68 Visible pores and cavities at the surface of specimen 11 prior to any pre-straining.**

4.5 Break before yielding

The tensile specimen 5 which was subjected to 1% pre-strain and was aged in 100 ℃ temperature for 11 days showed very brittle behavior in the tensile test contradictory to the other tensile specimens. The stress dropped fast after the yield point without any strain hardening and the percentage elongation at maximum force was only 0.24 % (not including the pre-strain). This suggests the presence of major casting defect in the specimen as the transition of fracture mechanism from ductile to brittle is unlikely based on the other specimens. To verify the reason for the brittle behavior the fracture surface of the specimen 5 was inspected with scanning electron microscope (SEM). The general view of fracture surface of specimen 5 is presented in Figure 69. Figure 69 shows that there is more typical fracture surface at the left side and some unusual features in the right-side indicating presence of slag and defects in the cast.

| 200 μm | EHT = 20.00 kV | Signal A = SE2 | Date :30 Apr 2021 |
| | WD = 22.7 mm | Mag = 54 X | Aperture Size = 60.00 μm |

Figure 69 Fracture surface of specimen 5 showing typical ductile fracture in the left. Right side shows some unusual features indicating impurities and defects in the cast.

Figure 70 shows the fracture surface more closely from the left side of the surface shown in Figure 69. Figure 70 clearly confirms that the fracture mechanism is fully ductile a s there is clear cavities around the graphite nodules and dimple pattern in the ferritic matrix.

| 100 μm | EHT = 20.00 kV | Signal A = SE2 | Date :30 Apr 2021 | | 10 μm | EHT = 20.00 kV | Signal A = SE2 | Date :30 Apr 2021 |
| | WD = 22.8 mm | Mag = 250 X | Aperture Size = 60.00 μm | | | WD = 22.9 mm | Mag = 1.60 K X | Aperture Size = 60.00 μm |

Figure 70 Fracture surface of specimen 5. a) general view showing cavities around graphite nodules and b) showing dimple pattern in the ferritic matrix

Figure 71 shows closer view of the unusual parts of the fracture surface. There is clearly some indication and features pointing towards ductile fracture but also areas that are clearly

not fracture surface at all. This indicates that there is slag and some pores in this area of the cast.
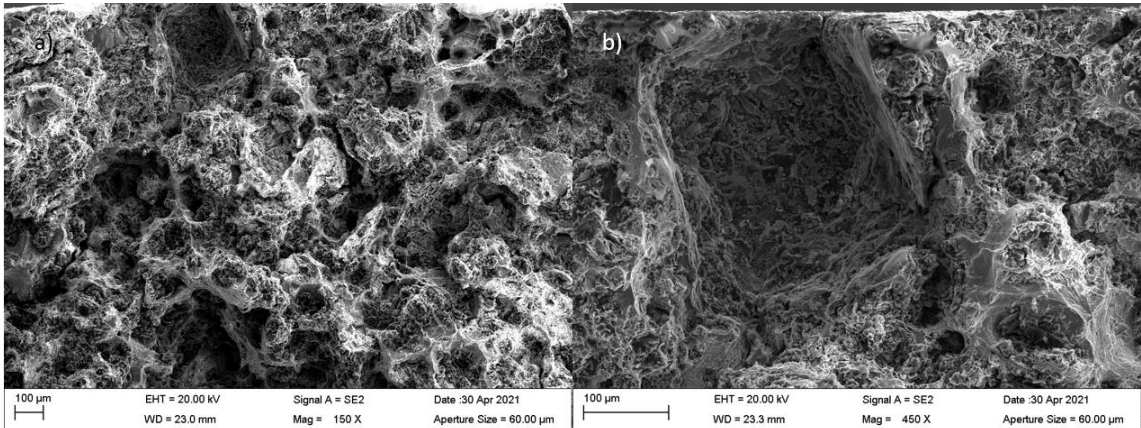
Figure 71 Fracture surface of specimen 5 at defect site. a) General view showing some signs of ductile fracture while having very uncommon surface indicating presence of impurities in the cast. b) Closeup showing surface that is clearly not fracture surface and indicates cavity or pore in this site as well as some slag.

Figure 72 shows even higher magnification images from the unusual parts of the surface clearly confirming that there are impurities in the cast. Figure 73 shows EDS analysis from the same area showing that there is magnesium, calcium, and sulfur present.
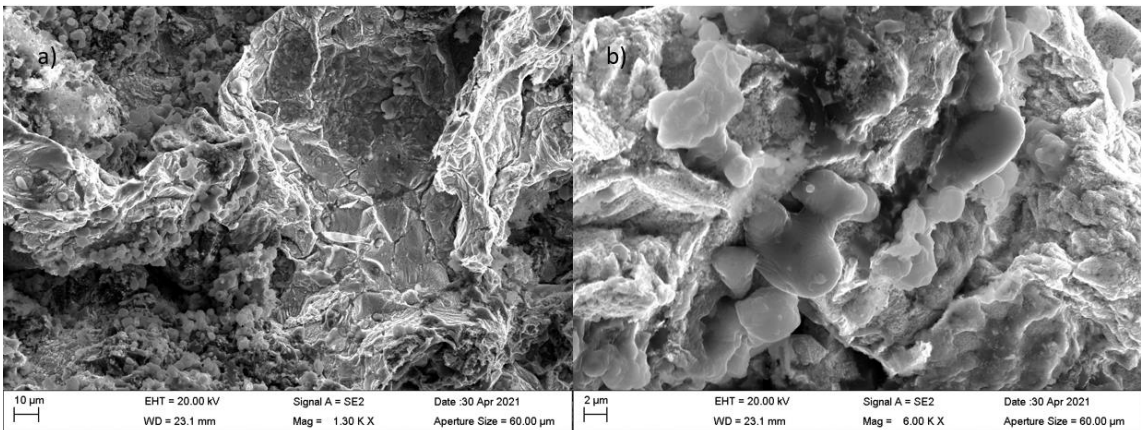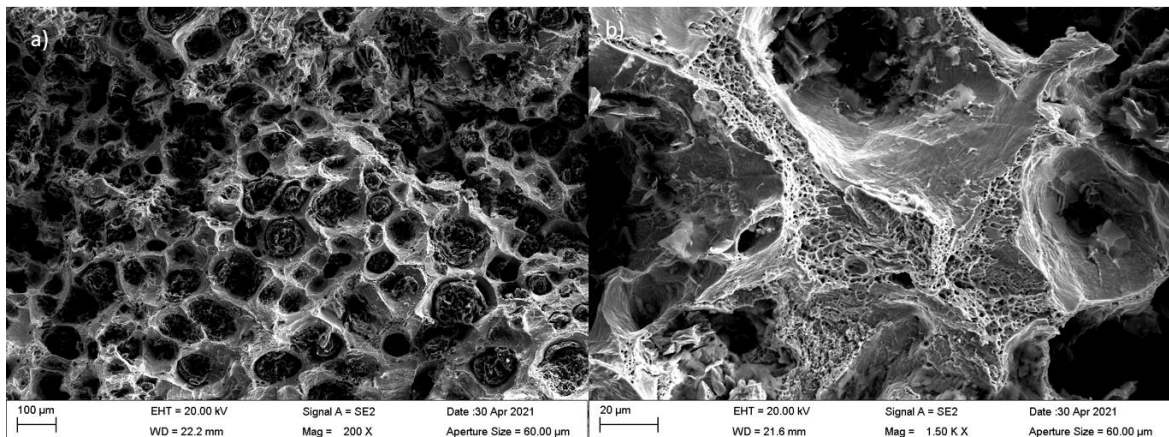

Figure 72 Specimen 5 fracture surface. a) General view showing unusual features (casting defects) and impurities b) showing closeup of the same location.
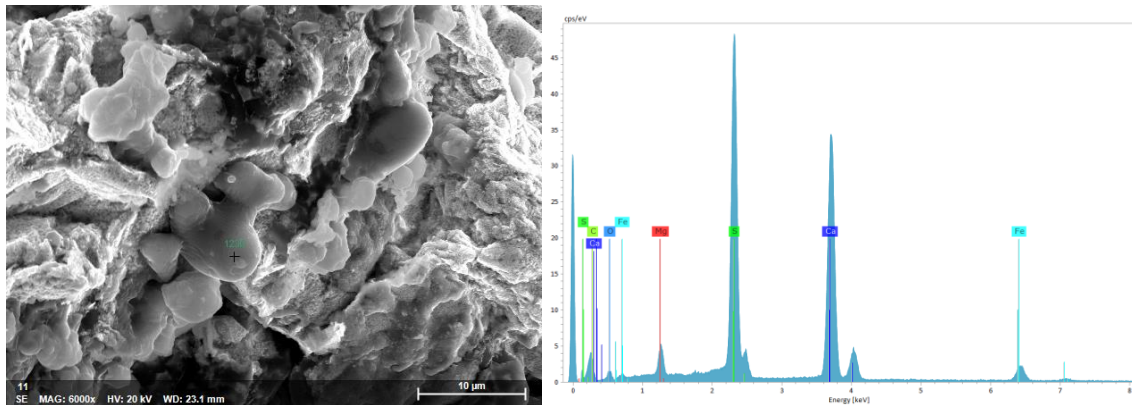
Figure 73 EDS analysis of impurities from specimen 5 fracture surface indicating presence of Mg, Ca and S.

Few other specimens in addition to specimen 5 were also studied with SEM to identify if the strain aging has some effect on the fracture mechanism and to identify reason for different yielding behaviors. The studied specimens were specimen 1 specimen 22 and specimen 29. Specimen 1 is the as received material, specimen 22 was pre-strained for 3% and aged at 400 °C for 1 day and showed low uniform elongation of 3.8 %. Specimen 29 is the 3% pre-strained specimen aged in 100 °C for 1 day that was studied with DIC and showed fast localization of strains at the onset of yielding.
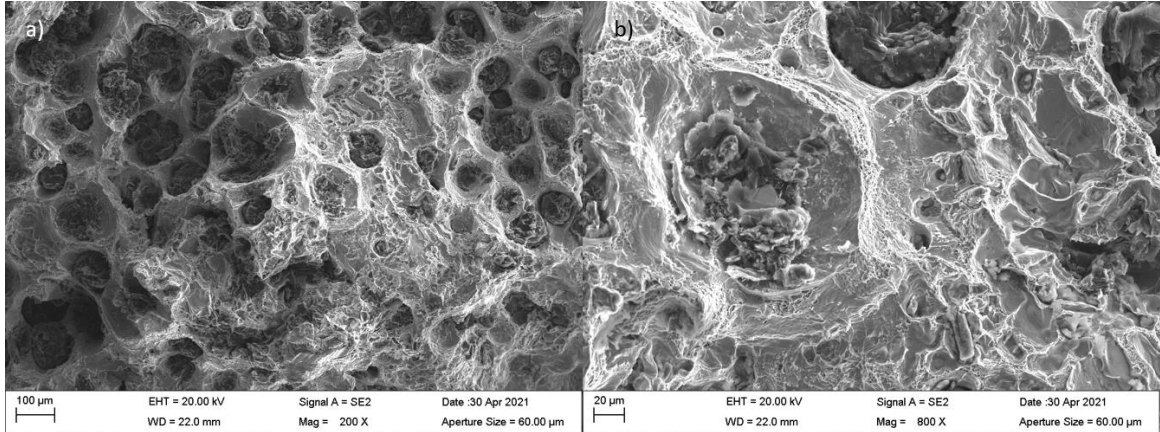
Figure 74 shows the fracture surface of the specimen 1. The fracture surface show large cavities in the ferritic matrix around the graphite nodules as well as dimple pattern in the ferritic ligaments which are typical for fully ductile fracture. The specimen fracture surface is homogeneous not showing presence of any major defects or impurities.
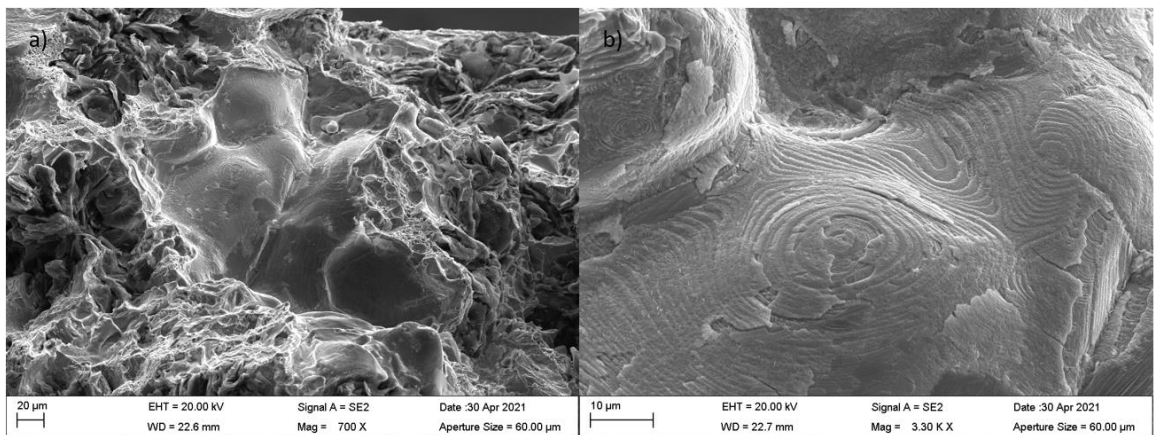

Figure 74 Fracture surface of specimen 1. a) General view of the fracture surface showing large cavities around the graphite nodules. b) Closeup from another part of the fracture surface showing small dimples in the ferritic ligament

Figure 75 shows the fracture surface of the specimen 22 from area that represents majority of the fracture surface. Like in specimen 1 there are clear cavities around the graphite nodules as well as dimple pattern in the ferrite. The fracture mechanism is fully ductile. However, the fracture surface of 22 is not as homogeneous as the fracture surface of the specimens 1 which indicates presence of some impurities in the cast. Figure 76 shows the fracture surface of specimen 22 in location where there is clear defect in the cast. The closeup shows very

smooth surface that is clearly not part of the actual fracture surface and indicates a presence of cavity or pore in this region. The presence of casting defects and impurities explain the lower elongation in this specimen.
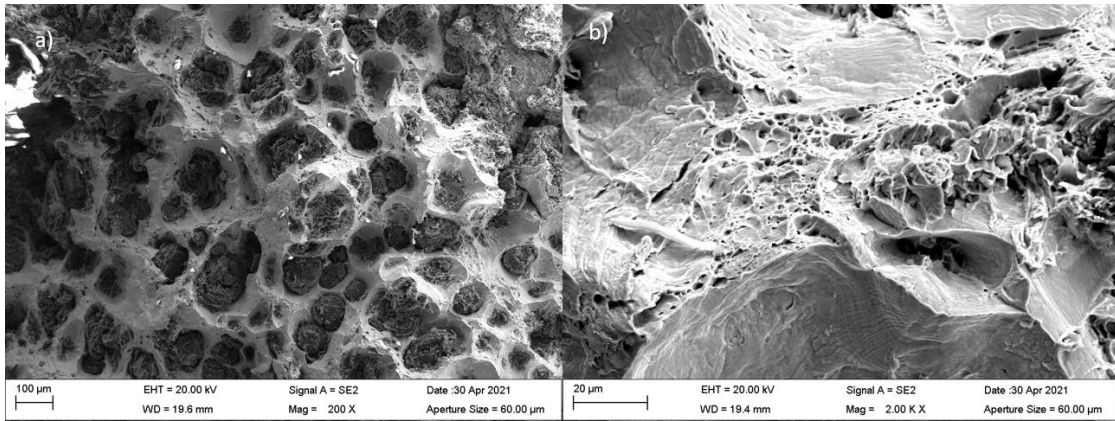

Figure 75 Fracture surface of specimen 22. a) General view of the fracture surface. b) Closeup of at the same position showing dimple pattern in the ferritic ligaments.
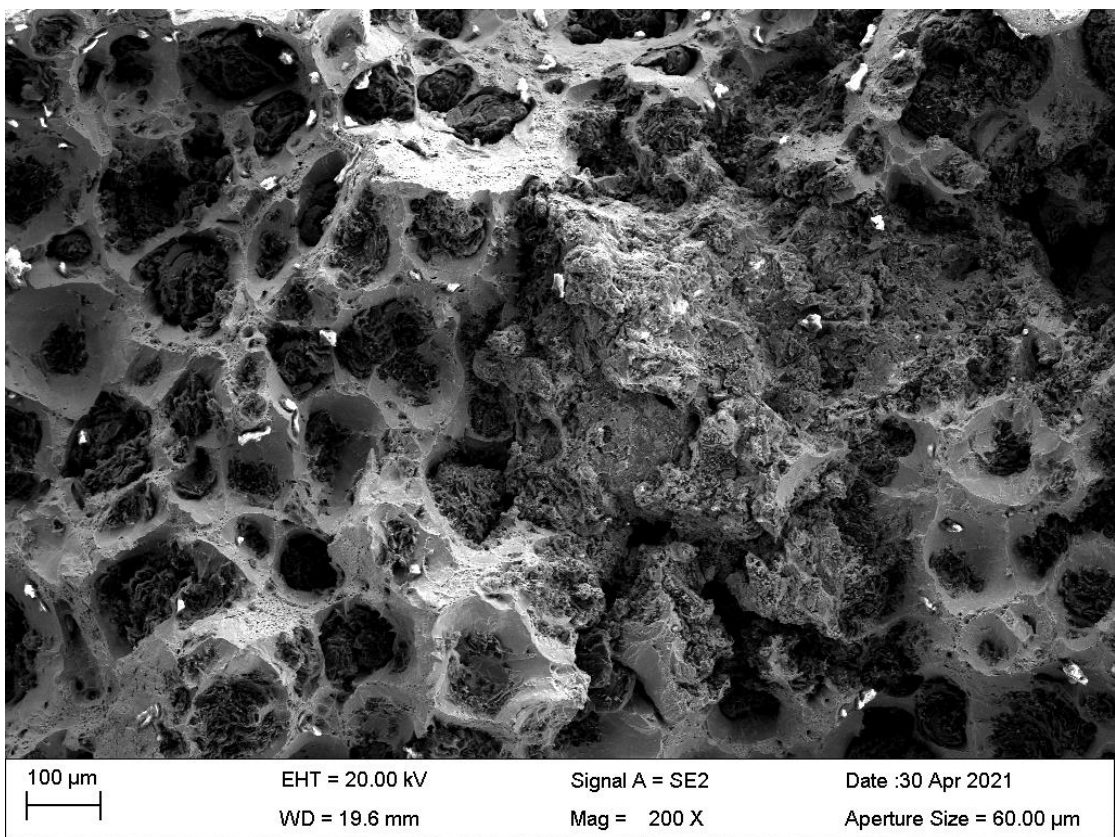

Figure 76 Fracture surface of specimen 22 at defect site. a) General view of defect site. b) Closeup of the defect showing very smooth surface indicating a presence of cavity or pore in this location.

Figure 77 shows part of fracture surface of the specimen 29. The fracture surface shows similar features to the other samples and the fracture mechanism is clearly ductile. There are small white spots present in the figure which indicate presence of some impurities in the cast. Figure 78 shows different part of the fracture surface of the specimen 29. There is clearly some casting defects and impurities present at this location. These may partly explain the fast localization of strain in this specimen.

Figure 77 Fracture surface of specimen 29. a) General view of the fracture surface showing large cavities around the graphite nodules. b) Closeup of ferritic ligament showing clear dimple pattern.

Figure 78 Fracture surface of specimen showing typical ductile fracture in the left side of the picture and some slag and impurities in the right side of the picture.

EDS analyses were made to some of the defect/impurity sites in the fracture surface of specimen 29. Figure 79, Figure 80 and Figure 81 show the EDS analysis from different sites that indicate the presence of impurities. Figure 79 indicates the presence of calcium, silicon, molybdenum, and oxygen in the cast. Figure 80 shows that there is potassium, oxygen, sodium, and aluminum in the cast as well as some chloride and titanium. Figure 81 indicates the presence of oxygen, titanium, aluminum, and silicon in the cast.
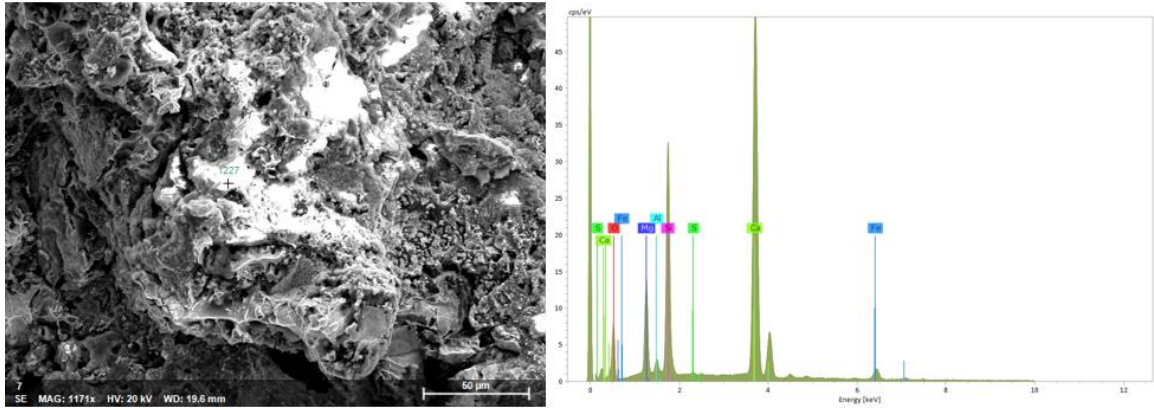
Figure 79 Specimen 29 EDS analysis indicating presence of Si, Ca, Mo and O in the cast.
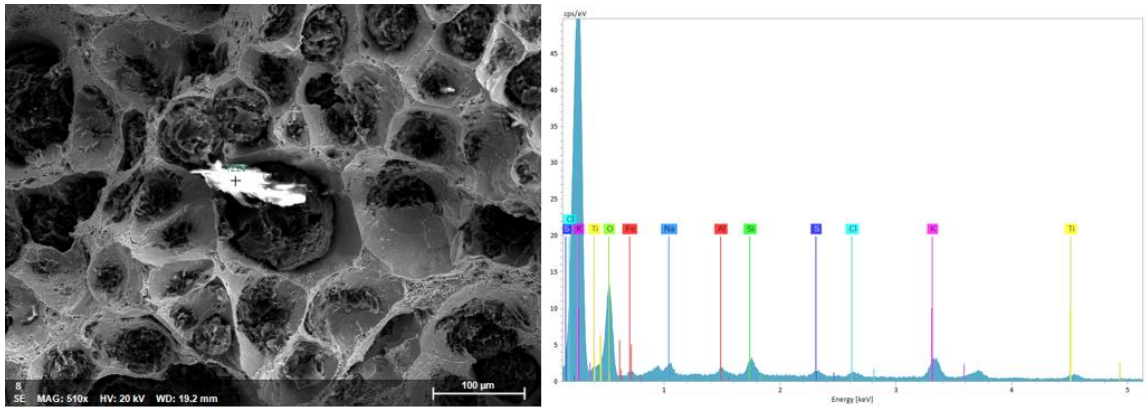

Figure 80 Specimen 29 EDS analysis indicating presence of K, O, Na, Si, and Al. The EDS analysis also gives small peaks for Ti and Cl.
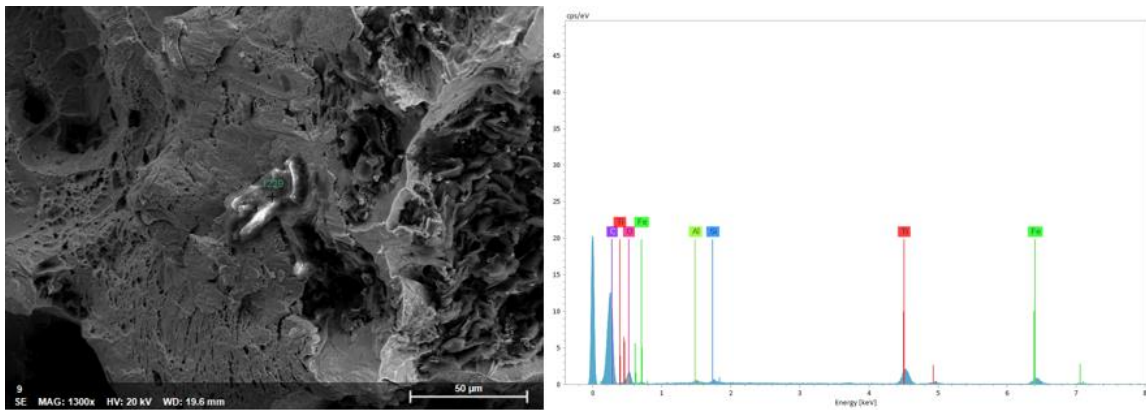

Figure 81 Specimen 29 EDS analysis indicating some O, Ti, Al and Si in the cast.

5 Discussion

This study clearly shows the inhomogeneous nature of the studied material. Due to uneven cooling of the cast and different casting defects present in the cast the specimens show quite different behavior when approaching the limits of the material. The non-homogeneous microstructure is also easily observed from the micrographs presented in this work. However, it is interesting to note that even with the presence of casting defects and scatter in the microstructure the yielding behavior is very predictable up to a certain point. Even after the strain aging the yield behavior is very predictable until the material suddenly fractures. This confirms that the graphite nodule size and distribution does not have an impact on the process of static strain aging and the static strain aging process is clearly a process that occurs in the ferritic matrix due to the interstitial solutes diffusing into the newly formed dislocations.

The aging process seems to be similar in the temperature range between 100 °C and 200 °C. The fact that there is no clearly observable difference in the yielding behavior between specimens aged at 100 °C and specimens aged at 200 °C regardless of the aging time, while there is a small observable difference in samples aged at 200 °C and 300 °C which becomes more pronounced at the temperature of 400 °C, suggests that the aging process changes at the higher temperatures of 300 °C and 400°C. Due to this the data from the higher temperature tests is likely not applicable to the conditions the insert is subjected to in the repository. It should also be noted that the results shows that the increase in yield strength is lower in the specimens that are aged in 200 °C for 11 days than in the specimens aged in 200 °C only for 1 day indicating possible over-aging. However, the difference is very small and due to the small sample size, it is statistically insignificant and could be attributed to measurement error and scatter in the material properties. Whether similar aging to the higher temperature specimens aged at 300 °C and 400 °C could occur in lower temperatures of 200 °C, 100 °C or even lower for aging times longer than 11 days is not clear and should be studied further.

The yield stress increase produced by the aging gets larger as the pre-strain is increased for all the specimens except for the specimens that are aged in 400°C for 1 day. This is somewhat contradictory with some of the reports found in literature regarding steels where the stress produced by aging is usually negatively correlated with increasing pre-strain. (See chapter: 2.3.3 The role of strain in strain aging).

All the strain aged samples show remarkable increase in the yield ratio (YS/UTS). In general, a good engineering practice is not to use material with yield ratio over 0.8. The yield ratio in the reference tensile test is around 0.71, but strain aging with all the pre-strains and aging temperatures raises the yield ratio over 0.8. For pre-strain level of 2% the yield ratio raises over 0.9 in all the cases except one and for pre-strain level of 3% the yield ratio gets even higher and close to 1.

The static strain aging lowers the total elongation of the material even when the amount pre-strain is considered in the total elongation. This is probably due the fact that the strains localize differently in the strain aged specimens than in the as received specimen. The DIC results show that there seems to be multiple distinct Lüders bands propagating in the strain

aged specimens. The bands collide with each other and prevent their movement and further propagation. The strains localize in these locked Lüders bands and cause multiple regions of localized strains along the gauge length preventing fully uniform distribution of the strain during the strain hardening. This reduced the effective gauge length of uniform elongation reducing the total elongation of the specimens.

From DIC results it is obvious that the strain aging changes the way strains localize and propagate in the specimens during the tensile tests. The as received material shows almost immediate start of uniform elongation through the whole gauge length when the specimen starts yielding. The complex arrays of non-defined and diffuse Lüders bands appear throughout the whole gauge length randomly and at very fast rate. The strain aged specimens show Lüders effect to some extent as expected from the sharp yield point. However, the Lüders effect demonstrated is not very typical and more a complex morphology of Lüders bands is observed. In all the strain aged specimens the strain first localizes at some specific point/points across the gauge length while the rest of the gauge length remain un yielded. The specimen 28 which was pre-strained by 2% shows the most typical Lüders deformation of all the specimens as the Lüders band nucleate at one end of the gauge length at the specimen shoulder and propagates towards the other end of the specimen. However, the Lüders band of the specimen 28 has somewhat diffuse front and does not have distinct border between yielded and un yielded material. The band seems to stop at around third of the gauge length and the upper half of the specimen proceeds to yield similarly to the as received material with randomly nucleating complex arrays of Lüders band. The strains in the specimen 29 which was pre-strained for 3% show immediate localization of strain in the regions where the deformation was highest during the pre-straining. This could indicate that the dislocations that are formed during the pre-straining and locked during the aging are unpinned at the yield point or that there is defect at the location of the strain localization. This kind of clear localization cannot be seen in the specimens that are pre-strained for 1% and 2%. This could be because there is higher density of dislocations in the 3% pre-strained specimen and thus there are fewer solute atoms per dislocation to form the Cottrell atmospheres. The overall locking effect is stronger in the 3% pre-strained specimen but in the locations where the dislocation density is highest the strength of the locking effect might be reduced due to limited solute atoms in the region.

Although the morphology of the Lüders bands is more complex in the strain aged specimens compared to for example the Lüders deformation of many steels, it is evident from the results that the strain aging markedly affects how the strains localize around the yield point compared to the as received material. The Lüders bands propagate faster in the specimens that are pre-strained less i.e., the strain distribution evens out faster from the start of the yielding in the specimens that have been strained less, or not at all, which is expected from the tensile experiments as the lower pre-strain specimens show little to no yield plateau after the pronounced yield point. The specimens that have been pre-strained for 3% show yield plateau to higher extent and the strain hardening region does not start immediately after the yield point.

It should be noted that the sample size for the DIC measurements is rather small and in order to get more specific and reliable data on how the strain localization and Lüders band movement differ between different pre-strain levels more experiments should be conducted.

This is especially true for the studied material as there is casting defects and natural scatter in the microstructure, which will probably have significant impact on the strain fields. There also remains the question regarding the repeatability of the DIC measurements as the speckle pattern is always slightly different when applied with spray paint. This makes repeated tests more important. It seems like the spray paint gives quite reliable results, but it would always be better to develop entirely repeatable patterning method to get more reliable data.

Despite the observed hardening and embrittlement of the material due to static strain aging the fracture mechanism does not change. All the fracture surfaces that were examined in this thesis showed signs of typical ductile fracture despite the strain aging. Even the specimen that fractured before yielding showed signs of ductile fracture.

The pre-strain levels used for this study are in line with the possible strains that the canister insert might be imposed to in the repository conditions due to rock shear movement. Although the higher pre-strains of 2% and 3% are very pessimistic and not likely to occur in practice. It is also demonstrated that static strain aging does not occur without external yielding in the cast iron insert at 100 °C and 200°C temperatures. This means that the canister would need to be subjected to two rock shear movement that cause yielding for static strain aging to have impact on the mechanical properties during the rock shear movement. This is very unlikely. Additionally, all the strain aged specimens except for one (specimen 5) fulfill the minimum ductility requirement of 3% plastic strain. This means that even if two rock shear movements would occur for the same canister, the canister is likely to survive them without failing, despite the static strain aging occurring after the first rock shear movement. However, as demonstrated in this work, although unlikely, it is possible that the material breaks before yielding after SSA has occurred. This is probably due to the contribution of casting defects and impurities in the cast together with the static strain aging effect. However, global failure in the insert would be very unlikely because of casting defects and strain aging.

In this study it was demonstrated that even small plastic deformation of around 1% causes marked strain aging effect on the material even with moderate temperatures and moderate aging times. Static strain aging occurs readily already at room temperature for the studied material. These findings are important as they confirm that SSA is likely to occur to some degree in the repository conditions and the effects of strain aging on the cast iron insert should be considered further. It is especially important to consider the possible synergistic effects of other possible embrittlement mechanism such as hydrogen embrittlement that could work synergistically with strain aging and cause the insert to become very brittle. The effect of static strain aging and hydrogen embrittlement seem to be very different, and they seem to affect the material through very different mechanisms. Unlike static strain aging, introducing hydrogen to the material will not cause yield point phenomenon to occur. Additionally, it has been demonstrated that the insert material will break by brittle cleavage fracture when loaded with hydrogen (see section: "2.4.1 Hydrogen embrittlement") unlike the SSA specimens. However, these phenomena manifest somewhat similarly reducing the total elongation of the material and the synergistic effect of strain aging and hydrogen embrittlement could be dramatic due to the different mechanism affecting the material and thus should be studied.

In this study the effect of different strain rate during the strain aging was not considered. As a result, there remains some question regarding the dynamic strain aging of the cast iron insert. In the repository conditions the canister can be subjected to wide variety of different strain rates due to the long time span and different types of rock movements. This could result in dynamic strain aging occurring already at low and moderate temperatures. There have been some studies regarding the dynamic strain aging of cast iron, but the strain rate dependency has not been studied yet in this material and whether the DSA occurs already at lower temperatures below 125 °C when the stain rate is low enough has not been demonstrated.

6 Conclusion

In this paper the static strain aging in DCI was studied. The main findings are compiled below:

- The SSA specimens pre-strained for 1%, 2% and 3% all showed pronounced yield point although the as received material yielded smoothly with no pronounced yield point. There is no yield plateau observed in the SSA specimens pre-strained for 1% or 2% but some yield plateau can be observed in the specimens pre-strained for 3% to some extent.

- The stress produced by aging increased as the pre-strain was increased for all the specimens except for the specimens that were aged in 400 °C for 1 day. In the aforementioned group the stress produced by aging decreased slightly when pre-strain was increased.

-The strain aging behavior was predictable between all the specimens. The yield strength and the tensile strength increased when the pre-strain was increased. There was no observable difference in the yield stress and tensile stress of the specimens when they were aged in 100 and 200 °C for 1 day and 11 days. The formation of Cottrell atmospheres seems to saturate already at 100 °C when aged for 1 day and the longer aging of 11 did not have different effect.

-The yield point is clearly less pronounced, and the yield strength increases less when the specimens are aged in temperatures between 300 and 400 °C. This indicates that the aging process changes, and the Cottrell atmospheres probably partly "evaporate" back to the solvent matrix reducing the dislocation locking effect.

- The fracture mechanism stays ductile in all the specimens despite the level of strain aging.

-From the DIC results the SSA specimens show more localized yielding behavior around the yield point compared to the as received material. The as received material starts to yield uniformly with no clear deformation bands while the SSA specimens show nucleation of Lüders bands at the yield point.

-The higher pre-strain levels cause the localization of the strains to higher degree. For the pre-strain level of 3% the strain seems to immediately localize to the points that showed most deformation during the pre-straining process, indicating unlocking of the dislocations.

7 References

[1] K. Ikonen, "Fuel Temperature in Disposal Canisters Fuel Temperature in Disposal Canisters," *Posiva Working Report 2006-19*, Posiva OY, Olkiluoto, Finland, p. 47, 2006.

[2] S. F. Chen, T. S. Lui, and L. . Chen, "Dynamid Strain Ageing of Ferritic Spheroidal Graphite Cast Iron in the Temperature Range 300K-700K." 1993 Available: DOI:https://doi.org/10.11279/imono.65.7_535.

[3] H. Mouri, M. Hayashi, and W. Wunderlich, "Effect of dynamic strain aging on isothermal (473) low cycle fatigue of ferritic ductile cast iron."*Mater. Trans.*vol. 50. no. 8.pp. 1935–1940. 2009. ISSN:13459678. Available: DOI:10.2320/matertrans.MRA2008482.

[4] Posiva and SKB, "Safety functions, performance targets and technical design requirements for a KBS-3V repository Conclusions and recommendations from a joint SKB and Posiva working group.," *Posiva SKB Report 01*, Eurajoki, Finland, p. 120, 2017.

[5] P. Eriksson, "Strategy , adaptive design and quality control of bentonite materials for a KBS-3 repository," *SKB Technical Report TR-20-03*, 2020.

[6] H. Raiko, "Canister Design 2012," *Posiva Report 2012-13*, Posiva OY, Eurajoki, Finland, p. 156, 2012 ISBN:978-951-652-194-0.

[7] T. Siren, "Excavation damage zones , fracture mechanics simulation and in situ strength of migmatitic gneiss and pegmatitic granite at the nuclear waste disposal site in Olkiluoto , Western Finland," 2015 ISBN:978-952-60-65-17-5.

[8] SKB - Svensk Kärnbränslehantering AB, "Design premises for a KBS-3V repository based on results from the safety assessment SR-Can and some subsequent analyses," *SKB Technical Report TR-09-22*, p. 44, 2009.

[9] SKB - Svensk Kärnbränslehantering AB, "Long-term Safety for the Final Repository for Spent Nuclear Fuel at Forsmark," *SKB Technical Report TR-11-01*, vol. 2, Stockholm, Sweden, 2011.

[10] M. Jonsson and L. Emilsson, "Mechanical design analysis for the canister," *Posiva SKB Report 04*, Eurajoki, Finland, p. 147, 2018.

[11] J. Pitkänen, "Inspection of Disposal Canisters Components," *Posiva Report 2012-35*, Eurajoki, Finland, 2013 ISBN:978-951-652-216-9.

[12] H. Raiko, T. Jalonen, L. Nolvi, B. Pastina, J. Pitkänen, and T. Salonen, "Canister Production Line 2012: Design, Production and initial state of the canister," *Posiva Report 2012-16*, Eurajoki, Finland, p. 174, 2012 ISBN:978-951-652-197-1.

[13] Swedish Nuclear Fuel and Waste Management Company (SKB), "Design, production and initial state of the canister," *SKB Technical Report TR-10-14*, Stockholm, Sweden, p. 111, 2010.

[14] C. F. O. Dahlberg, M. Öberg, and J. Faleskog, "Continuum modeling of nodular cast iron using a porous plastic model with pressure-sensitive matrix — Experiments ,

model calibration & verification Continuum modeling of nodular cast iron using a porous plastic model with pressure-sensitive matrix — Expe." 2015 Available: DOI:10.13140/RG.2.1.2426.1840.

[15] U. Ronneteg and T. Grybäck, "Non-destructive testing of canister components and welds Summary," *SKBdoc 1434744*, p. 127, 2014 ISBN:5561752014.

[16] D. A. Bowman and E. J. Kingston, "DHD residual stress measurements within the cast iron insert of a radioactive waste canister," *Client : POSIVA Report No .: R11-001 – Version 3*, 2013.

[17] A. Shipsha, "Evaluation of residual stress measurements. Effect of measured residual stresses on damage tolerance of cast iron PWR- and BWR-inserts," *Inspecta Technical Report No. 50018390-1*, no. 2, Inspecta Technology AB, Stockholm, Sweden, 2015.

[18] H. Raiko, H. Rydén, and M. Johansson, "Design analysis report for the canister," *SKB Technical Report TR-10-28*, p. 80, 2010.

[19] B. Miller and N. Marcos, "Process Report – FEPs and Scenarios for a Spent Fuel Repository at Olkiluoto," *Posiva Report 2007-12*, Posiva OY, Eurajoki, Finland, p. 274, 2007 ISBN:978-951-652-162-9.

[20] L. Börgesson, C. Technology, A. B. L. Johannesson, A. B. Heikki, and R. Vtt, "Uneven swelling pressure on the canister simplified load cases derived from uneven wetting, rock contours and buffer density distribution 1206894," *SKBdoc 1206894*, p. 27, 2009.

[21] L. Börgesson, C. T. Ab, J. Hernelind, and E. Ab, "Earthquake induced rock shear through a deposition hole the damage caused to the canister," *SKB Technical Report TR-06-43*, Stockholm, Sweden, p. 42, 2006.

[22] P. Dillström and L. Alverlind, "Probabilistic analysis of BWR canister inserts for spent nuclear fuel in the case of," *Inspecta Technical Report No.50014130-1*, no. 5, Stockholm, Sweden.

[23] P. Minnebo, K. F. Nilsson, and D. Blagoeva, "Tensile, compression and fracture properties of thick-walled ductile cast oron components."*J. Mater. Eng. Perform.*vol. 16. no. 1.pp. 35–45. 2007. ISSN:10599495. Available: DOI:10.1007/s11665-006-9005-z.

[24] K.-F. Nilsson, F. Lofaj, M. Burström, C.-G. Andersson, and SKB, "Pressure tests of two KBS-3 canister mock-ups," *SKB Technical Report TR-05-18*, 2005.

[25] K. F. Nilsson, M. Burström, F. Lofaj, and C. G. Andersson, "Failure of spent nuclear fuel canister mock-ups at isostatic pressure."*Eng. Fail. Anal.*vol. 14. no. 1.pp. 47–62. 2007. ISSN:13506307. Available: DOI:10.1016/j.engfailanal.2006.01.005.

[26] K. Ikonen, "Mechanical Analysis of Cylindrical Part of Canisters for Spent Nuclear Fuel Mechanical Analysis of Cylindrical Part of Canisters for Spent Nuclear Fuel," *Posiva Working Report 2005-12*, Posiva OY, Olkiluoto, Finland, 2005.

[27] O. Martin, K. F. Nilsson, and N. Jakšić, "Numerical simulation of plastic collapse of copper-cast iron canister for spent nuclear fuel."*Eng. Fail. Anal.*vol. 16. no. 1.pp.

225–241. 2009. ISSN:13506307. Available: DOI:10.1016/j.engfailanal.2008.03.005.

[28] J. Hernelind, E. Ab, L. Å. Qa, and J. Sarnet, "Hydrostatic pressure for detailed BWR / PWR-canisters Abstract Sammanfattning," *SKBdoc 1454226*, Stockholm, Sweden, 2015.

[29] L. Börgesson and J. Hernelind, "Earthquake induced rock shear through a deposition hole - Part 2," pp. 1–65, 2013.

[30] J. Hernelind, "Modelling and analysis of canister and buffer for earthqake induced rock shear and glacial load," *SKB Technical Report TR-10-34*, Stockholm, Sweden, p. 124, 2010.

[31] J. Hernelind and E. Ab, "Detailed models for PWR- and BWR-canisters for Earthquake induced rock shearing Abstract," *SKB Public Report SKBdoc 1415152*, no. 2, Stockholm, Sweden, p. 193, 2014.

[32] P. Dillström, "Damage tolerance analysis of BWR-canister inserts for spent nuclear fuel in the case of an earthquake induced rock shear load – Influence of using more detailed models," *Inspecta Technical Report No.5000264-1*, Stockholm, Sweden, p. 44, 2015.

[33] K. Ikonen and H. Raiko, "Thermal dimensioning of spent fuel repository," *Posiva Working Report 2009-69*, Eurajoki, Finland, p. 76, 2012.

[34] R. E. Smallman and A. H. W. Ngan, *Modern Physical Metallurgy*. Oxford: Elsevier Science & Technology, 2013.

[35] D. Hull and D. J. Bacon, *Introduction to Dislocations*, 5th ed. Elsevier Science & Technology, 2011 ISBN:9780080966731.

[36] R. E. Smallman and A. H. W. Ngan, "7 Diffusion," in *Modern Physical Metallurgy*, Elsevier Science & Technology, 2013 ISBN:9780080982236.

[37] D. J. B. Hull, Derek, "10 . 5 SOLUTE ATMOSPHERES AND YIELD PHENOMENA," in *Introduction to Dislocations*, 5th ed., 2011, pp. 220–227 ISBN:9780080966731.

[38] A. H. Cottrell and B. A. Bilby, "Dislocation theory of yielding and strain ageing of iron."*Proc. Phys. Soc. Sect. A*.vol. 62. no. 1.pp. 49–62. 1949. ISSN:03701298. Available: DOI:10.1088/0370-1298/62/1/308.

[39] H. Bhadeshia and R. Honeycombe, *Steels: Microstructure and Properties*, 4th ed. Elsevier Science & Technology, 2017 ISBN:9780081002728.

[40] I. Codd and N. J. Petch, "Dislocation-locking by carbon, nitrogen and boron in α-iron."*Philos. Mag. A J. Theor. Exp. Appl. Phys*.vol. 5. no. 49.pp. 30–42. 1960. ISSN:00318086. Available: DOI:https://doi.org/10.1080/14786436008241198.

[41] D. Caillard, "Dynamic strain ageing in iron alloys: The shielding effect of carbon."*Acta Mater*.vol. 112.pp. 273–284. 2016 Available: DOI:https://doi.org/10.1016/j.actamat.2016.04.018.

[42] H. Mouri, W. Wunderlich, and M. Hayashi, "New aspects about reduced LCF-life time of spherical ductile cast iron due to dynamic strain aging at intermediate temperatures."*J. Nucl. Mater*.vol. 389. no. 1.pp. 137–141. 2009 Available:

DOI:https://doi.org/10.1016/j.jnucmat.2009.01.018.

[43]   A. Ramazani, S. Bruehl, T. Gerber, W. Bleck, and U. Prahl, "Quantification of bake hardening effect in DP600 and TRIP700 steels."*Mater. Des.*vol. 57.pp. 479–486. 2014. ISSN:18734197. Available: DOI:10.1016/j.matdes.2014.01.001.

[44]   T. Waterschoot, A. K. De, S. Vandeputte, and B. C. de Cooman, "Static strain aging phenomena in cold-rolled dual-phase steels."*Metall. Mater. Trans. A Phys. Metall. Mater. Sci.*vol. 34. no. 13.pp. 781–791. 2003. ISSN:10735623. Available: DOI:10.1007/s11661-003-1006-z.

[45]   W. Zhao, M. Chen, S. Chen, and J. Qu, "Static strain aging behavior of an X100 pipeline steel."*Mater. Sci. Eng. A.*vol. 550.pp. 418–422. 2012. ISSN:09215093. Available: DOI:10.1016/j.msea.2012.04.095.

[46]   S. Gündüz, "Static strain ageing behaviour of dual phase steels."*Mater. Sci. Eng. A.*vol. 486. no. 1–2.pp. 63–71. 2008. ISSN:09215093. Available: DOI:10.1016/j.msea.2007.08.056.

[47]   T. S. Lui and C. G. Chao, "High-temperature properties of ferritic spheroidal graphite cast iron."*J. Mater. Sci.*vol. 24. no. 7.pp. 2503–2507. 1989. ISSN:00222461. Available: DOI:10.1007/BF01174520.

[48]   A. K. De, S. Vandeputte, and B. C. De Cooman, "Static strain aging behavior of ultra low carbon bake hardening steel."*Scr. Mater.*vol. 41. no. 8.pp. 831–837. 1999 Available: DOI:10.1016/S1359-6462(99)00232-8.

[49]   L. J. Baker, S. R. Daniel, and J. D. Parker, "Metallurgy and processing of ultralow carbon bake hardening steels."*Mater. Sci. Technol.*vol. 18. no. 4.pp. 355–368. 2002. ISSN:02670836. Available: DOI:10.1179/026708302225002452.

[50]   A. A. Vasilyev, H. C. Lee, and N. L. Kuzmin, "Nature of strain aging stages in bake hardening steel for automotive application."*Mater. Sci. Eng. A.*vol. 485. no. 1–2.pp. 282–289. 2008. ISSN:09215093. Available: DOI:10.1016/j.msea.2007.07.075.

[51]   P. Seraj and S. Serajzadeh, "Static Strain Aging Behavior of a Manganese-Silicon Steel After Single and Multi-stage Straining."*J. Mater. Eng. Perform.*vol. 25. no. 3.pp. 1047–1055. 2016. ISSN:15441024. Available: DOI:10.1007/s11665-016-1906-x.

[52]   M. Koyama, E. Akiyama, and K. Tsuzaki, "Factors affecting static strain aging under stress at room temperature in a Fe-Mn-C twinning-induced plasticity steel."*Tetsu-To-Hagane/Journal Iron Steel Inst. Japan.*vol. 100. no. 9.pp. 1123–1131. 2014. ISSN:00211575. Available: DOI:10.2355/tetsutohagane.100.1123.

[53]   B. R. S. Silva, F. Salvio, and D. S. Santos, "Hydrogen Embrittlement in Super Duplex Stainless Steel Tubes UNS S32750 Under Mechanical Stress."*Int. Hydrog. Conf. (IHC 2012).*no. January.pp. 245–254. 2014 Available: DOI:10.1115/1.860298_ch26.

[54]   H. Matsunaga, T. Usuda, K. Yanase, and M. Endo, "Ductility loss in ductile cast iron with internal hydrogen."*Metall. Mater. Trans. A Phys. Metall. Mater. Sci.*vol. 45. no. 3.pp. 1315–1326. 2014. ISSN:10735623. Available: DOI:10.1007/s11661-013-2109-9 ISBN:1166101321099.

[55] A. Forsström, Y. Yagodzinskyy, and H. Hänninen, "Hydrogen effects on mechanical performance of nodular cast iron."*Corros. Rev.* 2019. ISSN:03346005. Available: DOI:10.1515/corrrev-2019-0007.

[56] P. Sahiluoma, Y. Yagodzinskyy, A. Forsström, H. Hänninen, and S. Bossuyt, "Hydrogen embrittlement of nodular cast iron."*Mater. Corros.*vol. 72. no. 1–2.pp. 245–254. 2021. ISSN:15214176. Available: DOI:10.1002/maco.202011682.

[57] R. W. Hertzberg, R. P. Vinci, and J. L. Hertzberg, *Deformation and fracture mechanics of engineering materials*. Hoboken, NJ : Wiley, 2013.

[58] P. Olsson *et al.*, "Electron irradiation accelerated Cu-precipitation experiment – Testing of canister insert cast iron and an FeCu model alloy," *SKB Technical Report R-13-50*, p. 18, 2013.

[59] L. Brissonneau, A. Barbu, and J. L. Bocquet, "Radiation effects on the mechanical properties and long term ageing of spent fuel storage containers," in *The 14th international symposium on the packaging and transportation of radioactive materials. Conference proceedings*, 2004.

[60] Z. Chang, "Multiscale modelling of radiation-enhanced diffusion phenomena in metals," 2015 ISBN:9789175954950.

[61] Q. Yang, E. Toijer, and P. Olsson, "Analysis of radiation damage in the KBS-3 canister materials," *SKB Techical Report*, p. 27, 2019.

[62] R. Bigger *et al.*, "A Good Practices Guide for Digital Image Correlation," *International Digital Image Correlation Society*, p. 94, 2018 Available: DOI:10.32720/idics/gpg.ed1.

8 Appendices

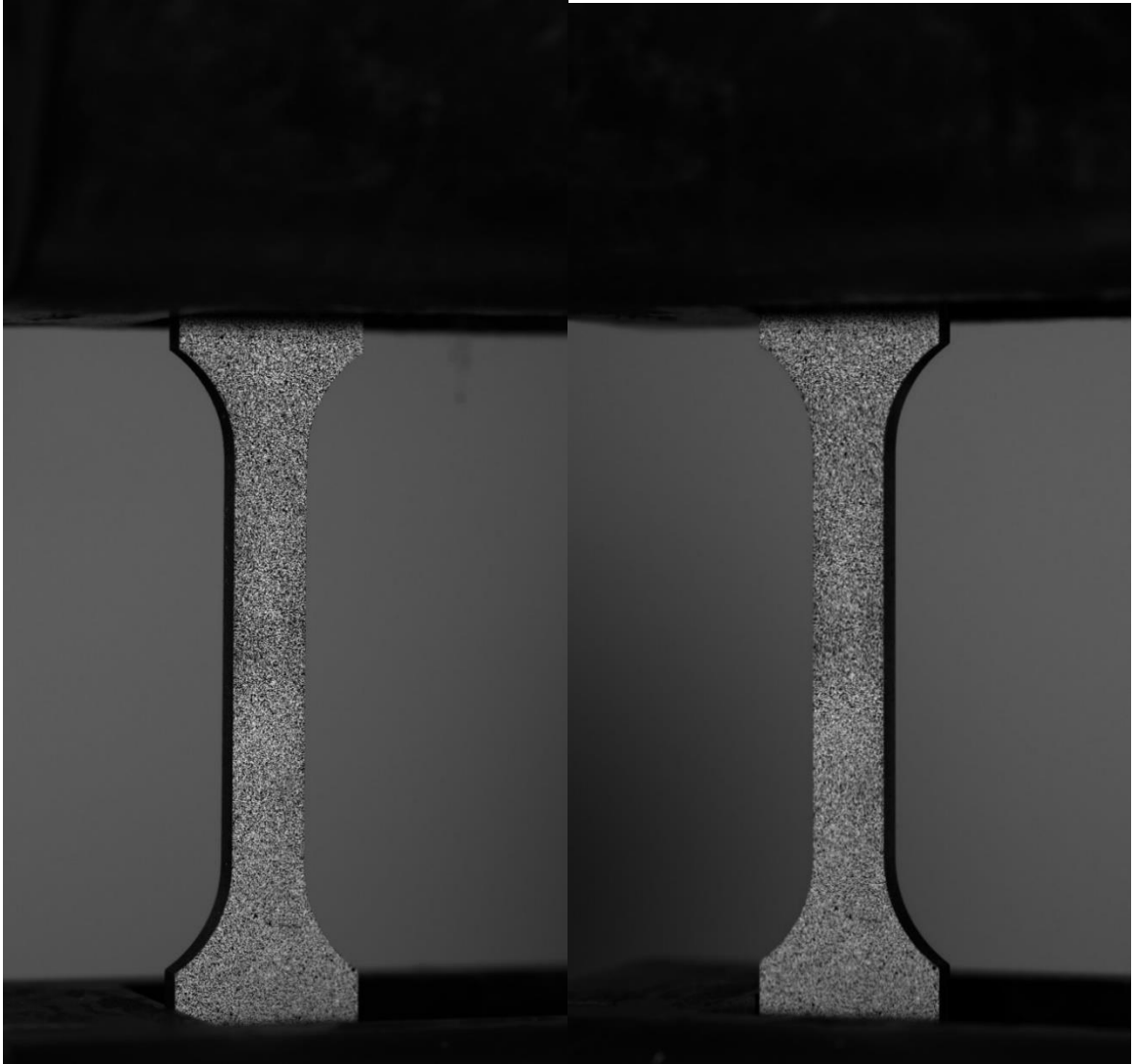## 8.1 Appendix 1. Speckle patterns used for the DIC experiments

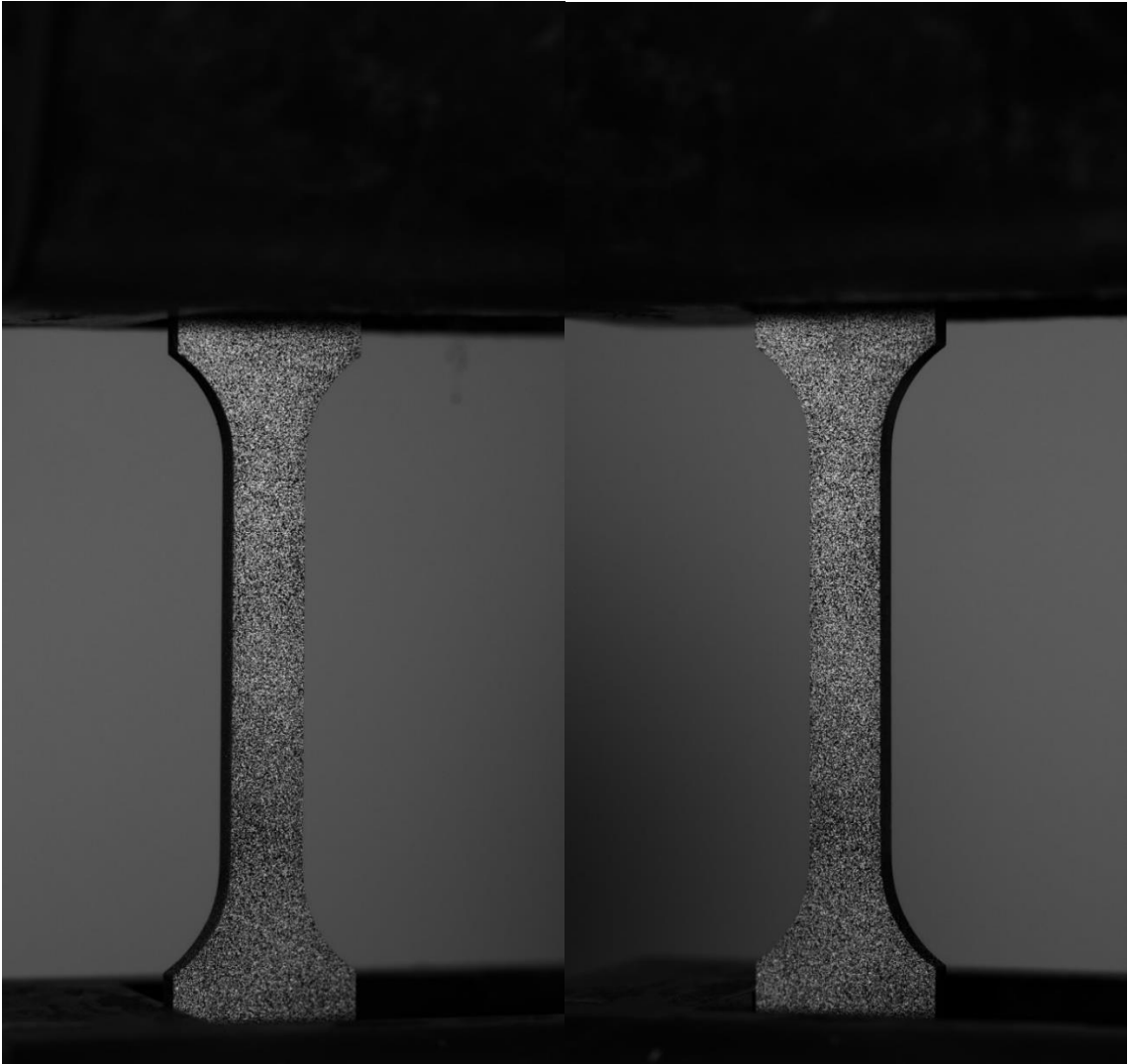**Figure 82 Specimen 24 speckle pattern for pre-straining**
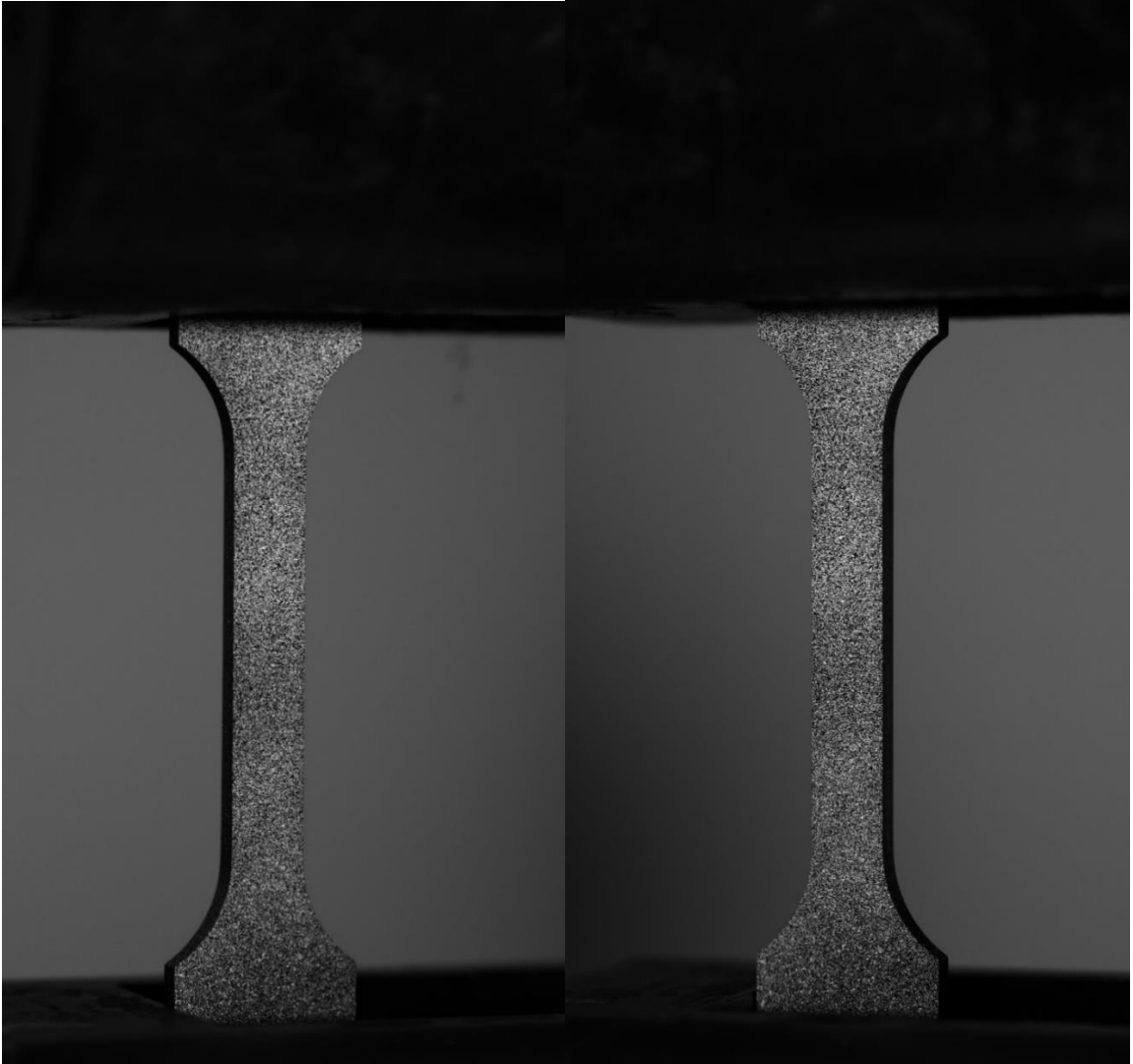
Figure 83 Specimen 28 speckle pattern for pre-straining

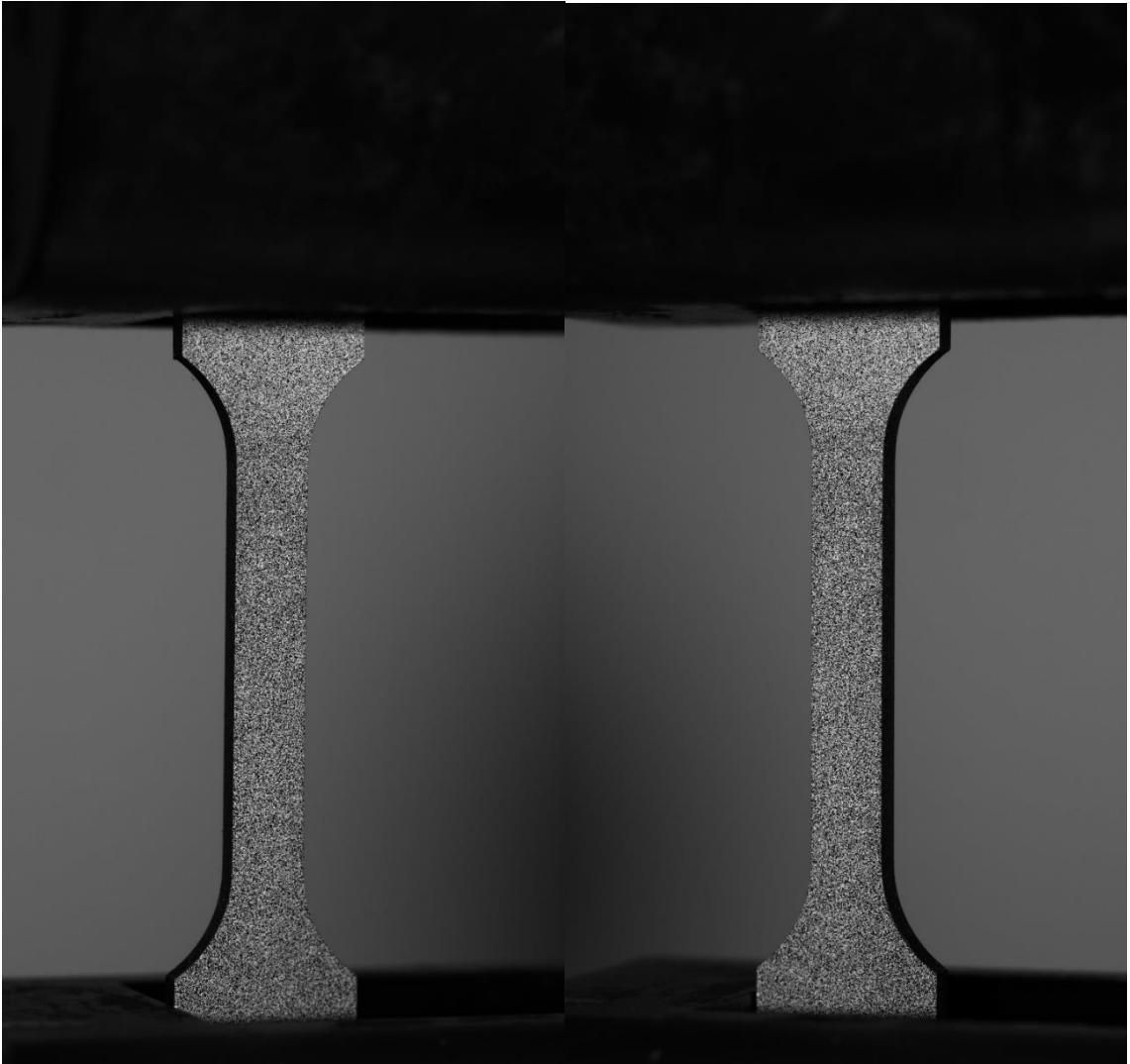**Figure 84 Specimen 29 speckle pattern for pre-straining**
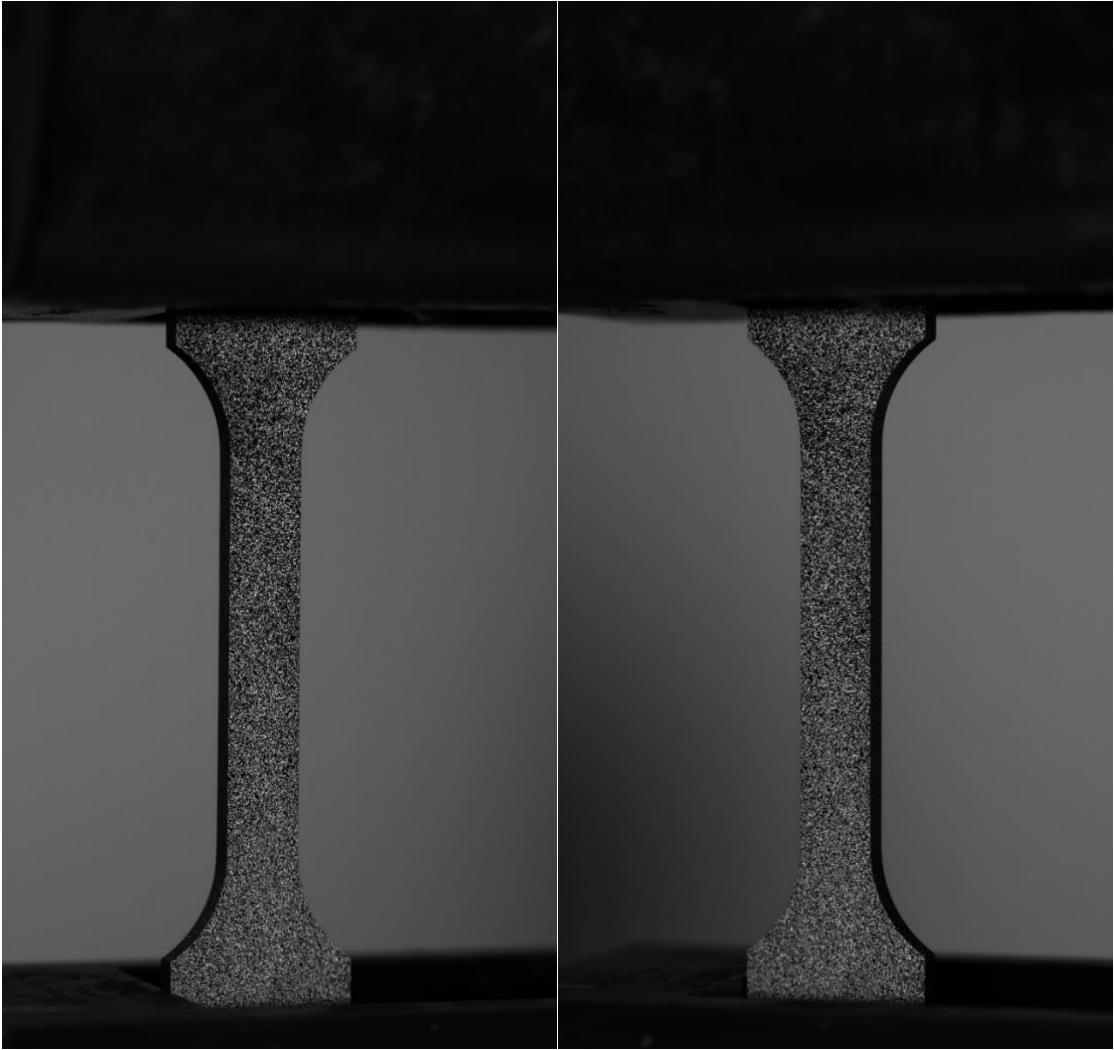
Figure 85 Specimen 26 speckle pattern for tensile test

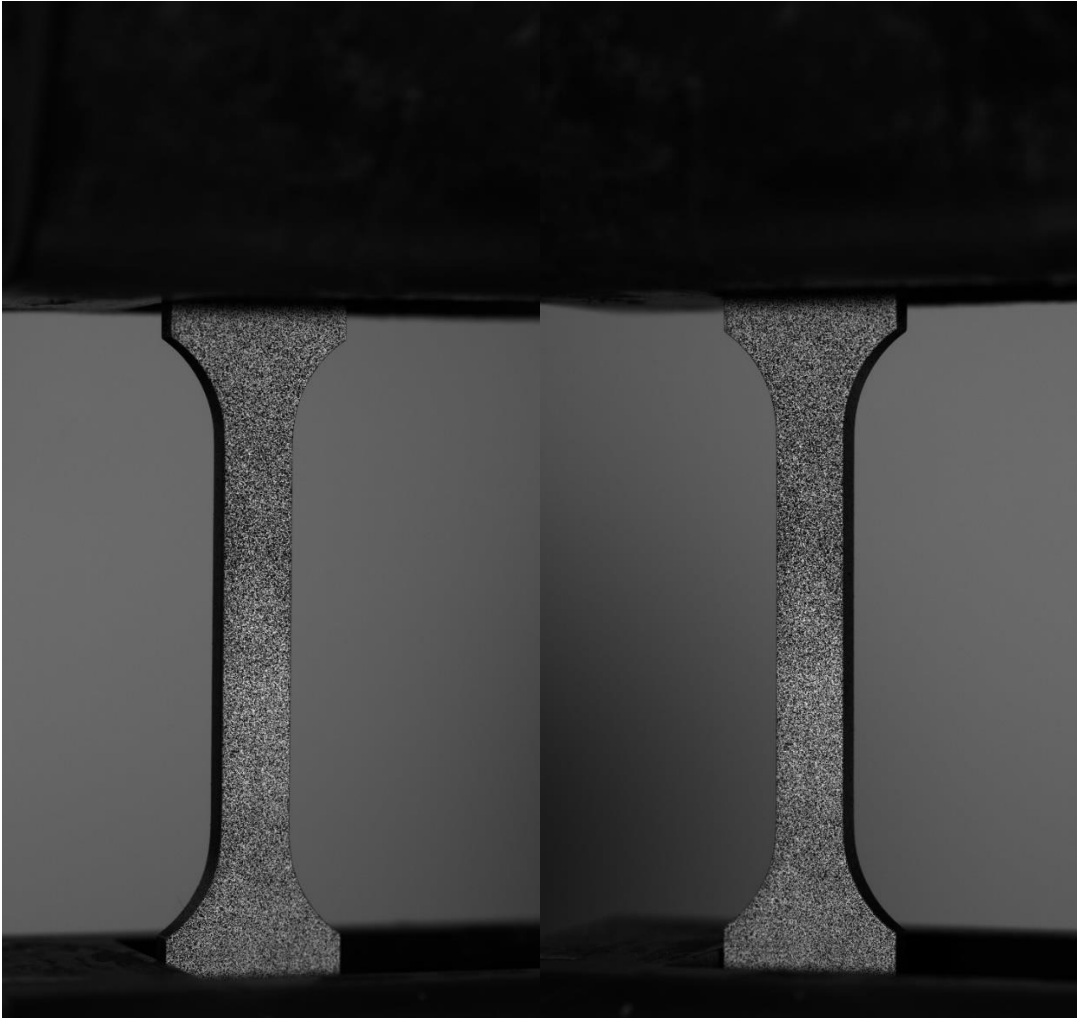**Figure 86 Specimen 24 speckle pattern for tensile test**
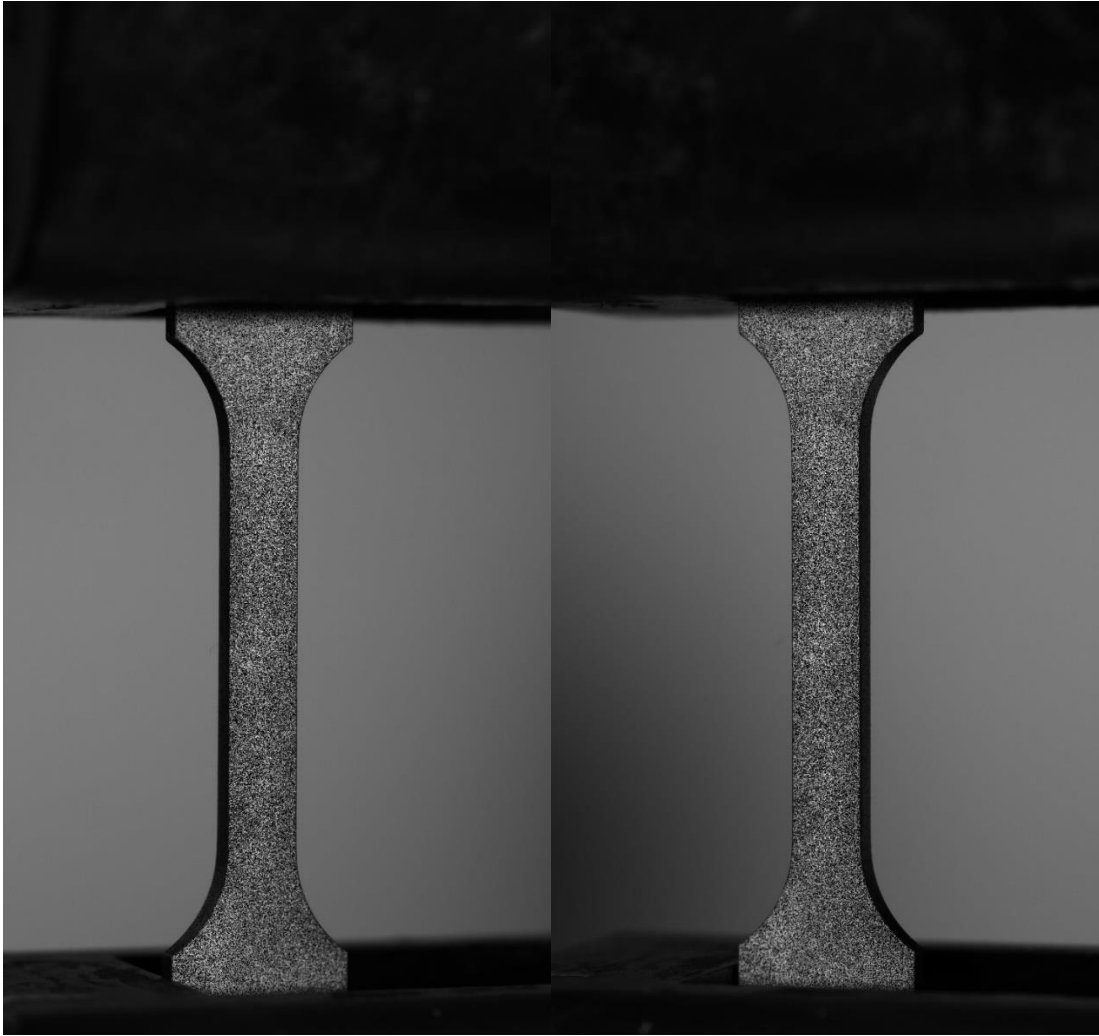
Figure 87 Specimen 28 speckle pattern for tensile test

Figure 88 Specimen 29 speckle pattern for tensile test